TRIBOLOGICAL CHARACTERIZATION OF SURFACE ENGINEERED TOOLING

TRIBOLOGICAL CHARACTERIZATION OF SURFACE ENGINEERED TOOLING FOR METAL CUTTING APPLICATIONS

By

ANDREW BIKSA, B.A.Sc.

(University of Toronto, Canada)

A Thesis

Submitted to the School of Graduate Studies

in Partial Fulfillment of the Requirements

for the Degree

Master of Applied Science

McMaster University

MASTER OF APPLIED SCIENCE (2010) McMaster University

(Mechanical Engineering) Hamilton, Ontario

TITLE: Tribological Characterization of Surface Engineered Tooling for Metal Cutting Applications

AUTHOR: Andrew Biksa, B.A.Sc. (University of Toronto, Canada)

SUPERVISOR: Dr. Stephen Veldhuis

Department of Mechanical Engineering

McMaster University

NUMBER OF PAGES: xiv, 198

Abstract

The objective of this research was to develop a bench scale apparatus (tribometer) for mimicking the friction and wear conditions on the rake face of a metal cutting tool. The motivation for this study was to save test material costs, reduce machine downtime for testing, increase the number of test replicates and effectively add a reliable testing tool to characterize metal cutting operations and coating performance. The tribometer provides useful results approximately 8 times faster than an industrial machine once all materials have been obtained.

This study focuses primarily on isolating and studying the adhesive conditions on the seizure zone of the rake face. The setup simulates subsurface plastic flow in high temperature, near seizure conditions. This unit was constructed as a modified Brinell hardness test. A spherical tipped pin (3mm diameter) made of tooling material and treated with a coating is loaded under high stress and high temperature into a flat disk made of the workpiece material. The disk then rotates. The pin is aligned such that it is on the axis of rotation of the disk to produce near zero seizure like velocity. A high resolution reaction torque sensor measures the friction stress. The test unit is capable of simulating normal stresses of 0-4GPa and temperatures from room temperature up to 700-800°C depending on the specimens and heating patterns required.

This study focused on coated and uncoated cemented carbide pins with 6% cobalt. The workpiece materials used were Ti6Al4V and Inconel 718. 2 cases were tested for each workpiece. First the uncoated pin was tested,

followed by an AlTiN Xceed® coating from Oerlikon Balzers®. Research conducted on an industrial machine has shown positive correlations with the tribometer measurements and agrees with the findings of our colleague Dr. L.S. Shuster in Russia who uses a similar test setup. The wear of the coated samples was lower than the uncoated samples.

The coefficient of friction (COF) was found to be the most suitable parameter for calculating tool performance. In general, the tests completed by the MMRI and Dr. Shuster (Fox-Rabinovich, Yamamoto and Aguirre, et al. 2010) showed that COF in similar rake face seizure conditions of a cutting tool is in the range of 0.2 – 0.35. The MMRI tribometer COF is calculated as follows:

$$\mu_{MMRI} = \frac{3M_{TOT}}{2F_N R_{IND}} = \frac{\tau}{\sigma} = \frac{F_F}{F_N}$$

Here M_{TOT} is the reaction torque measured, F_N is the normal load applied and R_{IND} is the outer radius of the disk print whether a spherical imprint or a flat circular scratch. Temperature was found to be the most important variable affecting friction and it was also the most difficult variable to accurately measure. The interface temperature and the temperature gradient within the workpiece/disk material are the most significant thermal variables.

To my parents, Paula and Victor Biksa.
Their encouragement and support
made this opportunity possible.

Acknowledgements

This research was made possible due to the significant contributions of the research and technical staff within the MMRI and McMaster University. First off I would like to thank Dr.Stephen Veldhuis for giving me the opportunity to work on this custom tribometer. His constant encouragement and technical support made this project enjoyable and successful. I would also like to specially thank Dr.German Fox-Rabinovich and Dr. Philip Koshy who offered expertise in machining and coatings on a daily basis.

I would also like to thank Mr. Terry Wagg, Mr. Doug Culley, Mr. Maneesh Khanna, Mr. Joe Verhaege, Dr. Julia Dosbaeva, Mr. Ron Loedwyks, Mr. Jim McClaren, Mr. Mark Mackenzie and Mr. J.P Talon for their constant support and technical feedback.

Amongst my graduate student colleagues I would like to thank Mr. Youssef Ziada, Mr. Josh Tovey, Mr. Mohammed Tauhiduzzaman, Ms. Zareena Ghani, Ms. Holly Dzuba, Mr. Brian Perry, Mr. Jeremy Boyd and Mr. Nima Zarif for sharing their ideas and support.

Lastly I would like to thank Dr. Eugene Ng and Dr. Tim Nye for being on my thesis committee and reviewing this work.

Table of Contents

List of Figures

List of Tables

Chapter 1. Introduction

Tribology is defined as the study of friction, lubrication and wear of materials. Friction occurs whenever materials slide in contact with each other. If relative sliding occurs between the materials, the interfacial zone between the materials will begin to wear. The focus of this research was on the tribological interaction of machine cutting tools and a workpiece during industrial machining applications. The goal of machining is to remove material from a workpiece in a precise and accurate fashion. The finished part typically must be of a high quality that matches the tolerances of a design drawing. As machining typically occurs under high stresses in the range of 1-3GPa and temperatures reaching as high as 1000°C the friction and resulting wear of the interacting tool and workpiece is often aggressive. Thus, it would be valuable for the following reasons to understand and extend the life and performance of machine tooling:

- Longer tool life reduces the number of tools which need to be purchased which is an economic benefit.
- Less friction will causes less wear to the tool which will increase part quality surface finish and result in a higher percentage of parts that meet design specification tolerances.
- Less friction could eliminate or reduce the use of lubrication which is an economic cost and environmental concern for disposal.

- Longer tool life results in less machine downtime and labour associated with setting up and replacing worn tools which increases profitability.
- Less friction could allow for a safe and acceptable metal removal rate (MRR) increase which increases profitability as more material is removed faster which increases productivity.

1.1 Research Motivation

To be able to achieve these goals in a reasonable time frame, a well designed research platform needs to be created. Ideally research should be carried out on the industrial machine in question as it is difficult to replicate the exact operating conditions. In general research on an industrial machine is limited for the following reasons:

- Time on industrial machines is expensive. It is not economically viable to purchase a machine in excess of $100,000 to do a series of testing each time a new set of conditions is being used in the field.
- Downtime is often unacceptable in the field as it reduces profits so there is limited time to do thorough testing on the actual industrial machine that would be used.
- The time to wear a tool from an initial state to a worn state can use a substantial amount of workpiece which comes at an appreciable cost both in terms of time and materials. All of this effort and labour produces one single test point. Often replicates of a test provide a better scope of performance but often this cannot be done again due to time and cost concerns.

- Industrial tests are not equipped to isolate the effects of temperature and normal stress, as they are outputs based on the machine input parameters.

As a result it is extremely useful to have a bench scale express test that can produce useful and accurate results without running into the limitations outlined above. This test would not necessarily have to be an exact representation of the machining process but if it encompassed the principle elements which reproduced a similar phenomenon it could produce a useful snapshot of the physical processes being undertaken in machining. Furthermore, if this bench scale express test was flexible it would allow the researcher to have control over many variables. For example, temperature and load are not variables that can be directly selected in machining. These variables are the result of picking feed rates, depth or cut and RPM for example. Thus this flexibility and insight could give rise to new and interesting findings which are not necessarily easy to spot on an industrial machine.

1.2 Research Objective

The objective of this research is to construct a bench scale express system that provides insight into the performance of tools operating under high stress and high temperature manufacturing conditions like machining. The overall goal of the research is to improve manufacturing processes. Machining is a common manufacturing process and according to Shaw, 3 distinct areas improve with increased machinability (M. C. Shaw 2005, 7):

1. Tool life increases.
2. Surface finish improves.

3. Energy usage of the machine decreases which increases efficiency.

This experimental unit in the field of tribology is typically termed a tribometer. This tribometer will interact a sample of tooling material and workpiece material under high stresses and high temperatures in a sliding action to produce similar frictional and wear performance characteristics that one would see if a similar test were reproduced on an industrial machine. In order to satisfy this objective the tribometer will need to be validated against machining tests with known results that can be trusted to be accurate and representative of the physical processes that take place. As good experimental practice, all future tribometer results should be scrutinized against machining results so that the procedure of tribometer testing is continually evolving and improving.

1.3 Research Scope

To satisfy the research objective the following tribometer design capabilities were desired:

Table 1.1: Operating Capabilities of the Proposed Tribometer

Normal Load Capabilities (Closed Loop)	0-2000N
Normal Stress for a 3mm Diameter Pin	0-4 GPa
Temperature Capabilities (Closed Loop)	20°C-975°C
Workpiece Rotational Speeds	0-1000RPM

These are typical loads, stresses, temperatures and rotational speeds seen in machining applications. The design setup will consist of a spherical tip pin (tooling material) which will be normally loaded against a flat disk material (workpiece material). The interface between the pin and disk will be heated to the

desired temperature. This simulates a tool pressing against a soft workpiece. This is a similar setup to a Brinell hardness test. The advantage of such a setup is that the contact mechanics are well established and the point contact of a sphere on a flat generates high stresses. This is advantageous when simulating machining conditions. The disk rotates counter clockwise. The pin is static and twists only due to the torque caused by the rotating disk. Torque is measured via a Kistler® 9329A micro reaction torque sensor (+/- 1Nm). The torque is a direct indicator of material sticking and the coefficient of friction under specific interface conditions.

The overall idea of the testing will be to have the capability to test numerous pins of tooling material such as tungsten carbide and high speed steel with various industry proven hard coatings as well as new novel coatings on various disks of workpiece materials. Due to testing and time constraints, Ti6Al4V and Inconel 718 will be the focus of this study for the coated and uncoated tungsten carbide tooling material. By testing numerous combinations of material, eventually a large matrix of tooling with various coatings can be plotted against workpieces for various processes at different loads and temperatures. The coefficient of friction (COF) and scanning electron microscope (SEM) data will be the studied outputs.

Visually the concept of this simulation is shown in Figure 1.1. The reader should be aware that in general no single experiment will sufficiently capture all aspects of machining. However, when carefully designed around the key variables, the value and significance of the model increases its value and functionality.

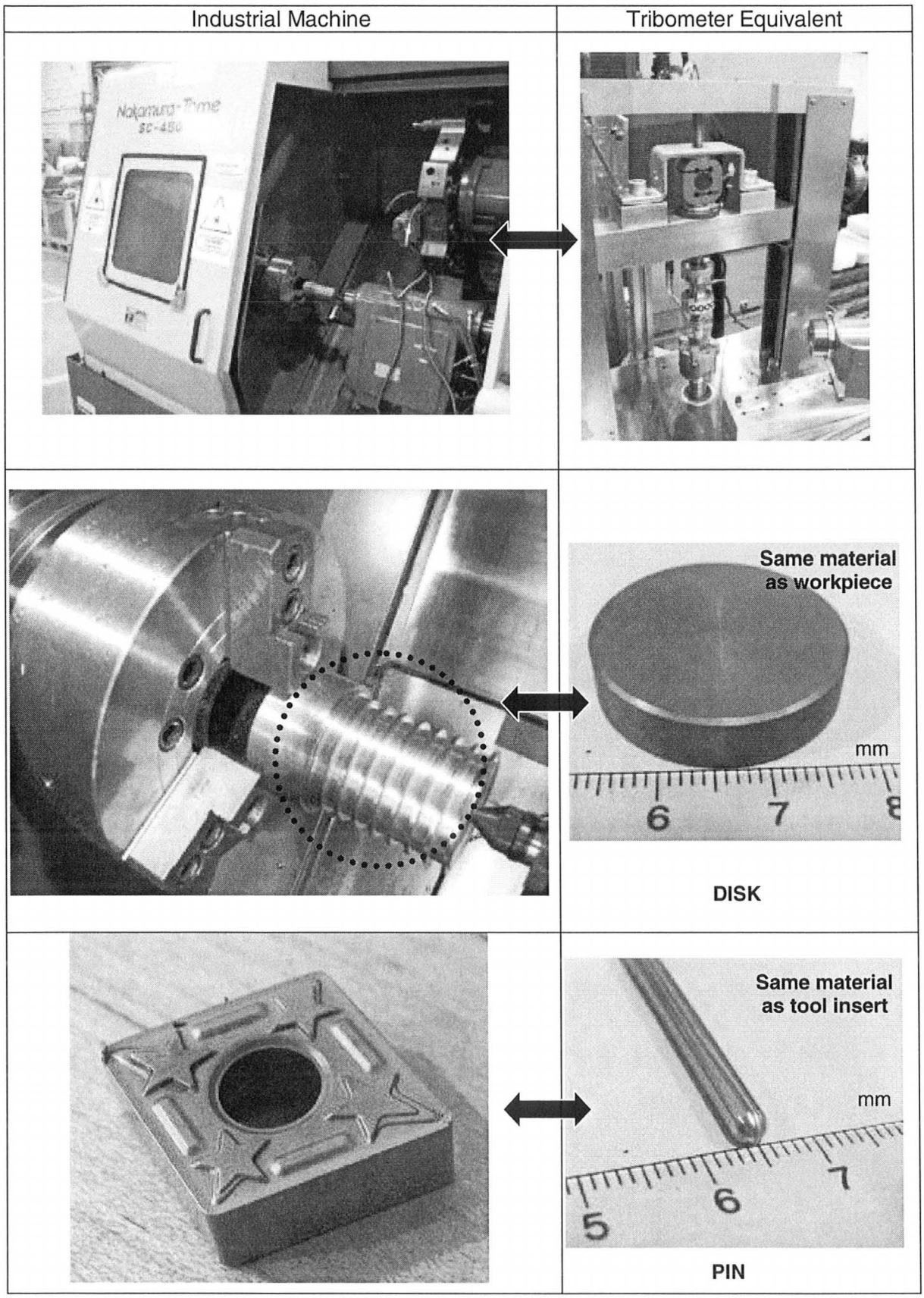

Figure 1.1: Machine vs. Tribometer Comparison

Chapter 2. Literature Survey

The following literature survey was structured to give sufficient background information on the fundamentals and design principles behind this body of research. The goal was to identify the key parameters and mechanisms that cause wear of tools and how to properly design and execute an efficient, reliable and accurate simulation of wear in metal cutting on a bench scale test. This literature survey has the following major components, listed in the order they are presented: 1) friction (action), 2) wear (result), 3) metal cutting (application) and 4) experimental design (simulate application). The overall scheme of this work is shown in Figure 2.1. All potential tribometer solutions must be validated on the real machine.

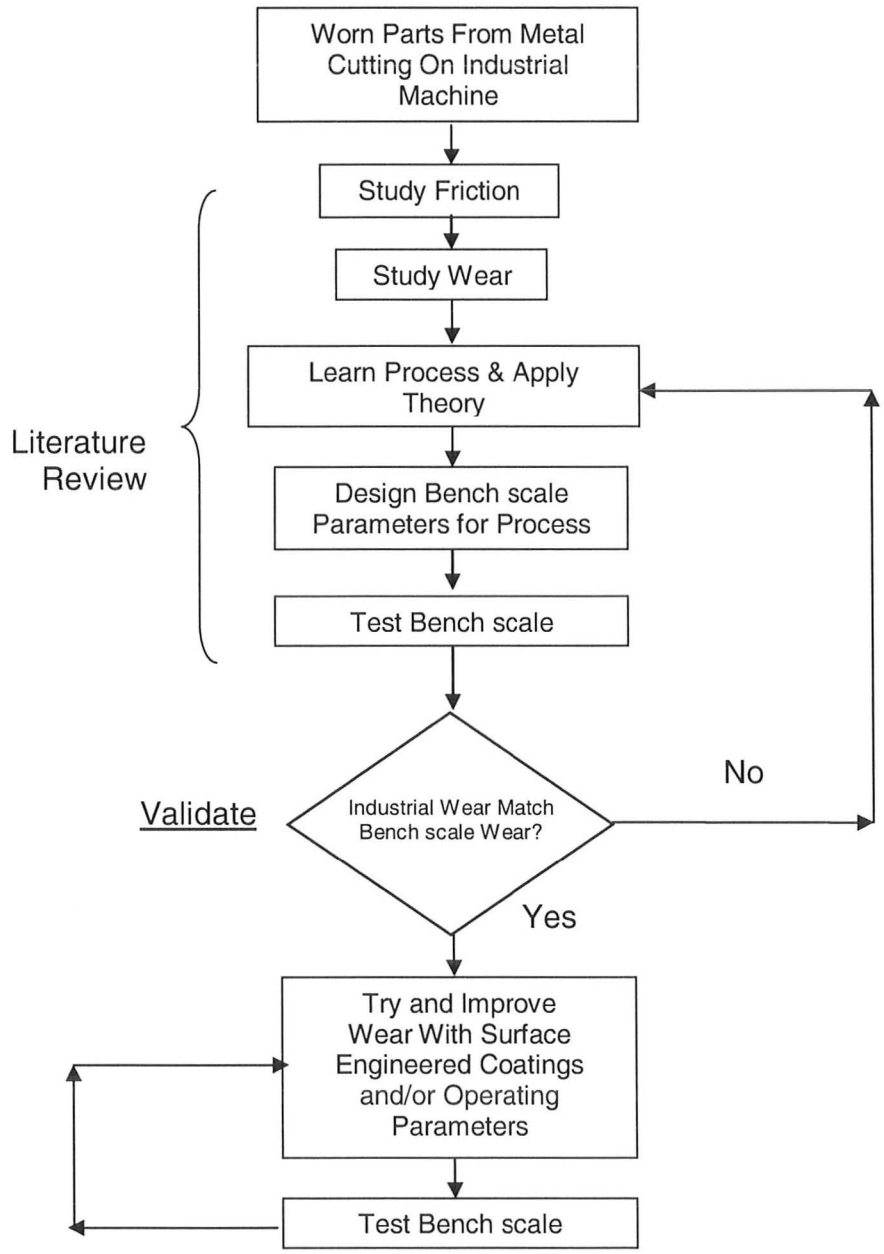

Figure 2.1: Testing Methodology

2.1 Fundamentals Principles of Friction

Friction is a major cause of wear. The focus here will be friction caused by the mechanical contact interaction of two surfaces sliding relative to each other. In general, friction is a tangential resistance across a projected area/interface under

normal load that tends to resist motion. In particular this work will focus on metal-metal interactions.

Friction is comprised primarily of a mechanical mechanism but chemical interactions do take place simultaneously. To fully appreciate friction and apply it to a wear situation, the fundamentals must be formed and understood. In general friction is dictated by: 1) surface geometry and material properties of both materials and 2) the operating conditions of the sliding (i.e. speed, pressure, temperature). Thus friction is not an individual material property but rather a function of a system. For the duration of this literature review, the two bodies in contact, body A and body B will be used for illustrative purposes. Body A will be harder than body B in all cases.

2.1.1 General Friction Free Body Diagram

It is extremely common in engineering applications that two materials will be in contact due to a normal load and will slide relative to each other. Such a scenario is sketched Figure 2.2. This is a simplification of the entire process but provides a good starting point.

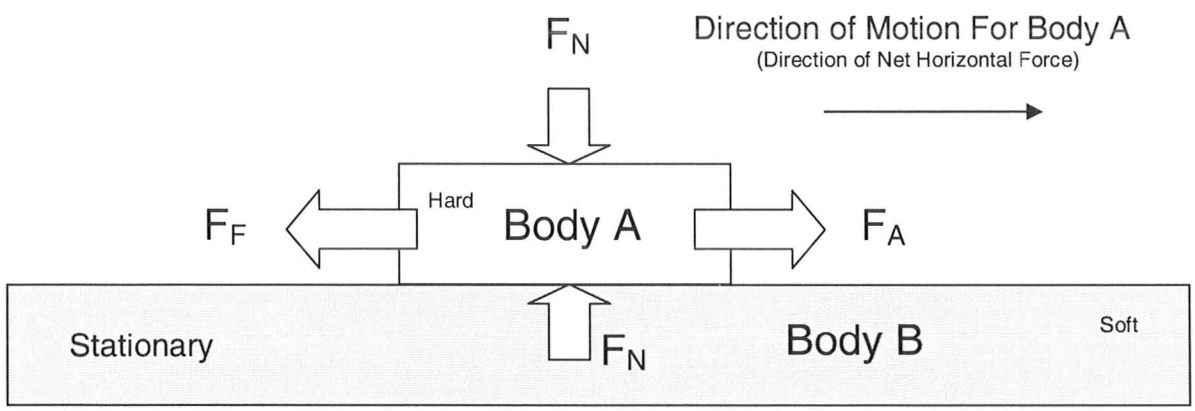

Figure 2.2: Free Body Diagram of the Friction Process

The friction will cause wear of both materials. However harder materials generally tend to wear less. To quantify friction and the subsequent wear, detailed analysis of this system must be completed.

2.1.2 Surface Interfaces – The Real Area of Contact

Typically it is the surface properties of the two interacting materials that play the largest role in dictating friction, with the bulk properties of the material beneath the surface of lesser importance. It is thus imperative before talking about forces, stresses and temperatures generated during friction to analyze the key geometrical features and material properties of surfaces and how they play a role in the friction process.

To the naked eye many surfaces look smooth on the macroscopic level but on the microscopic and nanoscale, most, if not all surfaces are far from perfect. Rabinowicz defines surface roughness as a departure or deviation from an ideal reference form or point (Rabinowicz 1995, 51). The term asperity is usually used to describe points of roughness. Typically either a stylus system or a laser interferometer can be used for roughness measurements. For measurements in our experiments, the laser interferometer is used as it provides a 3D plot of a surface section quickly with high resolution. It also offers the benefit of not causing wear or damage to the specimen. The laser model being used is a Zygo® NewView 5000 white light laser interferometer.

Typically surface roughness can be attributed to an R_A value which is more or less defined as an average deviation in height of the surface to a reference plane over a cut off distance. Other values such as R_Q and R_{PV} are commonly

used as well which are defined as the root mean square (rms) and peak to valley height difference respectively. The use of a single R_A value is debatable to some extent as markedly different surfaces may give the same R_A value (Arnell, et al. 1991, 7). Thus a friction tests may show different results for the same surface roughness R_A value. Thus typically multiple R values, such as R_A, R_Q and R_{PV} in addition to a 3D surface image will be reported when describing a surface. The Zygo® NewView 5000 white light interferometer calculates and reports all of these parameters as well as provides a 3D surface image. Due to the surface roughness, only a portion of the "apparent" contact area (A_A) is actually touching on both surfaces. These areas can be deemed as junctions or asperity interactions. The contacts that actually touch are deemed the "real" areas of contact (A_R). All frictional interactions take place in these real areas of contact. This is illustrated in Figure 2.3 if one looks at an enlarged version of a section between materials A and B

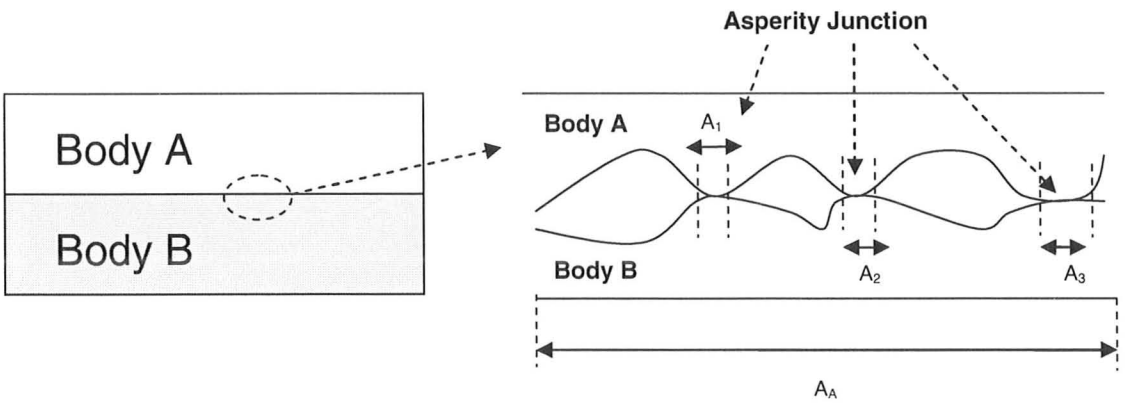

Figure 2.3: Real Area of Contact vs. Apparent Area of Contact

Thus the real area of contact is equal to the following:

$$A_R = \sum_{n=1}^{n=j} A_n \qquad \text{Equation 2.1}$$

Here n represents the junction number and j is the total number of junctions. The apparent area A_A is the projected area. Thus the following relationship can be highlighted:

$$0 < \frac{A_R}{A_A} \leq 1 \qquad \text{Equation 2.2}$$

When a system is lightly loaded or is very rough, the real area of contact is quite small compared to the apparent contact area. Thus the stress at each junction is significantly higher than the apparent compressive stress. As the load increases, the asperities flatten and the junction area grows. As a result the compressive stress is large at the beginning and gradually lowers. If this load is high enough the real area can approach the apparent area at which point the load no longer plays a significant role in contact. M.C Shaw notes that frictional sliding can be divided into two major categories: lightly load sliders (LLS) and heavy loaded sliders (HLS) (M. C. Shaw 2005, 154). Bowden and Tabor (Bowden and Tabor 1950) provide the following mechanism to explain how the asperities of materials interact. It is assumed for this mechanism that one material is harder than the other. Also it will be assumed that both asperities are spherical to start. As the load is applied the softer asperity will deform and eventually flatten as the real area of contact grows. The harder asperity will then make an indentation into the softer material. This is analogous to a Brinell hardness test. This work is also documented by Shaw (M. C. Shaw 2005, 160). The softer of the two materials will deform until the load is fully supported. The work of Bowden and Tabor has shown that as the load is increased the compressive stress will eventually become approximately uniform such that the compressive stress at the interface is

approximately 3 times the yield strength of the softer material, and the stress just beneath the surface of the softer material is equal to the yield strength of the softer material. This is the case when there is full plasticity. This is illustrated in Figure 2.4.

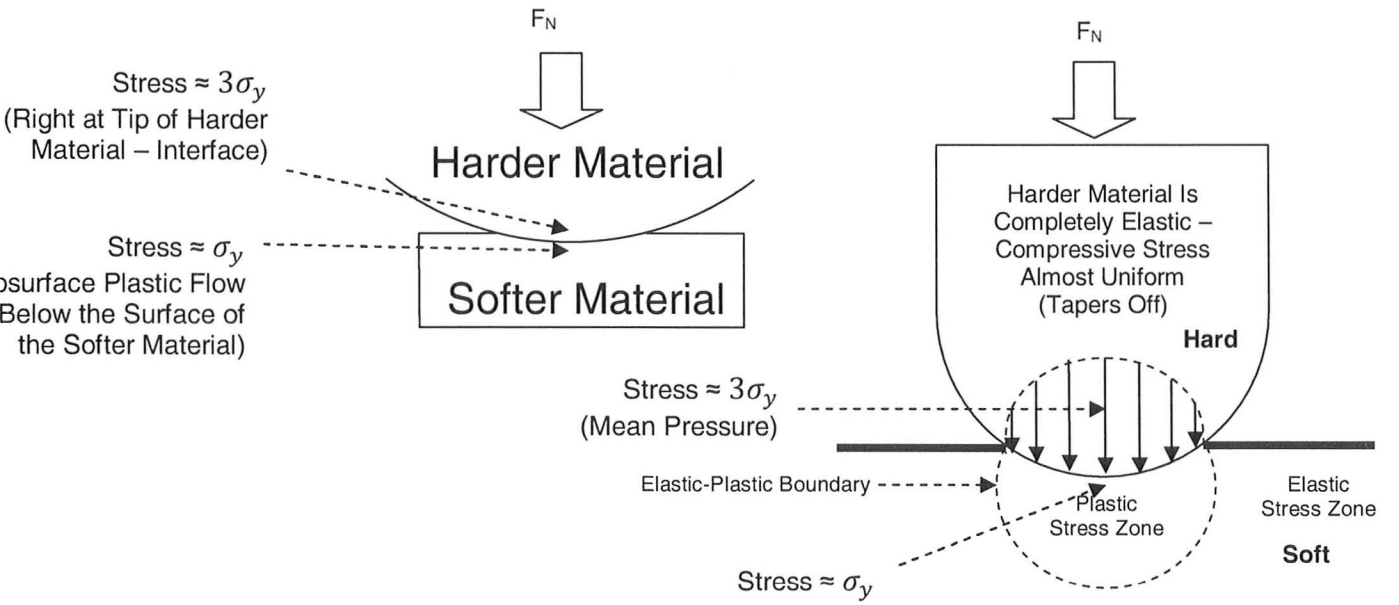

Figure 2.4: Stress Analysis of Asperities During Onset of Full Plasticity

The plastic zone is surrounded by elastic material to stop the spread of plastic flow. At this point the real area of contact will be approximately equal to the apparent area of contact. The interface stress of $3\sigma_Y$ is often referred to as the indentation hardness of the softer material (Rabinowicz 1995, 21). Bowden and Tabors findings were found to be relatively insensitive to the materials (lead, copper, steel) being used or the relative sizes. Thus, when the softer material is selected there is an estimated upper limit of the normal compressive stress ($3\sigma_y$) that is possible (Bowden and Tabor 1950, 13). Thus as many workpiece materials have yield strengths in the range of 0.5GPa to 1GPa, it is reasonable to expect that under heavy loads, the stress at such an interface would be somewhere

between 1.5 to 3GPa, hence the maximum design load for our experiments was set to 2000N for a 3mm diameter pin to produce these high stresses. The calculations for this load and pin design will be shown and verified in Chapter 3

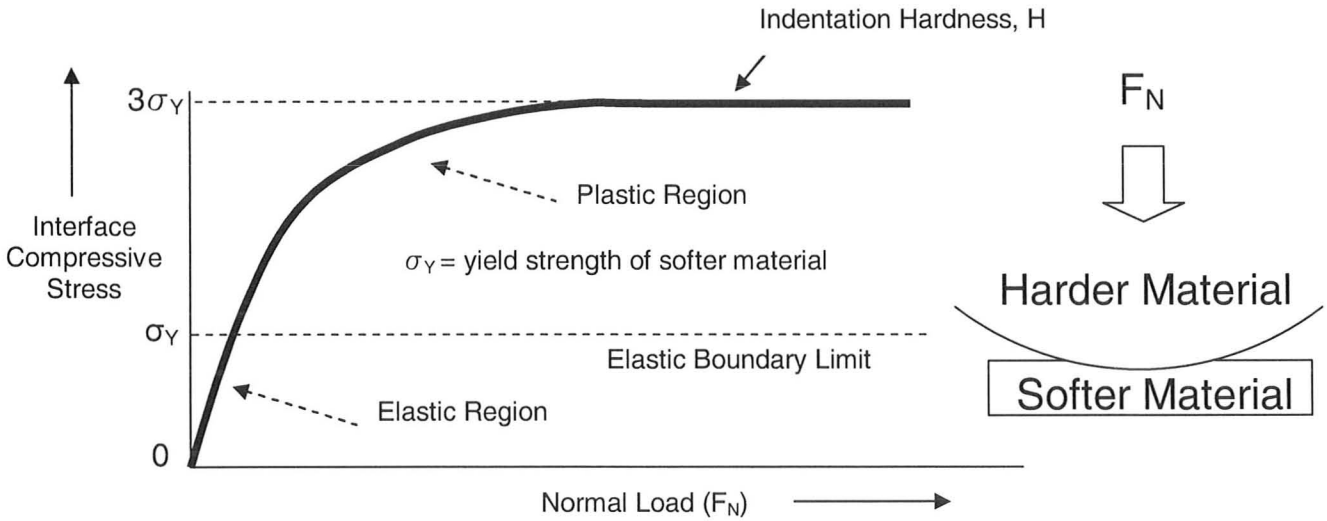

Figure 2.5: Relationship Between Compressive Stress and Normal Load

This analysis is also useful to define a guideline for approximating the magnitude of the real area of contact. If it is assumed that plastic deformation takes place on the softer of the asperities (which is highly likely) then according to Rabinowicz (Rabinowicz 1995) and the work established by Bowden and Tabor (Bowden and Tabor 1950), a minimum approximation of the real contact area can be made (Rabinowicz 1995, 45), as shown in Equation 2.3:

$$A_{R-MIN} \cong \frac{F_N}{H} = \frac{F_N}{3\sigma_y} \qquad \text{Equation 2.3}$$

Where F_N is the normal load in Newtons and H is the indentation hardness in Pascals. According to Shaw (M. C. Shaw 2005, 160), the onset of subsurface plastic flow will occur when the yield strength threshold is reached. This analysis is important as a limiting case as it will be shown later to apply to metal cutting.

Thus, as a minimum for a heavily loaded slider

$$\frac{A_R}{A_A} \cong = \frac{\sigma_y}{3\sigma_y} = \frac{1}{3} \qquad \text{Equation 2.4}$$

As an estimate, any system with A_R/A_A area ratio less than 1/3 can be roughly considered to be a lightly loaded slider case or if greater than 1/3 then a heavily loaded slider case. For a lightly loaded slider a Hertzian type elastic solution may be applied (Rabinowicz 1995, 47).

As a result, the real area of contact (for either LLS or HLS) is approximately bound by the following relationship as this is the smallest area possible based on indentation experiments:

$$\frac{F_N}{H} \leq A_R \leq A_A \qquad \text{Equation 2.5}$$

Finnie and Shaw noted that an approximate relationship for the real area of contact is as follows:

$$\frac{A_R}{A_A} = 1 - e^{-BF_N} \qquad \text{Equation 2.6}$$

Here B is a constant for the given material pair. Thus it can be seen that for a given material pair that as F_N is raised the real area of contact approaches the apparent area of contact. Shaw developed the following mechanism shown in Figure 2.6 to outline the response of materials to an increasing load.

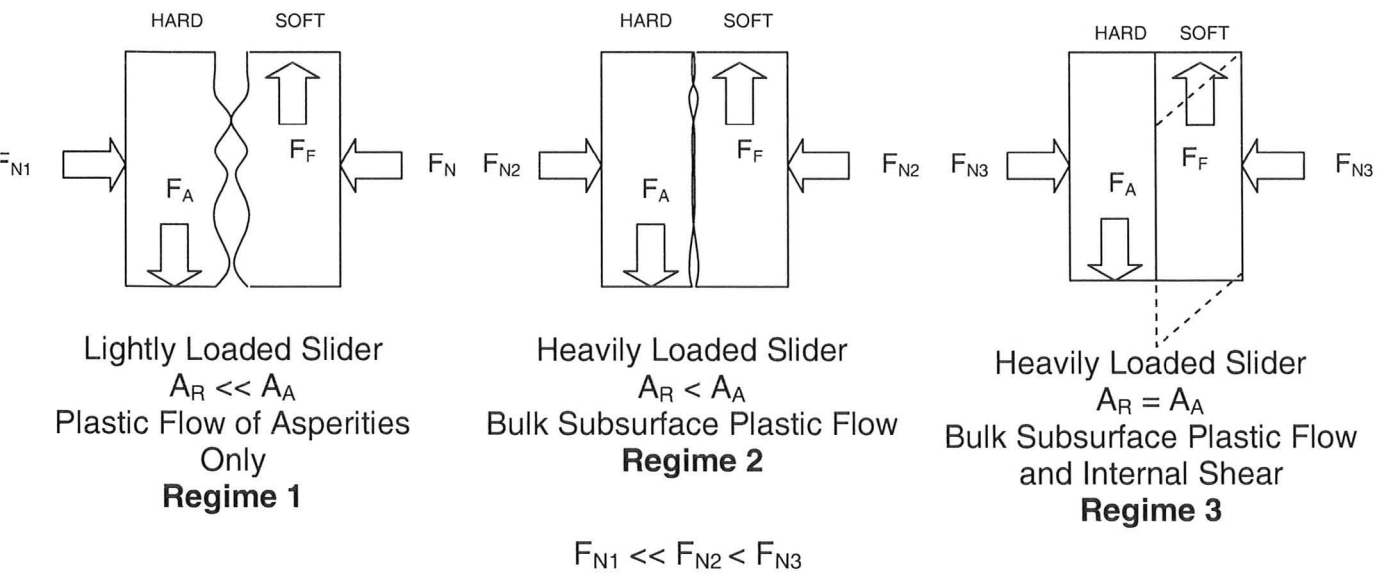

Figure 2.6: Effect of Increasing Load on Asperity Interaction

It is worth noting that the real contact area in general will increase if the following conditions are met (Rabinowicz 1995, 47-48):

- Surface roughnesses are lowered.
- Surfaces are sliding in shear. The real area of contact will increase with increased sliding distances possibly due to increase in conformity of the surfaces.
- The length of time in contact will tend to increase A_R.

2.1.3 Surface Films

It has been shown that the real area of contact between two surfaces account for the frictional behaviour. However the analysis thus far has made no reference to the surface films that typically exist on surfaces. As the surface layers dictate friction to a large extent, a film may change frictional properties significantly despite the nature of the real areas of contact. A typical surface in many environments and often in a manufacturing environment will contain multiple

sources of fluids that can deposit on the surface of a material and highly affect its frictional properties. Metals typically have high surface energies which attract films (Rabinowicz 1995, 89). A sketch of a common surface is shown below in a sketch adapted from Rabinowicz (Rabinowicz 1995, 82).

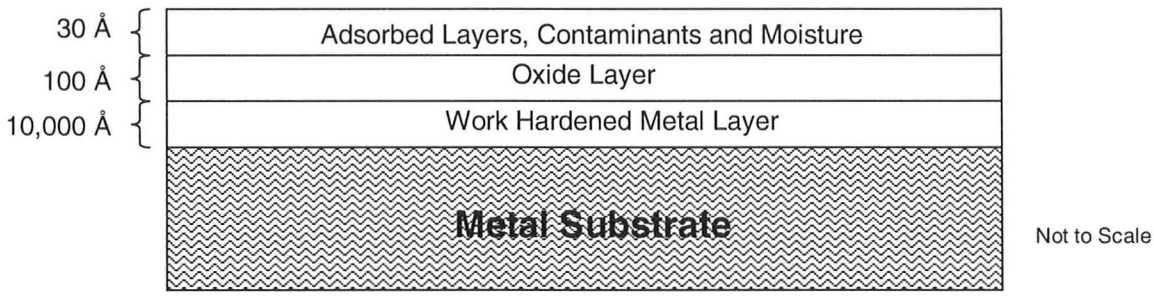

Figure 2.7: Typical Surface at the Microlevel

A work hardened layer usually is formed on the surface as part of its processing (i.e. grinding or turning) which is harder than the substrate metal. In general there will also be inclusions in the metal substrate and possibly trapped particles of lubrication from the manufacturing process (Arnell, et al. 1991, 2). Thus when a surface is prepared, all surfaces will be unique and one large asperity or misaligned inclusion could dominate the surface interaction (i.e. a large roughness peak). No matter how tight quality control is with regards to surface friction, every material is different even if they came off of an assembly line one after the other (Arnell, et al. 1991, 67). Furthermore the degree of contamination and adsorbed particles on the surface will vary from piece to piece and from surface to surface on the same material slab. All of these variables combined with the roughness of the surface result in an extremely complicated surface structure for which it is hard to predict its performance. A quote cited by Steele denotes the

struggle to predict surface characteristics. Steele noted the quote by renowned tribologist Wolfgang Pauli: "God made solids, but surfaces were made by the Devil" (Steele 2008, 1574). These layers may increase friction or decrease friction. In general these layers decrease friction as perfectly clean surfaces "cold weld" to each other in adhesion easily. As a result "mother nature" naturally provides lubricious layers to ease the sliding of materials.

2.1.4 Cause of Friction

Friction is caused by mechanical action of the contacting asperities. So far this analysis has been focused on the normal load/compressive stress and the nature of the surfaces interacting. When two surfaces slide or shear and plastic deformation occurs (which is almost always the case in friction) the friction will be dissipated as heat (product of friction force multiplied by velocity) almost 100% efficiently. Overall the temperature of the interface will rise during sliding. This increased temperature may promote "sticking" or adhesion which may increase friction. It is not uncommon in many applications that the real areas of contact will reach upwards of a few hundred degrees Celsius and in some cases as high as 1000°C (Trent and Wright, Metal Cutting 2000, 121). As the interacting surfaces are hidden from plane view this can be an astonishing result. However years of experiment, theoretical models and temperature sensing methods have confirmed that local extreme hotspots do occur and greatly influence the sliding. Due to these high temperatures, top layers of contaminants, adsorbed layers and/or moisture will be partially worn off or evaporate (Rabinowicz 1995, 82). According to Rabinowicz these contaminant layers are not completely removed by alcohols or

other organic solvents. The solvents in many cases may contain impurities or the surface may become re-contaminated quickly in a typical manufacturing environment. This is entirely possible in a machining environment with greases, lubricants and particles moving about in the air continuously. There is great difficulty in measuring these localized interacting temperatures reliably and accurately. A surface hidden from view may be cherry red while the outer bulk material visible to the naked eye looks the same as when the sliding initiated. This is also observed from many tests when the interacting surfaces are examined post test and show signs of extreme discolouring which is characteristic of having reached high temperatures at one point (i.e. metal chips). Also the hardness of many surfaces when post-tested indicate that high temperatures were often reached. Chemical processes such as diffusion become accelerated at these temperatures. Theoretical calculations tend to have errors for estimating these temperatures. According to the work of Rabinowicz it is generally observed that friction tends to rise with temperature due to adhesion until a peak value is reached. The friction then starts to decrease. This decrease in friction is termed by Rabinowicz as "melt lubrication" (Rabinowicz 1995, 116). Thus frictional temperatures play a large role in performance and wear and will be discussed in more detail in Chapter 3.

2.1.5 Mechanism of Friction

We have thus discussed the nature of surfaces interacting but what actually causes the friction? Adhesion is commonly used as a dominant mechanism in explaining the friction phenomenon. From a materials point of view, adhesion is

thought to be caused from the attraction of the surface atoms of two materials interacting at the real areas of contact. Adhesion is caused by loading surfaces normally and increased by tangential shearing (Rabinowicz 1995, 143-144) . Adhesion can occur at low or high temperatures. For example, metals like aluminum when pressed together will show adherence even at low temperatures, as the loading breaks the oxides formed on the surfaces and other films (Rabinowicz 1995, 77). Often the term "weld" is used as a qualitative description of adhesion. Rabinowicz gives a useful schematic of a typical adhesion joint. This is shown in Figure 2.8. The hexagons are shown to emphasize how grain boundaries and crystal structure can have an impact on the interaction.

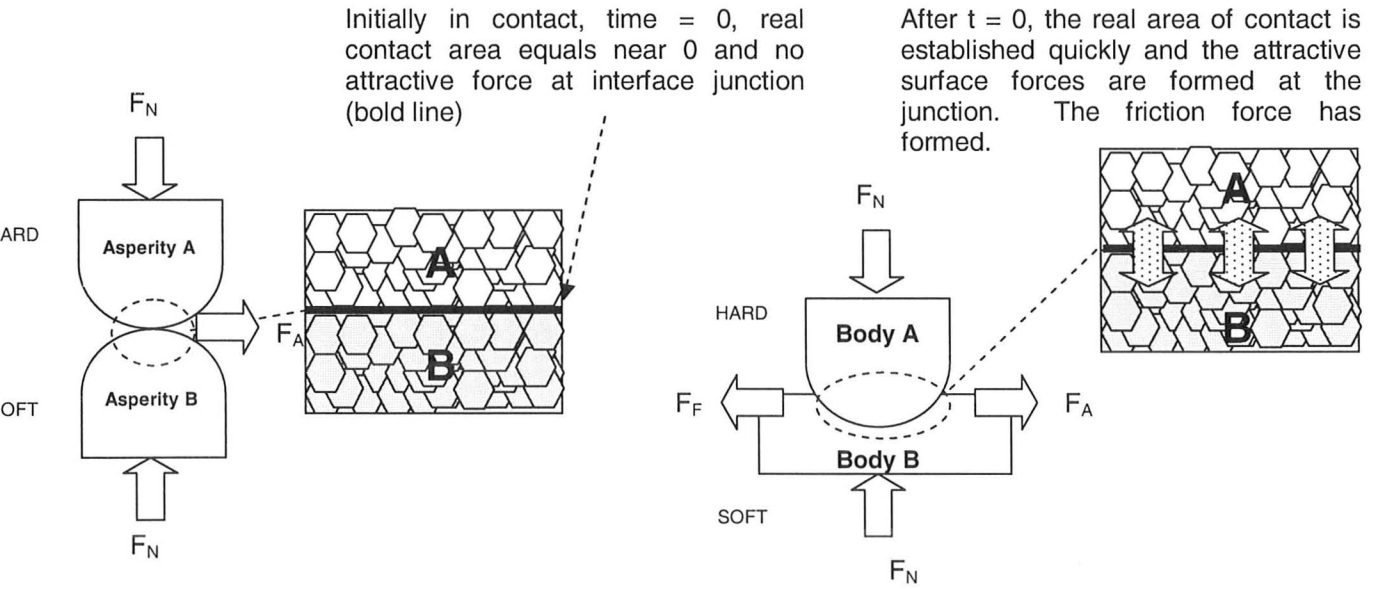

Figure 2.8: Qualitative View of Adhesion between Two Sliding Surfaces

Thus this "sticking" junction resistance is a major cause of friction. The junctions continually form and break in a cyclical fashion to maintain motion. Rabinowicz notes that approximately 90% of all friction is estimated to come from

the adhesion mechanism (Rabinowicz 1995, 78). Friction is also composed of a ploughing/abrasive term of resistance, a roughness/fatigue component as the asperities may need to rise over one another and an electrical resistance (Rabinowicz 1995, 80-81) component such that (F_F = Total Friction Force):

$$F_F = F_{Adhesion} + F_{Abrasion} + F_{Roughness} + F_{Electrical} \quad \text{Equation 2.7}$$

Equation 2.7 is usually simplified since the electrical component is often significantly less than the adhesive, abrasive and roughness components. Roughness and abrasion may be more dominant in very rough surfaces or surfaces containing hard inclusions but in many cases Equation 2.8 applies well. Adhesion will be most dominant as the real area approaches the apparent area under high loads and temperatures. However in general a case by case analysis is required for all scenarios to be accurate.

$$F_F \approx \underset{(90\%)}{F_{Adhesion}} + \underset{(5\%)}{F_{Abrasion}} + \underset{(5\%)}{F_{Roughness}} \quad \text{Equation 2.8}$$

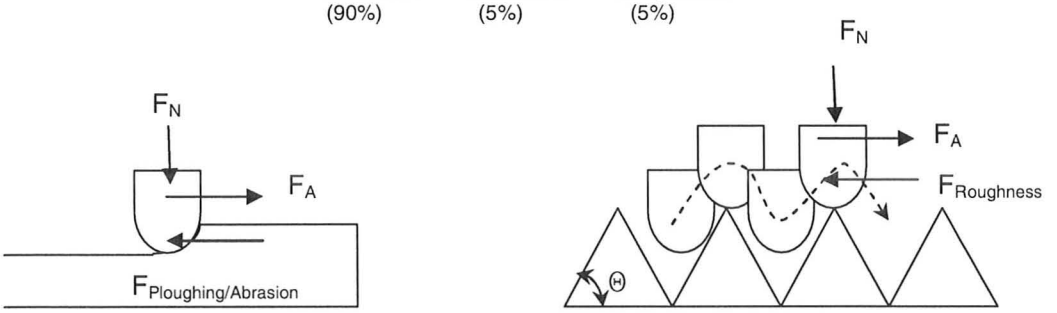

Figure 2.9: Illustration of Abrasive and Roughness Component of Friction

Rabinowicz notes that as a first approximation the coefficient of friction of a material may be estimated as follows based on the properties of the softer material as seen in Equation 2.9. The angle Θ in this case is an average roughness angle (interpreted as the slope of a triangle). This definition of COF is not complete, nor completely correct but it is a good introduction (Rabinowicz 1995, 69).

$$\mu = \frac{F_F}{F_N} \cong \frac{shear\ strength}{hardness} + \frac{tan\Theta}{\pi} \qquad \text{Equation 2.9}$$

Adhesion will be looked at in closer detail since it is widely considered the largest component of friction and is the focus of this thesis. In some cases the interface may be stronger than the shear strength of the materials and the softer (most often) or harder material will shear off and be stuck to the opposing material or be a free wear particle. This is discussed in more detail in Chapter 3. However in most cases it is postulated that the junction shears leaving no wear. Figure 2.10 illustrates the 3 cases that may occur when an adhesive bond forms and breaks.

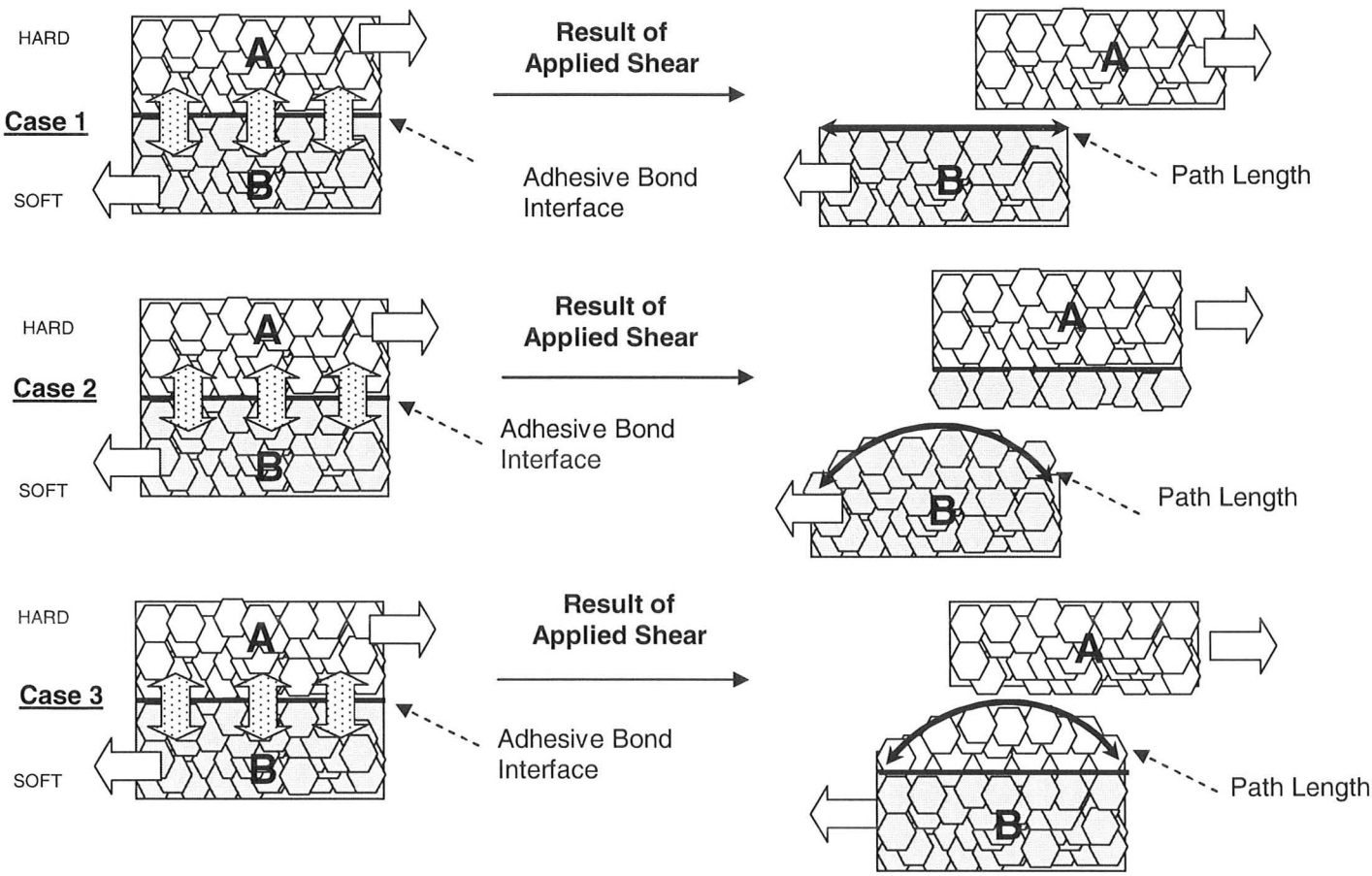

Figure 2.10: Illustration of the 3 Possible Cases of Adhesion at the Material Interface

Most tribologists agree that case 1 is far more probable than cases 2 and 3. In general Case 2 is about 1-10% of all scenarios according to Rabinowicz. This indicates that the junction of the two materials must have a comparable strength (similar magnitude) to the shear strength of the weaker material as a first estimate (Rabinowicz 1995, 75). Case 3 is the least probable as it implies that the softer material is pulling material from the harder material. All 3 of these cases may be taking place at the same time over numerous junctions between the materials. As a result the overall adhesive friction force will be the result of a distribution of the three cases outlined. However it is Case 3 that we are most concerned about in manufacturing and even though the incidence is rare, the impact on tool life is significant. It is also interesting to note that Case 2 can lead to instances of Case 3 as soft workpiece material builds up and pulls tool material out with it.

$$F_F \cong \sum F_{F-Case\,1} + \sum F_{F-Case\,2} + \sum F_{F-Case\,3} \qquad \text{Equation 2.10}$$

The interface is hypothesized to be the most common one that is breaking due to the path length of the interface bond being shorter than the path within the material, thus less energy is required to break the bond (Rabinowicz 1995, 149). Case 3 is the example of when a built up edge (BUE) is removed from a tool face. Experiments completed by Green (1955) and Greenwood and Tabor (1955, 1957) denote a possibility for Case 3 for one or a combination for the following reasons as seen in Table 2.1.

Table 2.1: Possible Explanations for Case 3

Possible Cause for Case 3	Explanation
Fatigue Viewpoint:	Bayer et al (1972) and Halling contest that in sliding, the stress changes cause fatigue within the harder material causing it to become weaker than its original state.
Statistical Viewpoint:	The harder material will have fluctuating properties from its manufacture and there may be non-uniform stress profiles in the contact zone. This was postulated by Rabinowicz in 1981.
Delaminating Viewpoint	There are cracks in the harder material beneath the surface during manufacture or due to fatigue loading.
Path Length Viewpoint:	The interface may not be perfectly horizontal, thus allowing the path length of shear within the materials to be shorter than that of the junction.

2.1.6 Coefficient of Friction

It has been established that friction dominantly results from the adhesive resistive force of interacting asperities over the real area of contact during sliding. Now that the cause and the mechanism have been approached it is important to quantify the value of friction. In most manufacturing tool cases friction is desired to be low to reduce wear and extend tool life.

To date, the most common way of quantifying the amount of friction is through the use of the coefficient of friction as introduced in Equation 2.9. Assuming the objects in our analysis are always moving we are thus concerned with the kinematic coefficient of friction, μ_K as defined below (in all subsequent cases μ_K will be simply stated as μ or COF):

$$\mu = \frac{F_F}{F_N} = \frac{\tau}{\sigma} \qquad \text{Equation 2.11}$$

Here F_F is the kinematic friction force, F_N is the normal load, τ is the frictional shear stress and σ normal compressive stress. It is common in

handbooks for friction to be represented by the coefficient of friction which is listed typically as a constant. In reality this is highly simplified, as friction is naturally chaotic and will change often when critical parameters change. Thus there is great importance in conveying how this coefficient changes and in establishing the most critical parameters (Stachowiak 2004, 323). As a result, coefficient of friction is better represented as an average of several samples and reporting the standard deviation of the data (Stachowiak 2004, 79) and the conditions under which it was established. Typically the normal load is fairly easily quantifiable in a situation. It may simply be due to the force of gravity and/or an applied force which can be measured by a dynamometer force sensor. The friction force may also be measured by a dynamometer as the force perpendicular to the normal force. Often a dynamometer with 1-3 axes (X, Y, Z) is used to accurately measure the forces simultaneously with high resolution and minimal cross-talk. If the surfaces are sliding at a constant velocity then the applied force will equal the opposing reaction force which in this case is the friction force.

To gain a full appreciation of the coefficient of friction, it is important to place some additional theory behind the value of the coefficient of friction, mainly what material parameters affect the value and what range of values are typically expected for a COF value. It is imperative when designing an experiment to know these derivations as it will provide a range of values to determine if the setup and sensors are working and also provide a framework of how to tune the friction value from a design perspective. The adhesion model will continue to be used in this

analysis. In general the energy of adhesion or rather the energy required to separate the adhesive interface is written as an equation as follows.

$$W = C_m(\gamma_{A+}\gamma_B) \qquad \text{Equation 2.12}$$

W, is the work of adhesion (J/m^2), C_m is the material compatibility factor which is a function of the two materials and γ_A and γ_B are the surface energies of the two materials respectively. It is important to note that compatibility, C_m does not mean that the atoms of both metals interdiffuse into each other (Rabinowicz 1995, 86). Figure 2.11 highlights these material compatibilities. The sketch is based on the works of Hansen and Anderko (1958), Elliot (1965), Shunk (1969) and Moffatt (1987). In general like materials strongly adhere and dissimilar materials weakly adhere based on binary solubility theory.

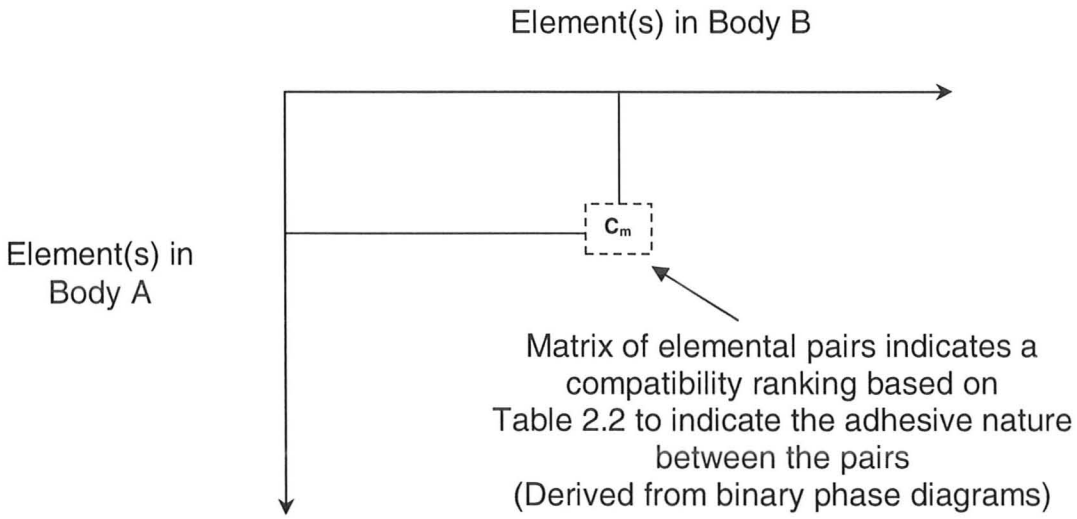

Figure 2.11: Material Compatibility Chart

Table 2.2: Material Compatibility Parameter Values From Rabinowicz

	Identical	Compatible	Partially Compatible	Partially Incompatible	Incompatible
C_m	1	0.5	0.32	0.2	0.12

Solubility increase ← → Solubility Decrease

Rabinowicz has reported the following general trends for COF as a function of material compatibility and lubrication for metals. This work was compiled from experiments conducted by Rabinowicz, Bowden and Tabor. Overall it shows that a lubricant and the compatibility of materials involved play a role in establishing the COF between metals (Rabinowicz 1995, 118-119).

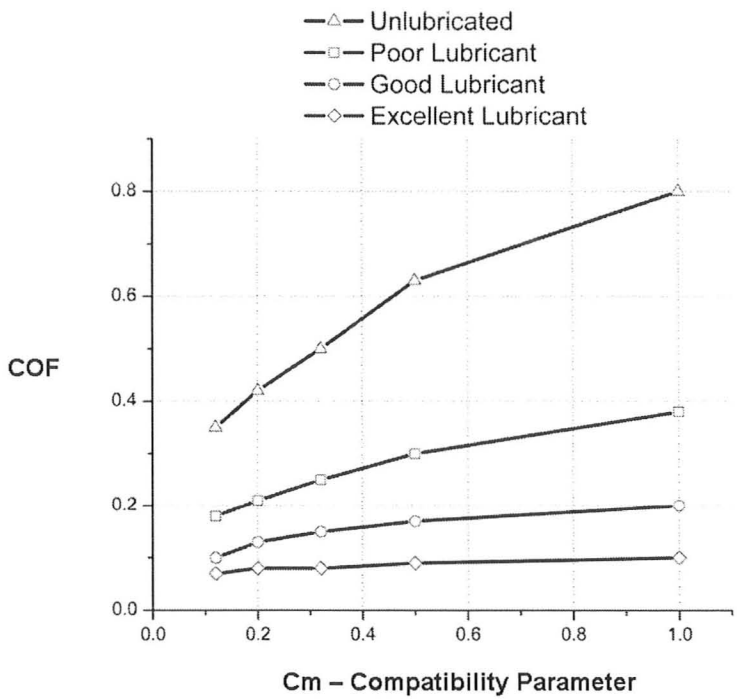

Figure 2.12: Generalized Effects of Lubrication and Material Compatibility on COF

The surface energy will increase as one gets further from the melting point and will decrease with the presence of oxides and other films that have been adsorbed on the surface. Freshly generated surfaces tend to be very chemically active (adhesive) as they have few adsorbed films and contaminants. This will lead to a higher surface energy when this surface is formed compared to its lower equilibrium value once exposed to the environment (M. C. Shaw 2005, 155). It is important to note the following relationship between surface energy and hardness in Equation 2.13.

$$\text{Surface Energy} \propto \text{Hardness}^{0.5} \qquad \text{Equation 2.13}$$

Tungsten has one of the highest surface energies at 2300 mJ/m^2. In general Rabinowicz postulated that the ratio of γ/H is a good indicator of friction and wear. In general a lower ratio of γ/H will produce:

- Lower coefficient of friction
- Less Wear (i.e. less and smaller wear particles)
- Lower Surface Roughness
- Less Adhesive Interaction

It is interesting to note that Tungsten has a γ/H tabulated at around 5.3 x 10^{-8} cm. This is one of the lowest ratios indicating Tungsten is a strong choice for low friction and wear. Thus it stands to reason why it is used in metal cutting! As a comparison, the following values for γ/H (x 10^{-8} cm) are listed for common materials:

- Tungsten (W) – 5.3 → Starting point for cemented carbides
- Iron (Fe) – 18 → Starting point for HSS (eventually heat treated)
- Aluminum (Al) – 33
- Lead (Pb) – 110
- Sodium (Na) - 2800

Rabinowicz notes that no matter how hard you make one of the materials, material is still going to be removed by some degree from the harder material. As mentioned the junction strength is comparable to the shear strength (S) of the softer material. Thus if the real area of contact is used and the strength properties

of the softer material is applied, an initial estimate of the magnitude COF can be completed. As noted, the general trend is that the compressive stress at the interface cannot exceed approximately 3 times the yield strength of the softer material and just below the surface of the softer material, the compressive stress is the yield stress. As a result, there is often a discrepancy as to which stress to use, $3\sigma_Y$ (often written as H, penetration hardness) or σ_Y to calculate COF. Bowden and Tabor use σ_Y which implies the stress within the softer material and that softer material is removed and Rabinowicz uses $3\sigma_Y$ which is the value at the interface implying that the interface breaks. As a result, by using both normal stresses to bound the solution, we can estimate the following:

$$F_{N-min} \cong \sigma_Y A_r \qquad \text{Equation 2.14}$$

$$F_{N-max} \cong HA_r \cong 3\sigma_Y A_r \qquad \text{Equation 2.15}$$

For the frictional force,

$$F_{friction} \cong SA_r \qquad \text{Equation 2.16}$$

We can write the following expressions, noting that in most cases S is equal to approximately ½ the value of the yield strength of most metals:

$$S \cong \frac{1}{2}\sigma_Y \qquad \text{Equation 2.17}$$

Thus as a first approximation, the coefficient of friction is bounded by the following minimum and maximum values.

$$\mu_{min} = \frac{F_F}{F_N} \cong \frac{SA_r}{3\sigma_Y A_r} \cong \frac{1}{6} \cong 0.17 \qquad \text{Equation 2.18}$$

$$\mu_{max} = \frac{F_F}{F_N} \cong \frac{SA_r}{\sigma_Y A_r} \cong \frac{1}{2} \cong 0.50 \qquad \text{Equation 2.19}$$

Thus friction is less if the interface shears rather than if the softer material shears, which makes physical sense. Thus it would be expected based on this analysis that COF should lie between approximately 0.17-0.50. In the case of 0.17, this represents the value for the case when the bond breaks at the interface whereas the 0.50 case represents the case where the bond breaks within the softer material. However as noted, not all junction breaks are the same and as a result there may be a distribution (i.e. normal distribution) of junction breakages thus, any estimate of COF should be considered as a bulk or lumped average of all cases. There is however a fault associated with this analysis. It implies that the COF is dictated only by the properties of the softer material and by adhesion. This is known to be false, as friction is a system parameter, meaning it is a function of both materials, the nature of the sliding and the conditions of the external environment (Arnell, et al. 1991, 35). From the above analysis it is also worth mentioning that it initially appears that COF can never be greater than 1 because the shear strength in general can never exceed the yield strength of the material. Furthermore, it was noted that the real area of contact plays the major role in friction yet it simply divides out in this calculation. While this analysis agrees with many experimental results, it is just a starting point to help find the important parameters and more or less provide a generally accepted range of values of COF. In reality the real area of contact will greatly affect the value of COF.

Most values reported by Rabinowicz for COF of metals are around 0.05 to 1 which implies there is more to the analysis. Abrasion and roughness could be more significant than the 5%-10% value listed by Rabinowicz. Arnell also has

reported COF on the order of 0.1-1 (Arnell, et al. 1991, 66). Research has shown that indeed COF can exceed 1 but typically in only rare situations. These are situations where the surfaces are perfectly clean (i.e. no oxide, no lubricants, no moisture and in a vacuum environment), where the real area of contact approaches the apparent area of contact and under vacuum like conditions. Furthermore some surfaces may have COF less than 0.17 because what is termed a 3rd body may exist between the two surfaces. This may be a solid with lower shear strength than either material or a lubricant fluid which will shear easily while supporting the load between the two materials. Thus there is no unified theory of friction and under certain conditions the mechanisms may change or other mechanisms may shift to a more dominant form. Nevertheless the concept of adhesion together with the ratio of shear strength to yield strength provides a decent estimation and a framework for looking at friction. In general it suggests that to lower friction, one would like to devise a low shear strength film (i.e. coating or lubricant) or material (i.e. graphite or sulphide) at the interface which is supported by surfaces with high hardness. Thus it is worth noting that friction modelling and experiment is typically empirical in nature due to no general governing mechanism and as a result a more appropriate equation for COF would be:

$$0 < \mu = C\frac{S}{\sigma_Y} \leq 1 \qquad \text{Equation 2.20}$$

Here C is a constant that depends on the nature of the materials, the operating conditions and the external environment, S is the shear strength of the softer material and σ_Y is the yield strength of the softer material. If a lubricant,

coating or 3rd body solid is used, this could be factored into the constant C. Thus in general engineering applications, if COF is calculated out of the range of about 0.05-1, some or all of the following scenarios may exist:

- The mathematical equations derived for COF in the experiment may contain an error.
- The sensors used may be calibrated poorly and/or are measuring other forces (i.e. friction plus some other forces).
- The system is operating on extremely clean surfaces under high load with materials of high compatibility (i.e. copper on copper, high C_m and low yield strength).
- The system is extremely rough and ploughing and roughness forces become dominant.
- The temperatures of the system are extremely low or high (either due to high sliding speed or external influence).

Typically the COF is thought to be independent of velocity within an order of magnitude. For most applications this is true, however with large increases or decreases there is a definite effect. Rabinowicz reports this from the work of Barwell in 1956. This finding on the weak dependence on sliding velocity within a certain range is also supported by the work of Arnell (Arnell, et al. 1991, 27).

2.1.7 Summary of Parameters That Affect Friction

To illustrate the complexity of friction, a summary table is provided based on an extensive literature review of the common parameters that affect friction. In general the tribological interaction of two or more materials will depend on the following 3 categories: 1) Operating/System Parameters, 2) Material Parameters and 3) Environmental Conditions (Stachowiak 2004, 9). It may appear that system parameters should be classified with environmental parameters. While some may argue this is true, the two are made distinct here based on the following reasoning: system parameters are assumed within reasonable control or adjustment by the user while environmental parameters at times may be out of the control of the user and are a unique variable based on day to day operations.

Table 2.3: Summary of Parameters that Affect Friction

Operating/System Parameters	Material Parameters	Environmental Parameters
Sliding Speed	Yield Strength	Humidity
Surface Finish/Roughness	Hardness	Oxygen Partial Pressure
Coatings	Young's Modulus	Ambient Temperature
Load/Stress	Fracture Toughness	
Shear/Shear Rate	Thermal Conductivity	
Strain/Strain Rate	Melting Point	
Sliding Distance/# Parts/Time	Surface Energy	
Contact: Formal or Non-Conformal	Grain Size	
Material Compatibility/Materials (i.e. mutual solubility)	Electrochemical Potential	
Lubrication	Inclusions	
Contamination/Adsorbed Films	Atomic Structure (FCC, BCC, HCP)	
Motion: Linear, Reciprocating, Rolling		

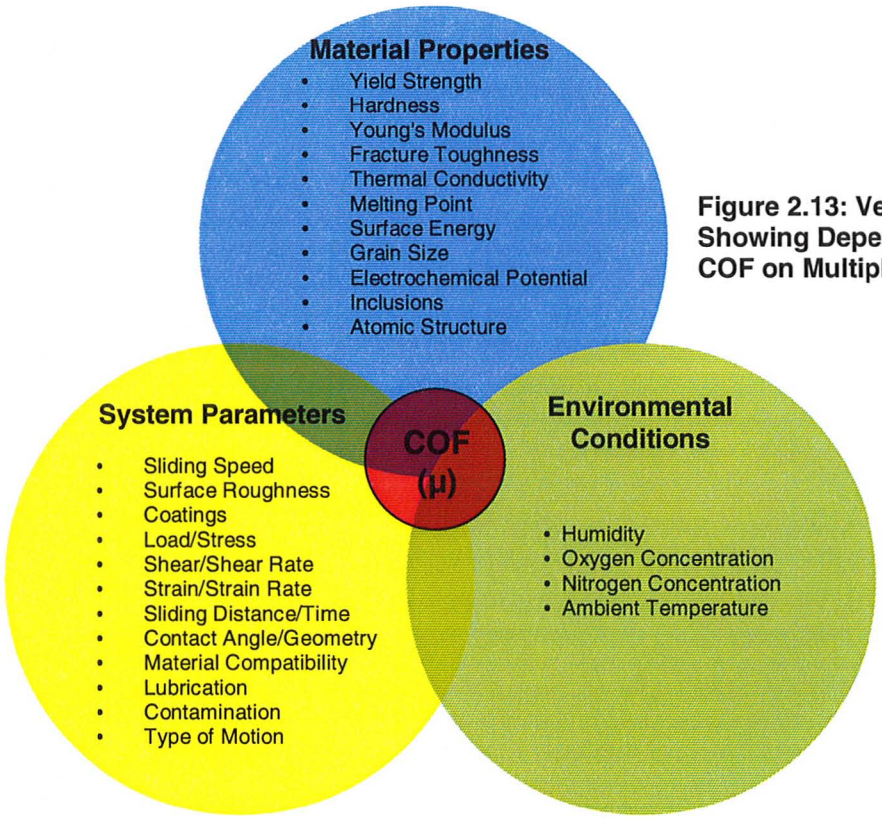

Figure 2.13: Venn Diagram Showing Dependency of COF on Multiple Factors

As mentioned, friction is often classically divided into two categories: lightly and heavily loaded sliders. The division between the two regimes according to the observations of Shaw and shown earlier is approximately when the real area of contact is 1/3 the apparent contact area. Table 2.4 is a summary for the laws of friction observed for both lightly loaded and heavily loaded sliders. Shaw supports the majority of the effects listed in this chart (M. C. Shaw 2005, 156). These observations are generally true within 1 or 2 magnitudes of change for each variable with regards to its effect on COF.

Table 2.4: Comparison of Lightly Loaded and Heavily Loaded Sliders

	Effect of Increasing Variables on COF	
Effect of Increasing:	Lightly Loaded Sliders ($A_R < 1/3A_A$)	Heavily Loaded Sliders ($A_R > 1/3A_A$)
Apparent Contact Area, A_A	None	None
Load, F_N	Negligible	Decrease
Velocity, V	Increase or Decrease	Increase or Decrease
Surface Roughness, R_a	Negligible	Negligible
Temperature, T	Increase or Decrease	Increase or Decrease
Surface Energy, γ	Increase	Increase
Shear Strength, σ_S	Increase	Increase
Hardness, H	Decrease	Decrease
Materials Compatibility, C_m	Increase	Increase

A few general comments about the chart above for velocity and roughness:

- The effect of velocity appears to be more due to thermal/chemical effects (softening, oxides, films etc) rather than mechanical effects as cited by Rabinowicz. The strength of most solids is not affected greatly by the rate of application of stress within an order of magnitude. (Rabinowicz 1995, 72-73). Increasing velocity will increase temperature and vice versa.
- The coefficient of friction tends to be relatively independent of surface roughness within an order of magnitude. As mentioned by Rabinowicz, 90% of friction is thought to be from adhesion. However, surface roughness may have pronounced effect on extremely smooth (mirror finish) or extremely rough surfaces. Under high stresses, when the real contact area approaches the apparent contact area, the effect of initial roughness becomes negligible as the asperities are flattened and conform to the geometry of the loaded surfaces.

As for the load effect, the work of M.C. Shaw has found the following general trend for frictional shear stress (τ) vs. the normal compressive stress (σ) as

illustrated in Figure 2.14 (M. C. Shaw 2005, 162). Region 1 is the lightly loaded slider region and regions 2 and 3 are the heavily loaded slider regions. Region 1 is the typical region for Amonton's Law of friction which is the classical ratio of friction force to normal force or conversely the frictional shear stress to the normal compressive stress.

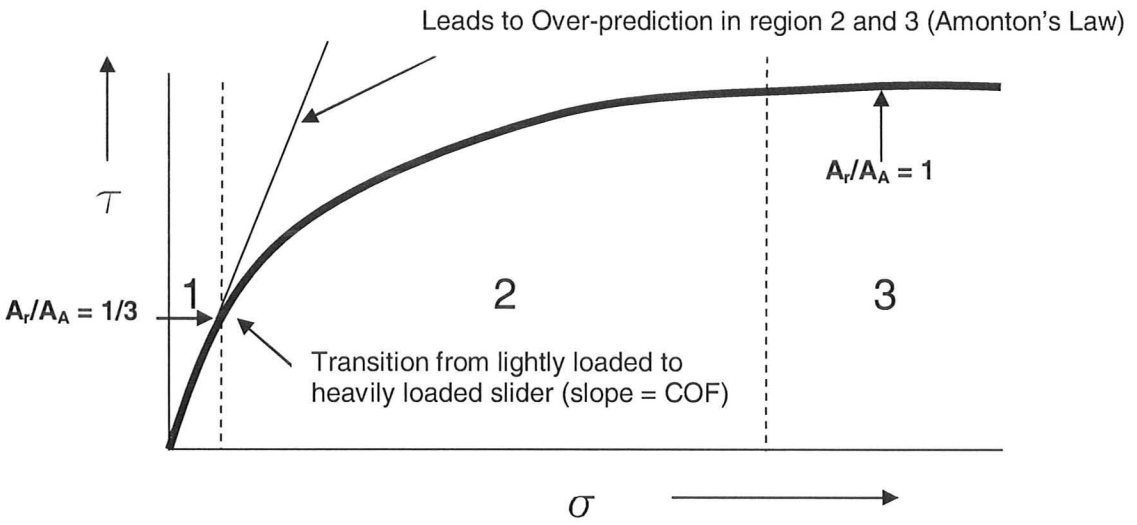

Figure 2.14: Evolution of Frictional Shear Stress and Normal Stress for LLS and HLS

As the loads increase into region 2 and 3 the asperities flatten and approach the real contact area. In regions 2 and 3 the relationship for COF is non-linear and junction growth is occurring. In region 3 the real area has approached the apparent contact area and load has minimal affect on COF. This trend however does not take into account the role of temperature or the effects of coatings or lubrication.

2.2 Fundamental Principles of Wear

Wear is a relative term. It often implies damage to a part from interaction with a mating part and/or an environment. However, depending on the application and the conditions, different types of wear exist. Wear may be defined by volume

of material removed or a change in surface finish. These varying wear types are often measured and analyzed in different ways. The amount of acceptable wear for a part to still function properly is entirely dependent on the application and no universal wear criteria exist although some standards have been developed. To further complicate matters multiple wear modes may exist simultaneously which leads to difficulty in determining which wear modes are most dominant in an application. If the surfaces become damaged aggressively, multiple wear modes may interact to confuse the analysis. The goal of this section will be to outline what mechanisms fundamentally tend to initiate wear, the common types of wear that exist and the methods/analysis of wear commonly employed in engineering practice. There is no general universal rule that states that friction and wear are always related and directly proportional. While a direct relationship between friction and wear is true in many cases caution should always be aired (Finkin 1979, 155). For this analysis, based on an extensive literature review and testing experience it will be postulated that reducing friction, will reduce wear and vice versa.

2.2.1 Relationship between Friction and Wear

Friction is commonly cited as a major cause or mechanism that initiates wear. Often wear is directly proportional to friction. Whether it is the adhesive wear particles formed, abrasion of hard particles ploughing a soft material, or the high temperatures generated causing diffusion of one material to the other, friction is often a pre-cursor to wear. Caution should always be aired when comparing friction to wear. For example two surfaces may exhibit very low COF values but

due to a manufacturing error there are localized rough spots. These rough spots may totally dominate the wear process despite lab tests indicating that the two surfaces show excellent low friction properties. To add to this abrasive example, it is postulated that low friction in some cases may lead to high wear because the loose wear particles that reduce friction (i.e. as a 3rd body particle) may act as an abrasive to increase wear (Rabinowicz 1995, 167). While adhesion is the dominant friction mechanism in some cases it may not be the dominant wear mechanism, as is the case with materials with hard inclusions. Thus the occurrence of each type of wear mechanism can be thought of as a probability (i.e. probability of friction mechanism existing x probability friction mechanism causing wear) (Koshy, Manufacturing Processes Lecture 2010). In the case of low velocity, with minimal inclusions, real area equal close to apparent area under high temperature it is assumed that adhesive friction and adhesive wear have very high probabilities. This will be shown in Archard's adhesive wear equation which will be outlined. In general the relationship between adhesive friction and wear is thought to be such that wear is proportional to μ^4 for metal interactions (Rabinowicz 1995, 167).

2.2.2 Adhesive Wear

Often the terms galling or attrition wear may be used to describe adhesive wear. To model adhesive wear Archard developed a simple asperity model to account for adhesive wear. The derivation shown below is adapted from the treatment by Rabinowicz (Rabinowicz 1995, 156-158). First Archard assumed that the two contacting asperities are spheres. The harder sphere under normal load

compresses the softer sphere until the softer material deforms plastically and can support the load. At this point two assumptions are made: first that the stress at the tip of the harder material is equal to the indentation hardness of the softer material (i.e. $3\sigma_Y$ of the softer material) and that the contact area is a circle.

It can be estimated that:

$$F_N = HA_R \qquad \text{Equation 2.21}$$

From here, if n is the number of junctions formed, the real area of contact must be equal to:

$$A_R = n\,\frac{\pi d^2}{4} \qquad \text{Equation 2.22}$$

Where d is the average diameter of each junction. It is then assumed that each junction will remain until a sliding distance equal to d before the junction interface breaks or a break within one of the materials occurs. This distance d is debatable but according to Rabinowicz, it is reasonable as a first approximation. It is also assumed that once the sliding distance d occurs and the junction breaks or a wear particle is formed that a new junction must be formed to support the load. As a result the number of junctions formed, N, for an arbitrary sliding distance, x, must be equal to:

$$N = \frac{nx}{d} \qquad \text{Equation 2.23}$$

Thus for a sliding distance, x = d, the number of junctions, N, formed is equal to the number of junctions broken, n. This is a rather simple approach but as will be seen, effective and consistent with experimental observation.

Rearranging Equation 2.22 we note the following:

$$n = \frac{4A_R}{\pi d^2} = \frac{4F_N}{H\pi d^2}$$ Equation 2.24

Thus, making the substitution:

$$N = \frac{4F_N x}{H\pi d^3}$$ Equation 2.25

Now it is assumed that a constant, K, is the probability (value 0 to 1) that breaking of a junction leads to a wear particle, either as a loose or transfer wear particle. If we assume that the wear particle formed is a hemisphere of diameter d (i.e. exactly half a sphere), then the volume of wear particles produced per sliding distance x, can be written as:

$$V_{adh} = \frac{KN\pi d^3}{12} = \frac{KF_N x}{3H}$$ Equation 2.26

Therefore, Archard's Law of adhesive wear is estimated above. K is the dimensionless probability between 0 and 1, F_N is the normal load, x is the sliding distance and H is the indentation hardness of the softer material. The value 3 is a shape factor based on the hemispherical approximation. Experimentation by the American Society of Lubrication engineers from 1958-1962 found the K value to be quite low. For example many materials exhibit a K value of about 30-50 x 10^{-4}. However a significant number of interactions take place over a short period of time to cause wear. This implies that this data strongly agrees with Rabinowicz that the most common case in adhesion is for the junction to shear with no wear particle (Rabinowicz 1995, 158-159). This K value is often termed the wear coefficient. If a substitution based on the coefficient of friction is made for F_N,

$$V_{adh} = \frac{KF_N x}{3H} = \frac{KF_F x}{3\mu_{adh} H}$$ Equation 2.27

At first glance this substitution seems to yield a counterintuitive result. It thus seems by raising the COF the volume of wear is decreased! However this is not the case from experimental experience. Rabinowicz found that a power law relationship was found for most metal on metal material interactions based on testing for relating the wear coefficient, K to the coefficient of friction, μ. Graphed on a log-log plot, the experimental findings found the following approximate relationship.

$$LogK \cong 4log\mu_{adh} + logb \qquad \text{Equation 2.28}$$

Here b is a positive number that is dependent on the material compatibility parameter C_m. Rewriting this equation in non-log form:

$$K \cong b{\mu_{adh}}^4 \qquad \text{Equation 2.29}$$

This experimental result is graphed below (Rabinowicz 1995, 167)

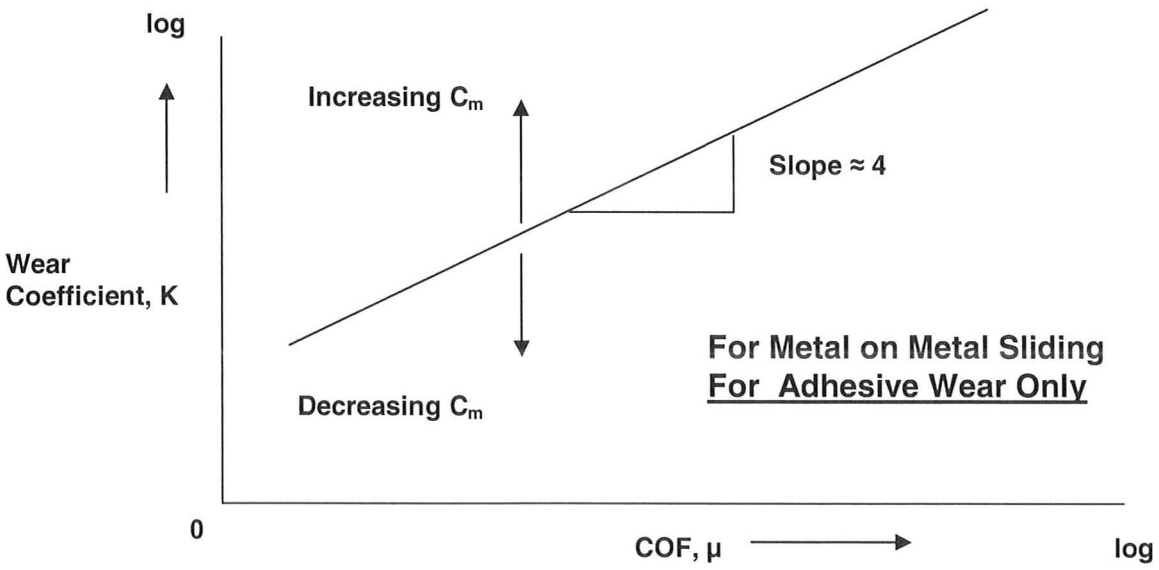

Figure 2.15: Relationship Between Wear Coefficient and COF for Metal on Metal Friction

Substituting this result into the modified Archard equation:

$$V_{adh} = \frac{KF_F x}{3\mu H} \cong \frac{b{\mu_{adh}}^3 F_F x}{3H} \cong \frac{b{\mu_{adh}}^4 F_N x}{3H} \qquad \text{Equation 2.30}$$

Here the friction coefficient is only the adhesive component of the total friction coefficient. While the exponent 4 is estimation it shows four important results, which are confirmed by Rabinowicz:

- The Archard adhesive wear equation is directly proportional to COF to the exponent 4 meaning a small reduction in COF has potential for large reduction in wear.
- An increase in hardness will lower wear which is consistent with the derivation of COF and experimental observation.
- The wear will increase directly with the sliding distance or time. This makes sense from ordinary experience. The more time parts are interacted under load the greater the chance the parts will wear out.
- The coefficient b is a function of the material compatibility parameter, C_m

2.2.3 Diffusive Wear

Diffusive wear derives from the elements of a particular material being transported to the other material due to a material concentration gradient as the driving force. For diffusion to occur there must be space for the atoms to move and sufficient energy to cause motion. The energy is vibrational in nature and is encouraged by an increase in temperature. According to Callister, temperature has one of the greatest effects on increasing diffusion (Callister 2003, 101). This is also supported by the work of Shaw (M. C. Shaw 2005, 177). This concentration driving force is increased exponentially by temperature.

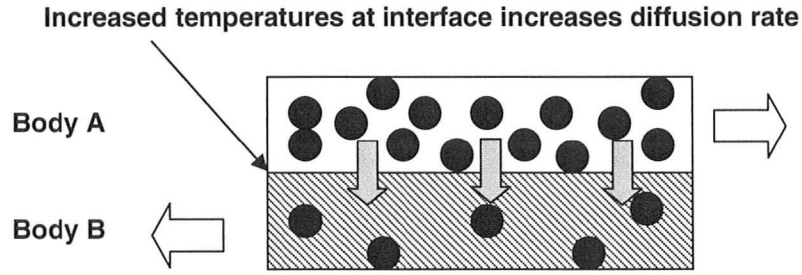

Figure 2.16: Illustration of Diffusive Wear Mechanism

Typically solid state diffusion can be modelled using Fick's Law to gain insight into the critical variables. Fick's Law states (Callister 2003, 96):

$$Mass\ Flux\ Species = -DA\frac{dC}{dx} \qquad \text{Equation 2.31}$$

Here D is the diffusivity which is dependent on the tendency of the elements to have potential to diffuse, A is the contact area of the surfaces and dC/dx is the concentration gradient of the atoms over a distance. The diffusivity is calculated by using Equation 2.32 (Callister 2003, 101):

$$D = D_o e^{\frac{-E_a}{RT}} \qquad \text{Equation 2.32}$$

Thus diffusivity has an Arrhenius type relationship with temperature. D_o is a pre-exponential constant, E_a is the activation energy, R is a constant and T is the temperature. As a result as temperature increases, the diffusivity and correspondingly the mass transfer of the species increases exponentially. Because friction is a dissipative process from plastic deformation taking place, high temperatures are reached at the interface. As a result, diffusion is increased tremendously as temperature increases (either from an increase in sliding speed or external source). The energy increase at the interface is given by Equation 2.33.

$$Energy\ Disspation\ Rate = F_F V = \mu F_n V \qquad \text{Equation 2.33}$$

The coefficient of friction here is the total friction coefficient. V here represents the velocity. It can be seen directly that the energy dissipation rate is directly proportional to COF. As a result, lowering COF will lower the temperature at the interface. Lowering the temperature will decrease the amount of diffusion and ultimately the amount of diffusive wear of the materials. Also a protective coating or lubricant can serve to reduce the temperature at the interface or act as a diffusion barrier. Surface chemistry and other atomic scale factors will play a strong role. A classic example of diffusion is the rubbing of diamond on cast iron. The carbon from the diamond will diffuse into the iron matrix causing diffusive wear of the diamond even though diamond is far harder than cast iron. Also in tungsten carbide tools the cobalt binder may diffuse out of the WC matrix if temperatures are high enough. In this case, the surfaces of the materials may appear to have a light-blue coloured residue.

2.2.4 Abrasive Wear

Abrasive wear derives from a harder surface ploughing or cutting into a softer surface. This ploughing may create a wear particle or the softer material may be simply displaced as a pile or mound of material, still intact to the original softer surface. This abrasive ploughing action is the principle behind the grinding process in metal removal operations. This hard asperity may be from one of the materials or as a 3rd body particle.

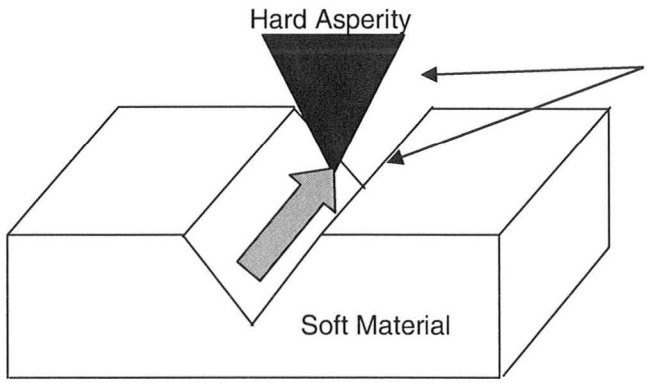

Figure 2.17: Illustration of Abrasive Wear

This build up of material is likely to be removed as a wear particle as sliding continues and the bond connecting it fails due to a fatigue related mechanism. Rabinowicz notes that if the harder surface is initially smooth then abrasive wear is far less likely to occur. Thus minimizing the R_a, R_q and R_z values of the harder surface will greatly minimize abrasive wear (Rabinowicz 1995, 191). Abrasive wear, from experience shows a similar equation to Archard's adhesive wear equation (Rabinowicz 1995, 193):

$$V_{wear} = \frac{K_{abr} F_N x}{H} \qquad \text{Equation 2.34}$$

Here K_{abr} is the abrasive wear coefficient. The other variables are the same as in the adhesive wear case. Thus it appears that high hardness also may reduce abrasion (however some hard inclusions in cases are known to produce the opposite effect). The work of Spurr and Newcomb found abrasion can be reduced by an increase in the elastic modulus, E (i.e. greater amount of elastic strain a surface can withstand) (Armarego and Brown 1969, 133). In a study completed by Avient, Goddard and Wilman in 1960 on the friction and wear of metals in abrasion, they found using various metals rubbed on emery cloth that the abrasive wear rate, W_{abr}, of metals follows the following relationship assuming that

abrasion is the dominant mechanism and that the total friction is approximately equal to the abrasive component of friction:

$$W_{abr} = KF_N(\mu_{abr} - C) \qquad \text{Equation 2.35}$$

Here K and C are constants. It thus shows that the wear rate in abrasion is directly proportional to the coefficient of friction (Avient, Goddard and Wilman 1960, 168).

2.2.5 Fatigue Wear

Fatigue wear is the result of the roughness component of friction. The mechanism considers that two asperities will interlock and produce a tensile and a compressive stress as shown in Figure 2.18. As the asperities slide over one another, this loading and unloading process occurs over and over. Cracks can develop beneath the surface and propagate, leading to a fatigue mechanism, with the asperities eventually breaking off as a wear particle (Armarego and Brown 1969, 135-136). The asperities may slide over each other several times and then break off forming a 3rd body particle. As a result, it appears that this type of wear should be proportional to the coefficient of friction.

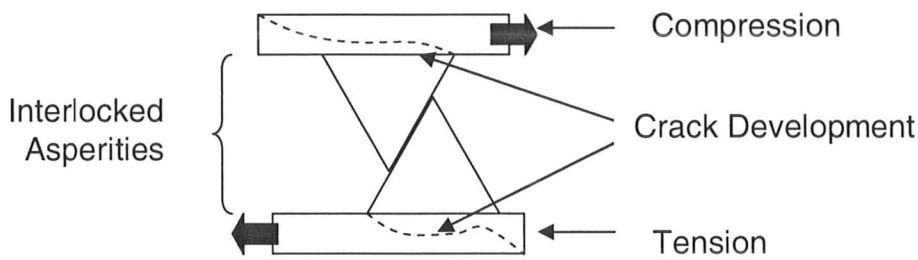

Figure 2.18: Illustration of the Fatigue Component of Wear

2.2.6 Chemical Wear

When two surfaces interact during friction chemical reactions may occur due to the combination of the materials and the potentially high temperatures which tend to increase the rate of a chemical reaction. A change in chemical composition or a transfer particle forming due to this interaction would be considered chemical wear. A common type of chemical wear is corrosion. This topic is inherently complex and will not be treated in detail, as the later part of this thesis will focus on the adhesive mechanism of wear.

2.3 Metal Cutting Principles

Before delving into friction and wear in a metal cutting application, it is imperative to outline the metal cutting process. The goal of this study is to use the concepts of tribology to reduce friction and wear in metal cutting applications. The three most common metal cutting operations are turning, drilling and milling.

2.3.1 Basics of Metal Cutting

Metal cutting is an important process in manufacturing. Metal cutting is highly interlinked with fields such as heat transfer, materials science, chemistry, lubrication, surface coatings and machine design. Thus machining on the whole is extremely difficult to model and a result it has been emphasized by numerous researchers that there is great value in well designed experiments to illustrate mechanisms that dominate the machining process. Such experimental setups are valuable to be able to accurately and reproducibly study the mechanisms in metal cutting in an effort to reduce waste, improve productivity, increase the number of uses for a single tool and produce a higher quality finished part.

Metal removal is significant and has a far reach in modern manufacturing. As a result the economics of metal removal is important. Significant research in the past 10-15 years has tried to estimate quantitatively the impact of metal removal processes. Outlined below are several reliable sources which highlight effectively the importance of improving metal removal manufacturing processes:

- Shaw estimates as of 2005 that in the United States, all forms of material removal accounts for 10% of the GNP (M. C. Shaw 2005, 2).
- Armarego found in a 1996 study that cutting tools in the United States are only selected correctly about 50% of the time and that tools are often only used to about 38% of their tool life capability (Armarego, et al. 1996).
- Trent stated that as of 1996, the United States purchased $7 billion in new machine tools. The total world consumption of machine tools in 1996 ranged from $35-40 billion. This was based on a study by the Association for Manufacture Technology (Trent and Wright, Metal Cutting 2000, 4).
- Ezugwu in 2005 in the International Journal of Machine Tools and Manufacture estimated that over $100 billion US is spent annually on metal cutting such as turning, milling, boring and other metal removal operations. The research also concluded that about 20% savings may be possible with the correct choice of tooling and machining parameters (Ezugwu 2005, 1353).

As a result there is a significant motivation to improve the metal cutting process. Shaw defines metal cutting to be a highly complex operation with two major operations taking place (M. C. Shaw 2005, xi) :

- Large strain and strain rates within the metal being cut (i.e. workpiece).
- Heavy loading and high temperatures between the chip and tool.

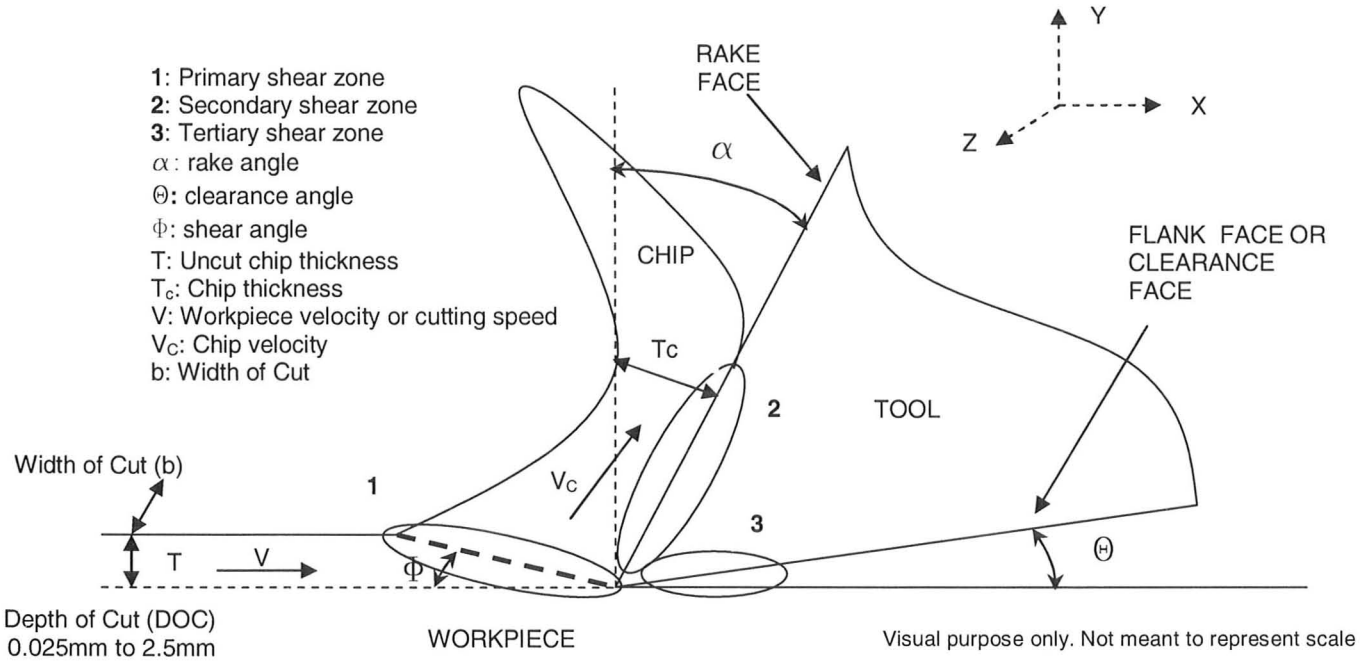

Figure 2.19: Tool and Workpiece Interaction Diagram

As a result of this tool and workpiece interaction, 4 important observations may be generally made for metal cutting (M. C. Shaw 2005, 4):

- Metal tends to shear rather than fracture during the cutting process.
- Chip formation is a highly plastic process that varies with the process and may be continuous or in smaller broken segments.
- The temperatures at the interface of the tool and workpiece are extremely high.
- The tool is constructed fundamentally of a harder material than the workpiece in order for the metal cutting mechanism to effectively take place.

The illustration in Figure 2.20 was adapted from the text *Manufacturing Science* by Amitabha Ghosh and Asok Kumar Mallik (Mallik and Ghosh 1986, 190) and is an elegant diagram that illustrates the wide application of Figure 2.19 to all major metal cutting operations. It thus stands to reason that if a solution can be found that agrees with this fundamental interaction and improves friction and wear it has potential to improve several metal cutting applications.

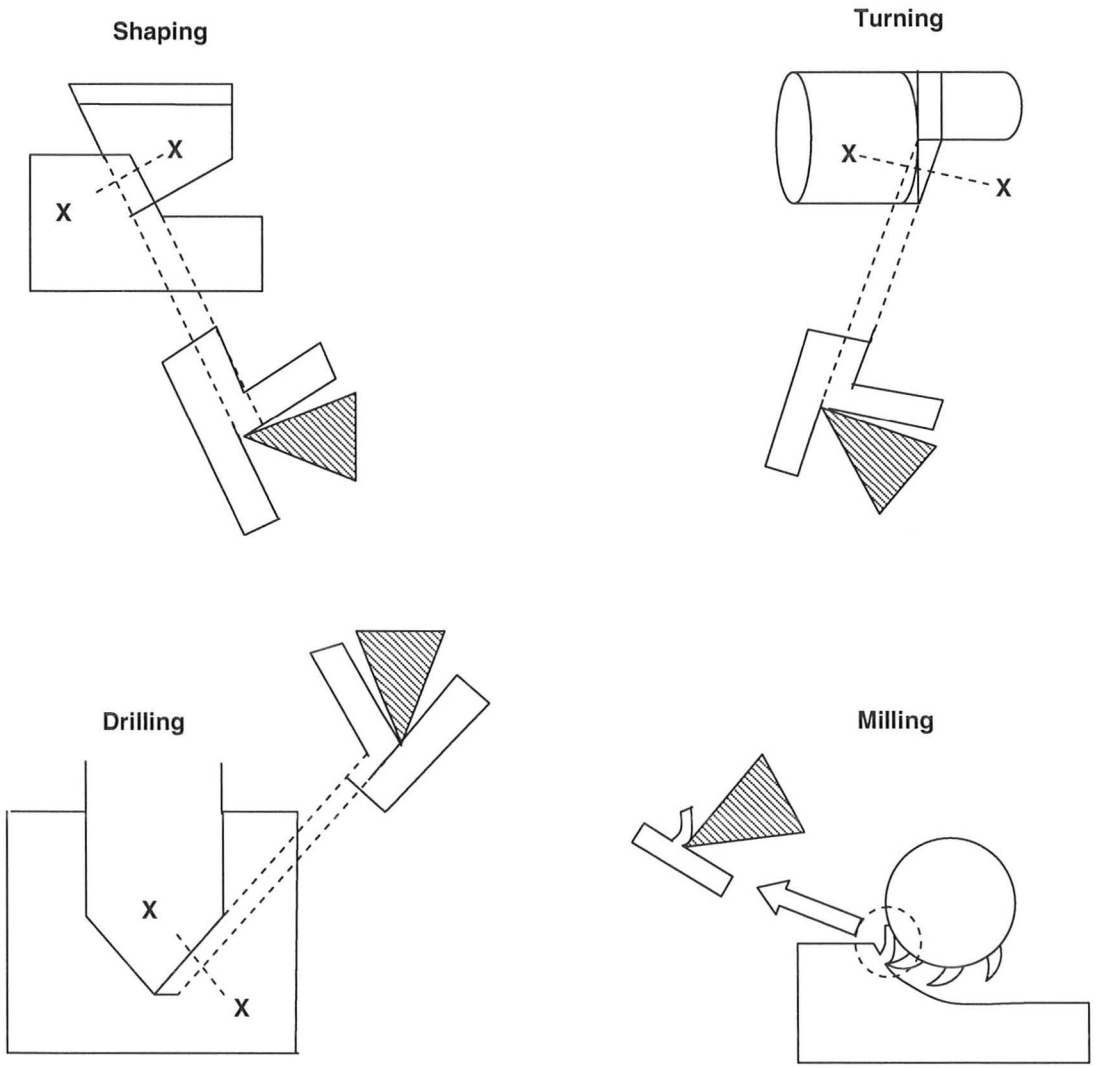

Figure 2.20: Tool and Workpiece Similarity for Various Metal Cutting Removal Processes

While this diagram represents orthogonal cutting it suffices to explain the physics taking place during metal cutting. Typical machining operations are

oblique. Regardless of orthogonal or oblique cutting, the basic principles of this chip diagram still hold true. Taking a closer look at the chip-tool interaction, more detailed information can be found about the cutting process. This model is simplified and contains numerous assumptions; however it is a reasonable first approximation. Some of the assumptions from this diagram are not completely accurate (M. C. Shaw 2005, 17). The assumptions are listed below:

- Assumption of homogenous strain.
- The chip does not flow to the sides.
- Constant depth of cut or uncut chip thickness.
- Workpiece width is greater than that of the width of cut (b).
- Uniform velocities.
- Continuous chips with no built up edge.
- Uniform normal and shear stress profiles.

In these processes the operator typically has control over the following variables:

- Cutting speed (V).
- Uncut chip thickness (d) which is often referred to as depth of cut (DOC).
- Feed rate (f) of the cutting tool over the workpiece.

In general the metal removal rate (MRR) is desired to be high. This increases efficiency and profitability.

$$MRR = Vfd \qquad \text{Equation 2.36}$$

Typically the depth of cut varies from 1mm for a heavy roughing operation to 0.1mm for a very fine finishing operation. The upper end is typically a machine or tool load limitation while the lower end is set by workpiece accuracy requirements. The cutting speed is usually limited by the thermal and strain sensitivity of the tool

or workpiece and feed rate is generally set by machine limitations on the high end and surface finish requirements on the fine end. Often production costs for metal cutting can be represented as a function of one of the processing parameters.
An example is cutting speed plotted vs. production cost. In this case cost reduces until a point where tool wear and thus tool life issues start to dominate and cost related to tooling start to increase overall production costs.

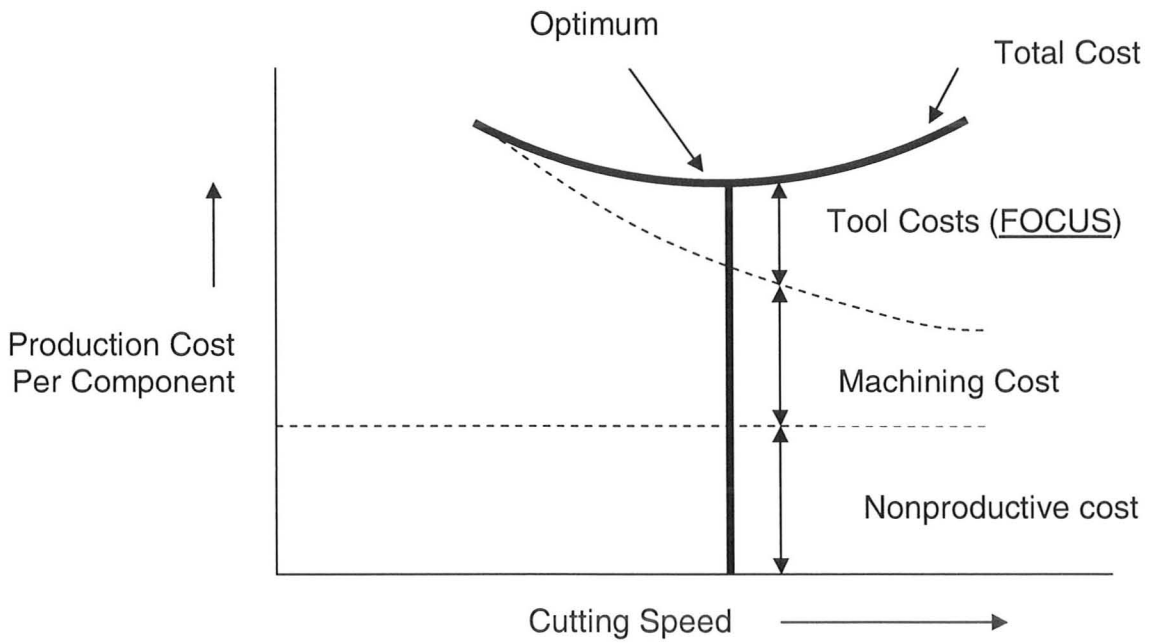

Figure 2.21: Analysis of Metal Cutting Costs vs. Cutting Speed

Here the total cost per part is the sum of the non-productive cost (i.e. raw material), machining cost (i.e. machine cost, labour) and the tool costs (i.e. purchase price plus the labour associated with replacing the tool). The focus of our research is to make the tool costs lower at higher cutting speeds which would work to shift the optimum cost per part further to the right which would increase productivity (Boothroyd 1975, 149) without triggering an increase in friction and wear. In metal cutting the two most dominant tool materials used are high speed

steel and tungsten carbides (cemented carbides) (M. C. Shaw 2005, 310-315). Tools must be made of extremely hard materials and they must also possess high strength and fracture toughness at elevated temperatures. The focus of this thesis will be on tungsten carbide tools with a 6% cobalt binder which is very common in cutting tool inserts. The workpiece materials of focus will be the hard to cut nickel alloy Inconel 718 and Titanium alloy Ti6Al4V.

2.3.2 Cutting Forces and Coefficient of Friction – Rake Face

In general metal cutting forms two new surfaces. The first is the underlying part of the chip and the second is the new surface of the workpiece (Trent and Wright, Metal Cutting 2000, 22). In general the underside of the chip is a freshly generated surface which is chemically active and due to metal on metal contact, it is "welded" to the tool face very efficiently (Trent and Wright, Metal Cutting 2000, 323). Despite the tool face often having a lubricant and special coatings, an intense adhesive interaction occurs between the chip and the rake face of the tool.

Trent states: "The contact area on the tool rake in particular is seen to be a very important region, controlling the mechanics of cutting and becomes a point of focus for research on machining. Not only the forces, but the temperatures, tool wear rates and the machininability of work materials are closely related with what happens in this region..." (Trent and Wright, Metal Cutting 2000, 74). Thus the rake face can have harsher wear than the flank face. Looking at the secondary shear zone on the rake face in more detail, the following forces of interest exist.

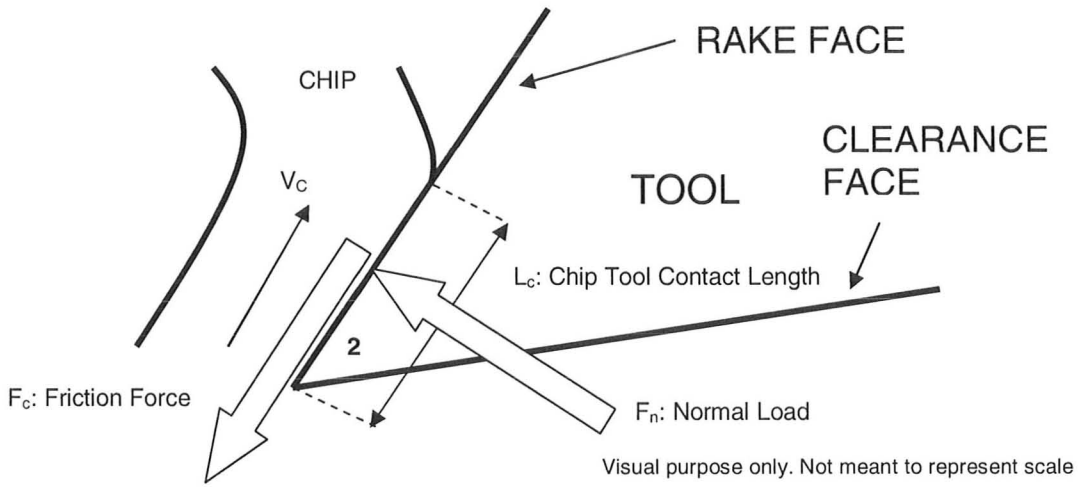

Figure 2.22: Forces Present on the Rake Face of a Typical Metal Cutting Tool

Shaw also notes that the friction on the clearance face is often less aggressive than on the rake face. As a result, larger benefits will come from improving friction conditions on the rake face than the clearance face. However it stands to reason that if the friction on the rake face is improved, there is a strong chance that there will be a friction improvement on the flank or clearance face. In 1945 Merchant proposed the following detailed force model which is widely used today. If these forces are decomposed into vectors, the following circle diagram in Figure 2.23 and Figure 2.24 can be constructed as adapted from Shaw's work (M. C. Shaw 2005, 18).

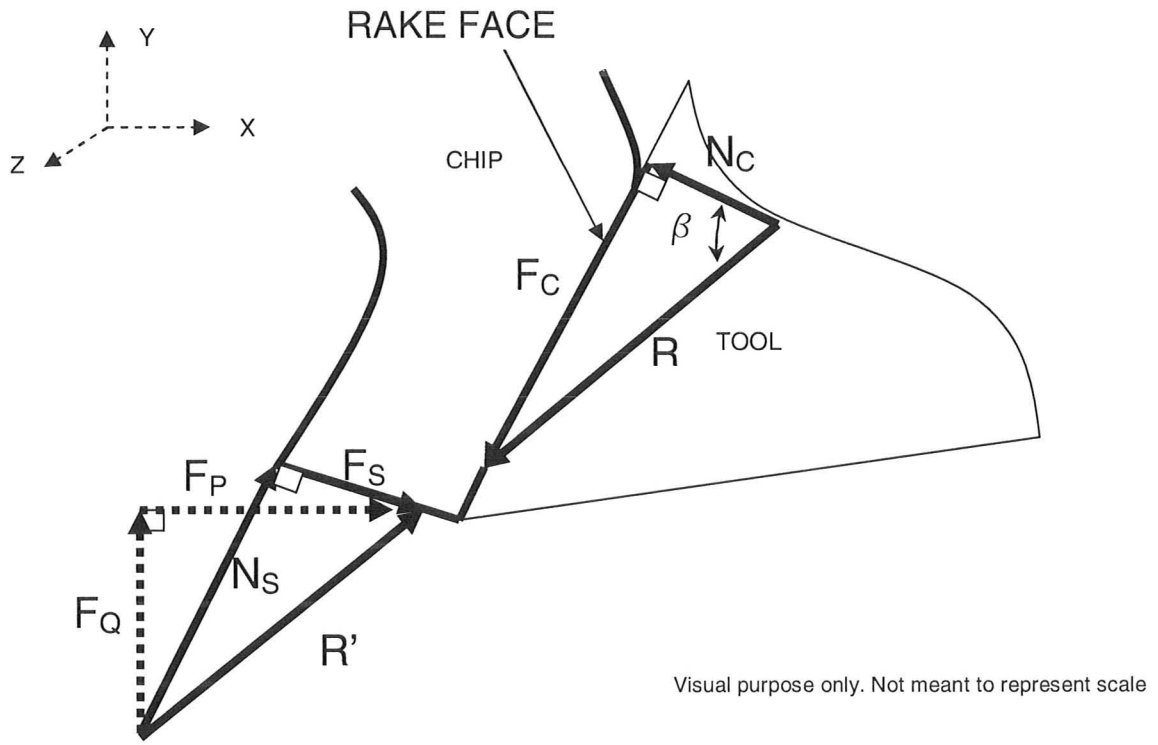

Figure 2.23: Forces Present in Metal Cutting on the Rake Face

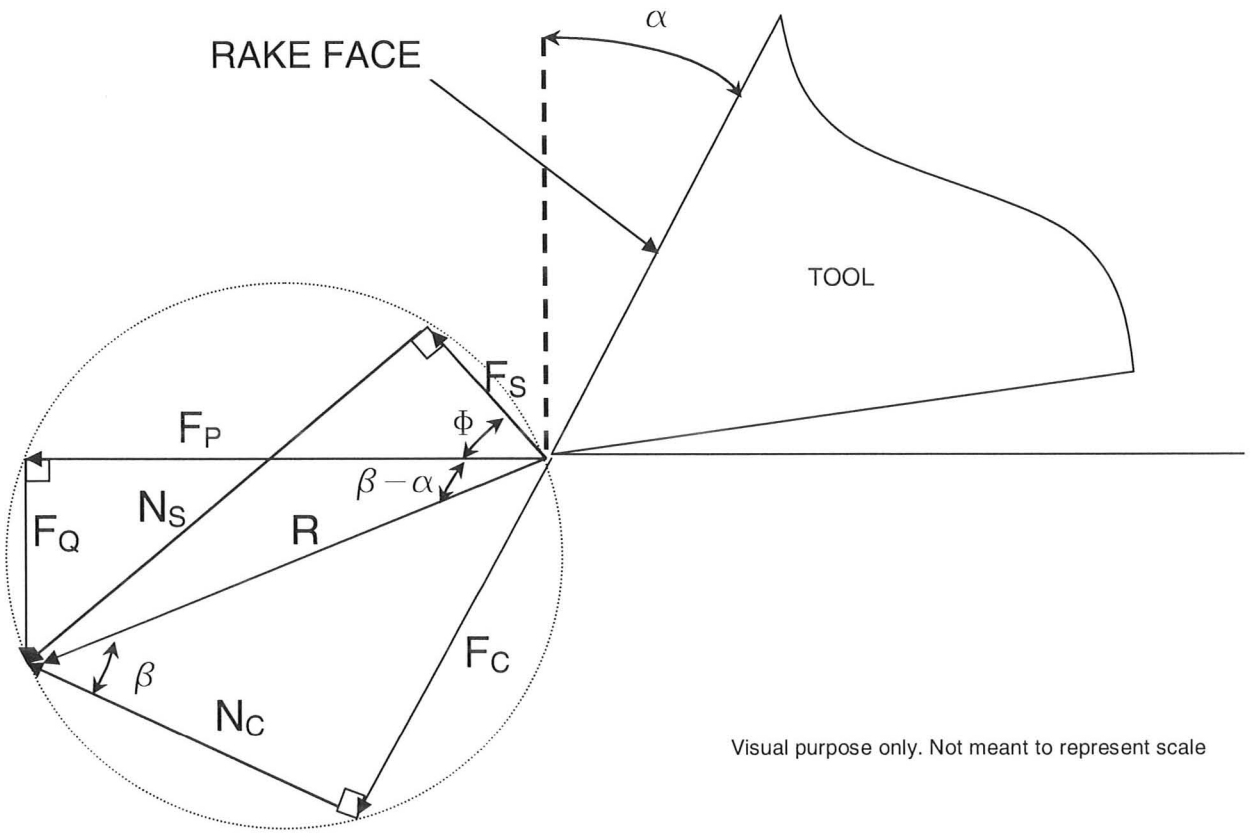

Figure 2.24: Merchant's Circle Diagram for Cutting Forces

F_S and N_S are the forces generated by the cutting action and sum to R'. Here F_Q and F_P are represented by dotted vector lines. This is to indicate that these are the forces measured easily by a dynamometer on the cutting tool. The following velocity vector diagram can also be constructed if a free body diagram (FBD) is isolated around the chip.

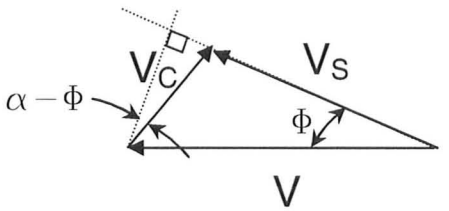

Figure 2.25: Cutting Velocity Vectors

Here the sum of the cutting velocity or speed (V) and the chip velocity (V_C) is equal to the shear velocity (V_S). V_C is the main variable of interest as it pertains to the speed of the bulk of the chip flowing across the rake face. Thus it becomes evident that many components and specific angles in cutting affect the frictional behaviour on the rake face. Based on work by M.C Shaw, cutting forces are typically in the range outlined in Table 2.5.

Table 2.5: Typical Forces Found In Orthogonal Cutting Operations

Force	Typical Range of Values (N)
F_P	500-3000
F_Q	250-1500

In general for orthogonal cutting F_Q will be less than F_P, with F_Q being equal to approximately 50% of F_P. From Merchant's circle and the diagrams introduced thus far the following relationships may be formed (M. C. Shaw 2005, 18):

Table 2.6: Force Equations In Orthogonal Cutting

Force	Equation
Shearing Force (F_S)	$F_S = F_P cos\Phi - F_Q sin\Phi$
Normal Shear Plane Force (N_S)	$N_S = F_Q cos\Phi + F_P sin\Phi$
Friction Force (F_C)	$F_C = F_P sin\alpha + F_Q cos\alpha$
Normal Force (N_C)	$N_C = F_P cos\alpha - F_Q cos\alpha$

As a result the coefficient of friction is commonly determined by the following equation:

$$\mu = tan\beta = \frac{F_C}{N_C} = \frac{F_P sin\alpha + F_Q cos\alpha}{F_P cos\alpha - F_Q cos\alpha} = \frac{\tau}{\sigma} \qquad \text{Equation 2.37}$$

Here τ and σ represent the frictional shear stress and the normal stress respectively on the rake face or secondary shear plane. Shaw has reported COF as high as 0.5-1.5 (M. C. Shaw 2005, 29-30). This coefficient of friction is a lumped or bulk average. As will be shown, this definition of coefficient of friction is often inadequate in determining frictional effects in metal cutting and has faced criticism as this value does not represent a range (min and max) or standard deviation in values. Furthermore, two types of frictional regimes exist on the rake face The rake face will be discussed in more detail to outline the shortcomings of this simple COF model in an effort to determine a more appropriate analysis.

2.3.3 Stress – Rake Face

The work of Zorev (Zorev 1966) has shown that the normal and shear stresses on the rake face of a cutting tool varies with position along the tool-chip contact length. Furthermore, the tool-chip interaction phenomena vary within the tool-chip contact length (L_c). There is a seizure region near the tip of the tool and a sliding zone that trails further from the cutting edge. It is difficult to estimate the exact proportion of the contact length, that experiences seizure and sliding but as an estimate, 50% of L_c for both regions is a reasonable assumption (Stephenson 1997, 424-425). The path to seizure on the rake face can be summed up in 3 stages. First plastic deformation leads to breaking of surface films and oxides.

During the second stage, the asperities contact and nucleate. The plastic deformation continues and intensifies at this point, which is encouraged by material creep. During the 3rd stage the asperities are interlocked and form a strong bond and are effectively seized. Points of contact are continuously developing as well as being destroyed (Fox-Rabinovich and Totten 2007, 71-72). The profile of stresses takes the following approximate form shown Figure 2.26 (Trent 1983, 81).

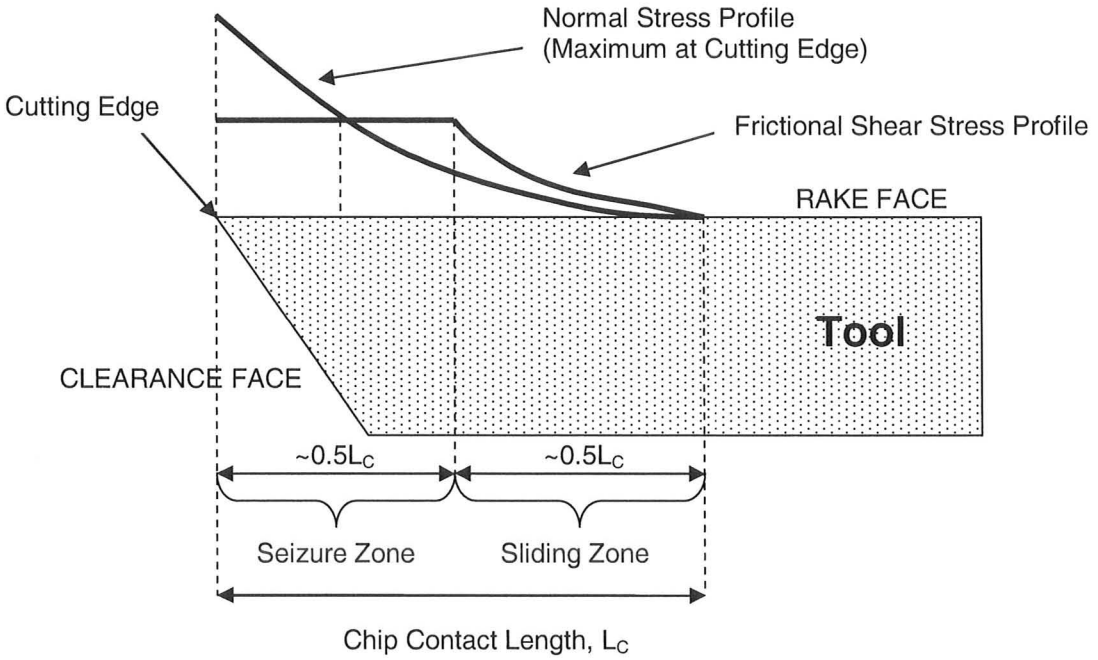

Figure 2.26: Stress Profiles on the Rake Face of Tool

Trent has cited 2 examples of cutting 1020 and 12L14 steel and found that in both cases the shear stress was about 15-50% of the normal compressive stress in the seizure zone. The frictional shear stress is highest in the seizure zone and decays in the sliding zone. In the sliding zone the shear stress is approximately equal to the normal stress (Trent 1983, 89). Further results from Chandrasekaran and Kapoor found similar results, with the shear stress being in

the range of about 20-40% of the normal compressive stress in the seizure zone. Thus COF in this region should range from about 0.15 to 0.50 which is the same range derived earlier for an adhesive mechanism. This study noted that the shear stress is in the range of the shear stress of the workpiece material (Chandrasekaran and Kapoor 1965, 498, 500). Trent notes that the mean compressive stress from cutting materials like medium carbon steel and titanium can reach in the range of 0.5 to 1 GPa in the seizure zone (Trent and Wright, Metal Cutting 2000, 80). Loladze, using a split tool found that when cutting several steels, the maximum stress near the tool edge varied from 0.9 GPa to 1.6 GPa (Trent and Wright, Metal Cutting 2000, 82). Boothroyd has reported compressive stresses as high as 3.5 GPa (Boothroyd 1975, 85). Thus in general 0.5-3.5 GPa is a typical compressive stress range on the rake face of the tool in the seizure zone. Figure 2.27 from Shaw illustrates how two different regimes of friction exist simultaneously on the rake face of the tool. The sliding zone is region 1 (LLS) and the seizure zone may be region 2 or 3 (HLS). This graph does not show the effect of temperature.

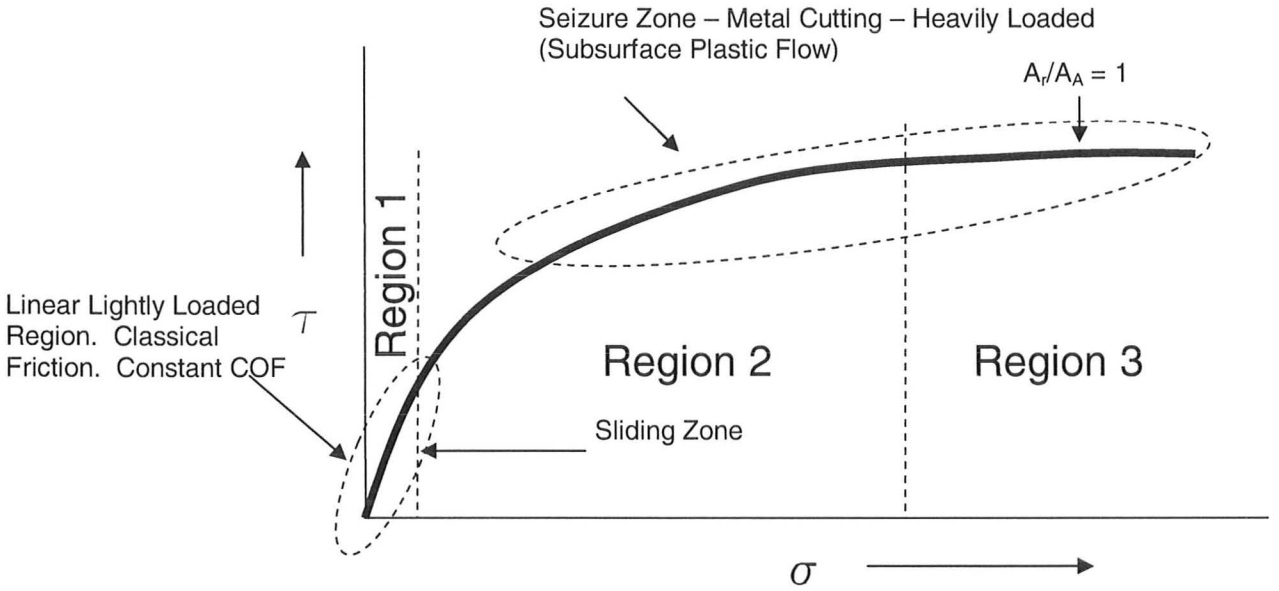

Figure 2.27: Stress Regimes on the Rake Face of the Tool for the Seizure and Sliding Zones

As load is applied yielding occurs at the tips of the asperities and the real area grows until it can sufficiently support the load. After sufficient load is applied and junction growth occurs, plastic flow moves from within the asperities and into bulk subsurface plastic flow. The work of Bailey also supports this theory of subsurface plastic flow in metal cutting (Bailey 1975, 243). Under these conditions the real area of contact approaches the apparent area (high adhesion ensues and surface roughness plays a diminished role) of contact at which point the normal load has no significant effect. According to Trent, the velocity of the chip at the interface of the seizure zone is thought to approach zero (Trent and Wright, Metal Cutting 2000, 65). Even though the bulk chip velocity V_c is not zero, the thin seized layer of chip to the tool is thought to be barely moving and this is supported by quick stop tests where the chip is completely stuck to the tool. Bailey also found this trend to be true and expressed accurately by Figure 2.28 (Bailey 1975, 265).

Shaw has illustrated this phenomenon as well and shows the following velocity gradient within the chip, with subsurface plastic flow occurring at the interface (M. C. Shaw 2005, 177).

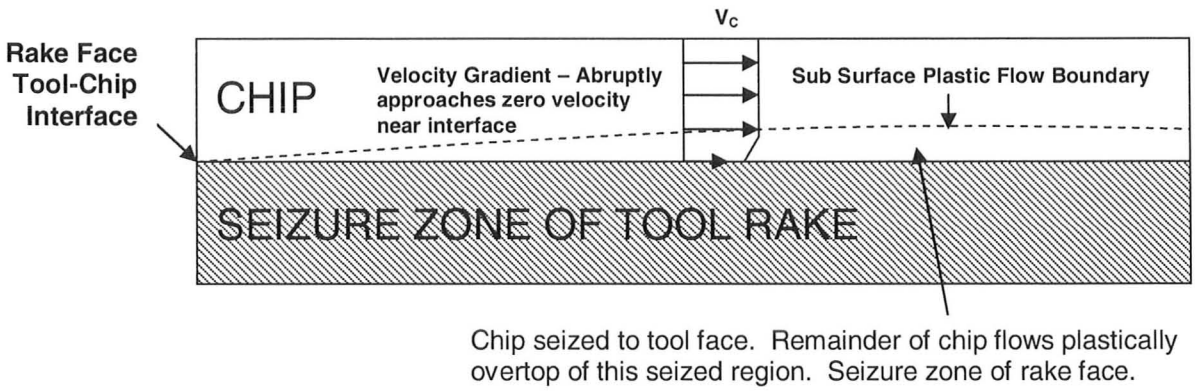

Figure 2.28: Velocity Gradient of the Chip in the Seizure Region

Shaw notes that the combination of high stress, high temperature and low surface velocity is unique to the subsurface plastic formation that forms in metal cutting on the rake face seizure zone. As a result, simulation or knowledge of the seizure region is valuable. Minimizing friction in this seizure region would most likely have the most significant benefits than simulating and improving the sliding region or the flank face. Thus the COF value calculated from Merchant's circle diagram is a lumped value that does not encapsulate the entire friction phenomena. The friction and wear in the seizure region and sliding region are completely different. Thus with the seizure region being more critical to friction and wear, simulating close to seizure conditions with rake face stresses and temperatures would yield a COF value with farther reaching implications and meaning for improving metal cutting processes.

2.3.4 Temperature – Rake Face

Machining as mentioned is characterized by its high temperatures. In some cases the tool may look relatively cool however the contact points may be around 1000°C. This is frequently observed with chips glowing red hot. In general the temperature gradients in machining are quite steep, ranging several hundred degrees Celsius over a few millimetres (M. C. Shaw 2005, 214). Bowden and Tabor also noted that these high temperatures are reached often extremely quickly in many cases in a matter of seconds (Bowden and Tabor 1950, 41). Recent results published in CIRP showed that high temperatures in metal cutting can reach steady state in less than 20 seconds (Davies, et al. 2007, 588) . Thus the assumption of a quasi steady state temperature profile is quite valid as a framework to establish the criteria for machining (M. C. Shaw 2005, 240). These temperatures will have a direct effect on COF and wear. There are 4 major areas of energy consumption: 1) shear plane, 2) friction at the tool-chip interface, 3) formation of new surface areas and 4) momentum change. Of these 4 mechanisms of energy consumption the first 2 consume the bulk of the energy, with the shear plane consuming about 75% of the energy and the friction at the tool chip-interface consuming approximately 25% of this energy (M. C. Shaw 2005, 31). Thus in general the primary shear zone is the largest contributor to heat generation (Boothroyd 1975, 93). Of this energy consumed most of the heat is expelled as thermal energy which results in an appreciable temperature rise (M. C. Shaw 2005, 26). According to Shaw, 90% of the total energy generated goes to the chip, 5% energy to the tool and 5% to work (M. C. Shaw 2005, 25). Thus, the

net heat flux is to the chip. Thus in simulation of cutting, it becomes important to capture this heat flux. As plastic deformation occurs on the primary shear plane during cutting, the gross plastic deformation causes considerable heat to be generated. The portion of the chip that slides against the rake face of the tool then accumulates more heat and as a result the highest temperatures are on the rake face of the tool a short distance away from the cutting edge. Thus the chip is hottest on the rake side and cooler on the opposite side. As a result it is not uncommon for temperatures at the chip to tool interface region to range anywhere from 600°C to 1300°C depending on the application (Boothroyd 1975, 110). The temperatures found in metal cutting are often a function of the cutting speed, the feed rate, the uncut chip thickness (depth of cut), the width of cut and the materials. However it is well known from research that the cutting speed and material properties tend to have the largest effect on temperatures. Once the material is selected (often this is a chosen or fixed variable in many processes), the cutting speed is typically has the largest effect on the temperatures reached. Cutting speeds reported by Trent are often in the range 0.05m/s to 5 m/s (Trent and Wright, Metal Cutting 2000, 11). Typical feed rates are 0.0125mm/rev to 2.5 mm/rev (Trent and Wright, Metal Cutting 2000, 11). In general reducing the chip contact length will reduce temperatures. Experiments have shown that up to about 30% lower temperatures can conceivably be achieved by lowering the contact length (Trent and Wright, Metal Cutting 2000, 128). The temperature profile in machining is affected by the tool geometry, the rake angle and the clearance angle (Trent and Wright, Metal Cutting 2000, 128). Some heat will come from the tertiary

shear zone (clearance or flank face) but it is usually less than the other two zones unless this area is badly worn. In many cases the chips are discoloured to a blue or purple colour which can be related to temperature. Hardness tests of the chips post cutting also indicate that high temperatures are reached and then rapidly cooled (Trent and Wright, Metal Cutting 2000, 100). Shown in Figure 2.29 is an illustration of the temperature profiles in metal cutting.

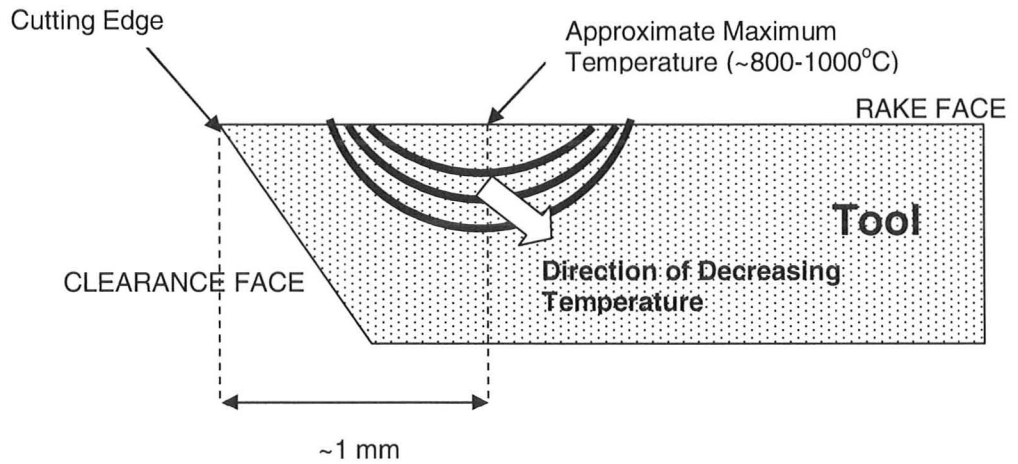

Figure 2.29: Temperature Profiles in Metal Cutting

The 1mm value is an estimate and does not represent all cutting scenarios. The average tool rake face temperature can be approximated by:

$$T = u\sqrt{\frac{Vt}{k\rho C_p}} \qquad \text{Equation 2.38}$$

Here u is the specific cutting energy (function of the material), V is the cutting speed, t is the uncut chip thickness or depth of cut, k is the thermal conductivity, C_p the specific heat capacity and ρ the density of the workpiece material. Width of cut is of no major significance to tool temperature and is omitted from this analysis. This equation shows that cutting speed appears to have the

same impact as the depth of cut. In general the specific cutting energy varies with $1/t^{0.2}$ thus substitution for u in terms of t yields Equation 2.39 (M. C. Shaw 2005, 238). Thus cutting speed tends to have the greatest influence on tool rake face temperature.

$$T \propto V^{0.5} t^{0.3}$$ Equation 2.39

Similar results were found by Kalpakjian (Kalpakjian 1995, 612) who stated that in general cutting speed was the most dominant of the cutting parameters. For a general set of conditions, hard to cut materials like titanium have a specific energy of 35.1 x 10^8 J/m^3 and high temperature strength nickel based alloys like Inconel 718 have a specific energy around 49.14 x 10^8 J/m^3. Aluminum has a specific cutting energy on the order of 5 times less than that of titanium (M. C. Shaw 2005, 35). As the specific energy is relatively independent of the cutting speed and only moderately affected by the rake angle, it is a useful term to help dictate which materials will machine well and which won't.

The rake angle, shear angle and type of chip will also govern the temperature and friction and often the underlying relationship is best established using experimentation. In general Shaw notes that there is no single simple method to measure temperature at the tool chip interface. Whether it is hardness calibrations of the chip or tool, thermocouples, pyrometers, chip colours, temperature sensitive paints or even FEA, there are assumptions and errors in temperature. At best these temperature measurements are estimations if done very carefully. Shaw notes that many of the temperature gradients are exponential. Temperature on the flank face tends to be lower than the rake face and not as sensitive to the cutting parameters as is observed with the rake face.

In general the bulk COF in machining will vary with temperature as shown in Figure 2.30. This is due to thermal softening at the higher temperatures and possibly voids generated by thermal cracking (Bailey 1975, 266). Work from Merchant has shown a similar trend to Bailey's, based off the work of Zorev (Zorev 1966, 222). The work postulates that COF initially rises with increased adhesion (as temperature increases), dominating the reduction in shear strength, reaches a peak value and then decreases with increased temperature (American Society for Metals 1950, 30) as shear strength reduction begins to dominate over adhesion effects.

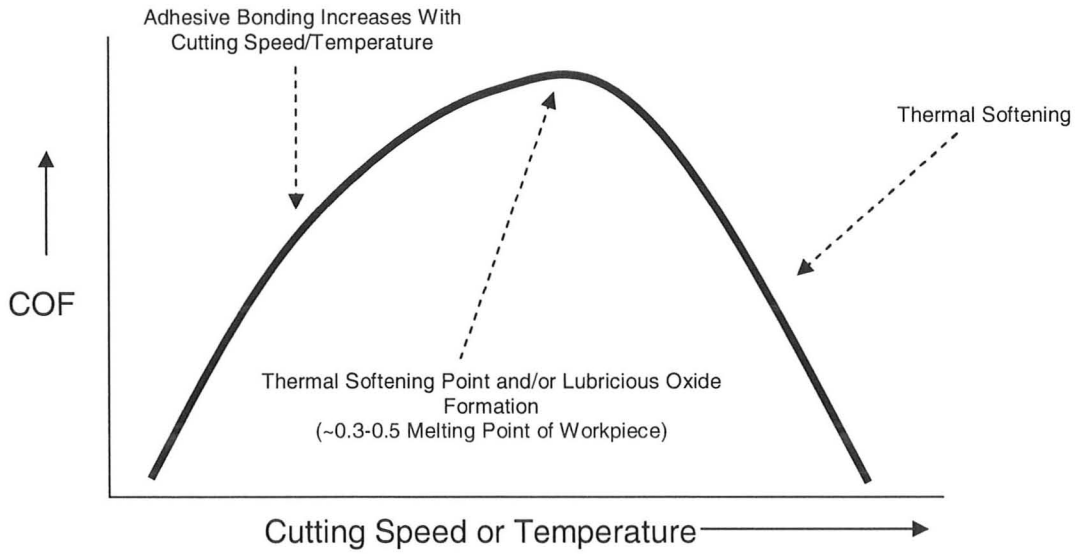

Figure 2.30: Variation of Bulk COF with Cutting Speed or Temperature

Schey has also noted the trend in Figure 2.30 (Schey 1983, 581). The work of Iwata et al. has also confirmed that around 0.3-0.5 of the melting point of the softer material, is approximately the peak of the COF curve (Iawata, Aihara and Kurasaka 1971, 153-163). It is worth noting that with a reduction in cutting forces at higher cutting speeds (i.e. higher temperatures) this does not mean that tool life

will be improved. The thermal effects may be such that diffusion or decrease in tool strength becomes critical. In general tool life is inversely proportional to temperature.

2.3.5 Wear In Metal Cutting

In general materials are considered more machinable if the tools being used to machine them last longer, if the cutting forces are lower, if the surface finish of the workpiece is improved and overall they allow for higher MRR rates (Trent and Wright, Metal Cutting 2000, 252). Due to the intense stresses, temperatures, friction and seizure in metal cutting tools, the tool inserts tend to wear out rapidly. Any improvement in wear resistance may have a dramatic improvement in process stability which impacts part quality and productivity. In general, metal cutting has several wear mechanisms operating simultaneously, which account for the inherent complexity associated with wear. Often these wear mechanisms are interrelated and no direct solution to all of them may be immediately available. Wear as previously mentioned is a relative term. Wear as criteria may pertain to any or a combination of the following:

- # of parts produced before a certain unacceptable surface finish on the workpiece is produced.
- # of parts produced before catastrophic failure of the tool.
- Volume of material removed from the tool or length of wear scar.

The following sketches in Figure 2.31 were adapted from Fox-Rabinovich and Totten (G. a. Fox-Rabinovich 2007, 152). For carbide tools on the rake face, adhesion and diffusion tend to be the dominant wear mechanisms. Diffusion

produces a crater and adhesion produces a built up edge which may eventually be pulled from the tool, taking tool material with it.

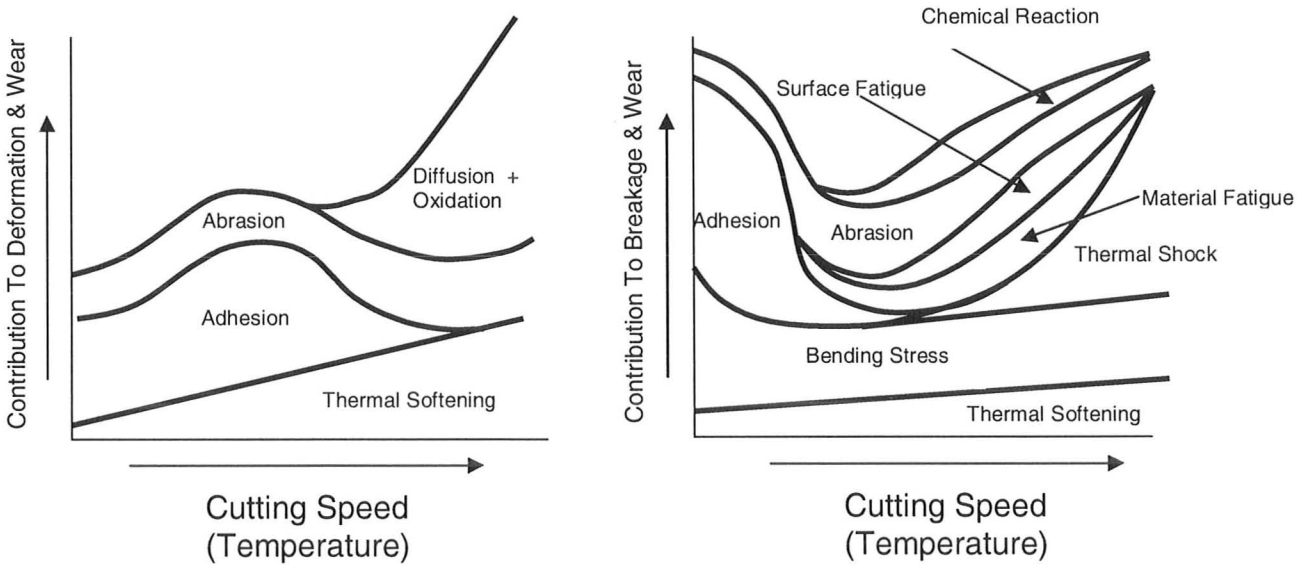

Figure 2.31: Wear Mechanisms in Metal Cutting That Operate Simultaneously

Childs presents a similar argument based on the MRR (Childs, et al. 2000, 121). Childs representation notes that under machining conditions that adhesion tends to be more dominant than abrasion and fatigue. These graphs are all generalized and a case by case basis is required. Schey notes that in general the wear trends on the flank face are directly proportional to the rake face, although the rake face wear rate tends to be more aggressive. Meaning, if the wear is reduced on the flank face there is potential the wear will be reduced on the rake face and vice versa (Schey 1983, 599). Similarly Boothroyd has noted that while the friction on the flank face may be similar, the rake face seizure sticking is harsher and more dominant (Bailey 1975, 256). This forms a key central point for this work. Later in this thesis flank wear will be compared to the bench scale COF data of the tribometer which simulates rake face conditions. The research

completed to date has validated the conclusion of Schey, that in general the wear rates of the rake and flank face directly scale together. Shaw explains the classic wear rate curve as follows (σ_S stands for the yield strength of the workpiece material):

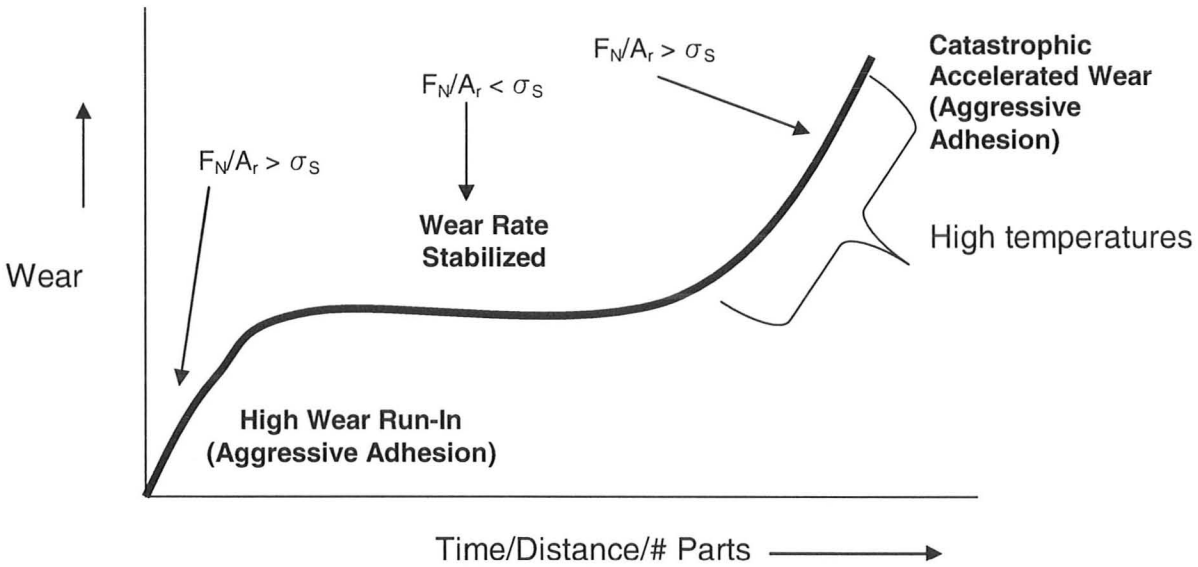

Figure 2.32: Fundamental Wear Curve Frequently Observed In Metal Cutting

For this analysis, Shaw assumes that the yield stress of the workpiece is approximately the threshold for subsurface plastic flow. Shaw also finds that wear is greater in a subsurface plastic flow regime (heavily loaded slider) than a lightly loaded slider case. During the initial run in stage, the real area of contact is initially very close to 0 as the load grows. As a result the stress is very high. Thus F_N/A_r will exceed the yield strength and high wear will occur. The high level of wear is indeed observed in the run in stage of many metal cutting tests as can be observed under an SEM microscope (Dr.G.Fox-Rabinovich 2010). This is the reason why intermittent cutting is detrimental as it experiences this harsh run-in stage more frequently. As the real contact area then grows under load, eventually

the F_N/A_r ratio will go below the yield strength of the workpiece. The condition for subsurface plastic flow will not be met and less adhesive interaction and/or wear will occur. The wear will more or less stabilize or grow at a slow rate. Eventually the temperature in the interface will rise, increasing adhesion and decreasing the yield strength of the materials temperature. As a result, the F_N/A_r ratio reverts to the case where it is greater than the elevated temperature yield strength and subsurface plastic flow initiates again and excessive wear occurs typically until failure (M. C. Shaw 2005, 172-173). Armarego and Brown found that the form of Archard's wear equation applies to machining. They also found that the wear will increase with temperature (Armarego and Brown 1969, 138-139). This is also supported by Shallbrock in 1938 (M. C. Shaw 2005, 283) and Boothroyd (Boothroyd 1975, 146). Flank Wear is typically the standard for tool wear. It is often measured as the length of the wear scar or notch wear scar on the flank face. When this length reaches 300 microns the tool is typically deemed to be worn out and no longer usable. These criteria may change depending on the application. A typical flank wear curve is shown on the following page.

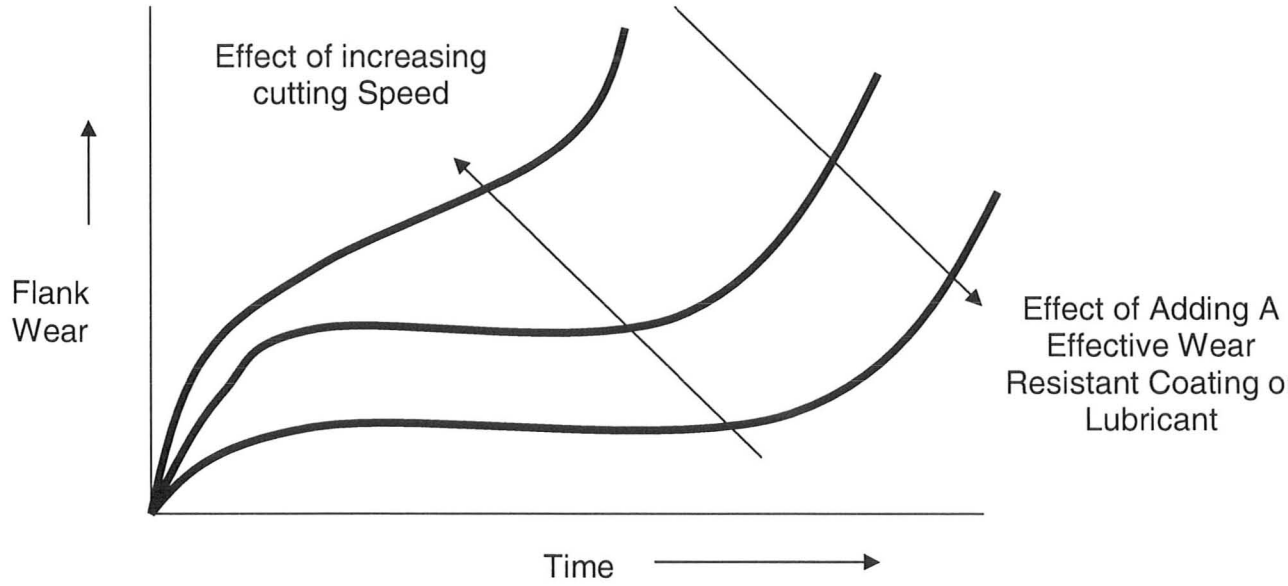

Figure 2.33: Effect of Cutting Speed, Coatings and Material Removal on Flank Wear

The wear rate on the rake face is higher than that on the flank face. However, the volume of wear required for failure is larger on the rake face than the flank face for catastrophic failure. Shaw denotes that the tool life is approximately the same regardless of whether rake face or flank face wear is used. Because the rake face scar is harder to measure (depth of wear) it is thus more subjective and is less widely measured compared to flank wear which is a linear distance easily measured under a microscope. However, crater wear depth curves on the rake face follow the same general wear trend as flank wear curves (M. C. Shaw 2005, 180-181). Schey also notes this trend (Schey 1983, 599). Taylor notes tool life by Equation 2.40:

$$VT^n = C \qquad \text{Equation 2.40}$$

Here V is the cutting speed, T is the tool life and C and n are constants based on the tool-workpiece combination. For HSS, n = 0.1, for WC, n = 0.4. Thus, this classic equation also reinforces that cutting speed/temperature tends to

be more or less the most dominant variable in wear. This equation may be re-written in a form which is more helpful in analyzing the largest effects on tool wear (M. C. Shaw 2005, 180):

$$VT^{1/n}f^{1/m}b^{1/l} = C' \qquad \text{Equation 2.41}$$

Here n < m < l. Here f is the feed rate and b is the depth of cut. This shows that tool life is most affected by cutting speed, then the feed rate and lastly the depth of cut. Of particular interest in metal cutting is the formation of built up edge (BUE) which occurs when the workpiece material adheres to the seizure zone of the rake face. The BUE is typically formed in the first few seconds of cutting or running in. The BUE tends to be near the cutting edge of the tool (Trent and Wright, Metal Cutting 2000, 102). BUE can be reduced in many cases by adjusting the operating conditions or the addition of an effective lubricant or coating (Trent and Wright, Metal Cutting 2000, 76). BUE contributes to tool wear in the following way. As the BUE increases in size it becomes unstable and is removed. When this occurs, it may take part of the tool with it thus causing damage to the tool surface. In extreme cases the tool at this point is no longer acceptable for use (M. C. Shaw 2005, 33). This is similar to Case 3 outlined earlier where the harder material experiences wear. In some cases if there is no visible sign of BUE it does not necessarily mean that adhesion is not occurring. It just indicates that there is no net accumulation of workpiece material to the tool face due to an adhesive mechanism. Effective cutting fluids have been shown to prevent BUE (M. C. Shaw 2005, 267). Although BUE is undesirable it does for a period of time protect the tool face but overall BUE is an unwanted phenomenon.

Furthermore BUE may alter the rake angle which will affect performance and possibly surface finish (Trent and Wright, Metal Cutting 2000, 43).

2.3.6 Wear Reduction Techniques in Metal Cutting

Typical methods used to reduce wear in metal cutting are:

- Use of a cutting fluid.
- Use of surface engineered tool coatings.
- Choosing more appropriate tool and material combinations (i.e. material compatibility).
- Choosing more appropriate machining conditions (i.e. cutting speed, depth of cut, feed rate).
- Adding lubricious inclusions to the workpiece material.

Cutting Fluids:

Cutting fluids are typically used for one or all of the following purposes (Fox-Rabinovich and Totten 2007, 382,389):

- Reduce temperature due to the high heat capacity of many cutting fluids.
- Act as a low shear strength film to reduce friction. In some cases the lubricant will lower the shear strength of the workpiece (Rehbinder effect) and form wedge pressure in micro cracks that results in less energy to shear the workpiece (M. C. Shaw 2005, 278).
- Evacuating chips or aid in chip flow.

- Lowering the surface energy of the fresh chip surfaces which will reduce adhesion and transfer of material (will increase surface finish and efficiency).

It has been reported that cutting fluids as lubricants can contribute as much as 16-20% of the total manufacturing costs and can lead to some health, quality and environmental concerns (Sreejith and Ngoi 2000, 287). In contrast cutting tools are usually 2-4% of the total manufacturing costs (Byrne, Dornfeld and Denkena 2003, 12). In general the cutting fluids cost can exceed labour and overhead costs for some machining applications (Byrne, Dornfeld and Denkena 2003, 12). It is estimated in some cases that 10-30% of the cutting fluid may be wasted due to flooding and inappropriate use of the fluids (Dahmus and Gutowski 2004, 6). When selecting a lubricant it should be non-toxic, non-offensive (i.e. odour) to the operator, not damage the part or lead to corrosion of the part /machine or be a fire hazard. Compressed gases may also be used to carry away heat and cause beneficial chip breakage which may lower cutting forces and improve surface finish of the workpiece (M. C. Shaw 2005, 292).

Testing of cutting fluids can be done under real metal cutting conditions but large matrices of combinations are required. This results in considerable time, money and consumption of tools and workpiece material. Minimum quantity lubrication (MQL) or mist lubrication has the advantage of reduced need for waste treatment, reduction of lubricant purchasing cost, the ability to recycle chips without post-processing and evacuating the chips easier with a vacuum system (Fox-Rabinovich and Totten 2007, 393). MQL can also relieve environmental and

health concerns such as skin irritation, fumes, smoke, bacteria and odour concerns (Ezugwu 2005, 1363). However to reduce the lubricant some compensation must be made for the loss of fluid to reduce friction and wear. In some cases the thermal shock that comes for a hot cutting edge passing through the coolant can lead to thermal fatigue of the cutting edge which shortens tool life and offsets any benefits from the lubricity and overall cooling effect.

Material Compatibility:

As outlined with respect to reducing friction, simply picking a more suitable tool and/or workpiece material may be the solution to reducing wear if these materials tend to lower interface temperatures, reduce diffusion and reduce adhesion. Typically in many operations either the tool or the workpiece will be fixed and the range of allowable tool materials which can withstand the cutting load is limited. This makes the selection and development of coatings all the more important as an option for increasing tool life.

Operating Conditions:

Operating conditions are the machine settings such as cutting speed, feed rate and depth of cut. Cutting speed will have great influences on temperatures and cutting forces. Cutting speed may increase or decrease tool life. Depth of cut and feed force may also affect tool life. In the case of depth of cut for example, if the depth of cut does not exceed the nose radius of the cutting edge, ploughing will dominate rather than cutting from shear. This will result in higher cutting forces and shorter tool life. Thus in some cases, cutting more material per pass will

decrease wear. These parameters should not be trivialized and need to be investigated carefully.

Inclusions:

Since the real area of contact is approaching the apparent contact area in metal cutting on the rake face it is very difficult if not almost impossible to get lubricant to the rake interface to reduce friction and wear. Some research has been completed using textured surfaces applied to the rake face of the tool to retain the lubricant during machining. Also lubricious particles can be supplied by the workpiece, either by doping the workpiece material or through the use of glassy inclusions. Properly designed, they may come to the interface by diffusion under high temperatures and reach the interface and act as a solid lubricant (Gekonde and Subramanian 2002, 160).

Surface Engineered Coatings:

Of the tooling costs, which are already fairly low, coatings typically comprise only 16-20% of the tooling cost (Byrne, Dornfeld and Denkena 2003, 5). Hard lubricious coatings have made a large impact on machining as of recently and continue to grow in their usage. These coatings are typically very thin which has the benefit of not affecting dimensional tolerances and in many cases they do not change the perception of the product. Coating thicknesses are typically on the range of 10 microns so they have minimal impact on the dimensional tolerances of the cutting edge. In many cases, one cannot tell by the naked eye if a coating has even been applied unless there is a noticeable colour difference. Operation and

use is therefore "business as usual" from an operator point of view which is a benefit. It is generally accepted that in the seizure region a cutting fluid cannot penetrate the chip tool interface, thus if a properly selected coating is placed on the tool, a lubricious protective layer will exist between the tool and chip for some period of time. Childs cites that as much as about 80% of all carbide tools are coated. High speed steels and some ceramics are often coated as well. Childs defines the science and engineering of optimizing surface conditions of a material as *surface engineering* (Childs, et al. 2000, 109). According to Childs, one of the largest and continually growing areas in machining over approximately the last 20 years is surface coated technologies. One principle on which coatings can be designed is around the concept of "self-organization". This involves a surface responding to load and temperature in a way that serves to protect the surface. An example in nature is a callous on a human hand that forms due to friction. Similarly a mollusk shell generates many layers of inorganic and organic material which results in strength without being brittle. These concepts applied to nanocoatings could produce significant improvements in the use of engineered systems (Fox-Rabinovich and Totten 2007, 10-11).

Although it is desirable for the coating to be at least as hard as the tool material it should ideally also have a low free energy of formation which is an indication of its stability. Thus an ideal coating is a function of mechanical and chemical effects (Childs, et al. 2000, 111). Thicker coatings in general will last longer however too thick a coating will not be reinforced by the substrate and fail by spalling off the surface. Physical vapour deposition (PVD) and chemical vapour

deposition (CVD) processes tend to dominate the coating industry. PVD coatings tend to be smoother than CVD coatings. PVD coating is a cleaner process, is more versatile and minimizes the brittleness of the coating as compared to CVD (Sreejith and Ngoi 2000, 290). Properly selected PVD coatings tend to provide high hardness, low friction and shorten the chip-tool contact length (Fox-Rabinovich and Totten 2007, 232-233). CVD coatings are introduced as gaseous compounds that adhere to the substrate. PVD coatings are applied by ionized atoms attracted to the surface of the substrate due to a difference in potential. A sputtering process is used to clean the surfaces to ensure a strong adherence of the coating. PVD has the advantage of using lower temperatures to deposit the coatings. CVD coatings are often applied in the 800-1000°C temperature range whereas PVD coatings are typically applied in the 400-600°C temperature range (Trent and Wright, Metal Cutting 2000, 169-170). Thus PVD coatings are an advantage due to the fact that CVD coatings need extra care and precaution to preserve the microstructure of the tool. PVD coatings also tend to have less residual stresses and stress cracking (Trent and Wright, Metal Cutting 2000, 224). In general the diffusive process can be minimized with a properly selected coating (Childs, et al. 2000, 125). A properly selected coating will typically also show less adhesion/BUE on the rake face as evidenced by quick stop devices (Childs, et al. 2000, 138). Common coatings in use today are AlTiN or TiAlN coatings (same coating components but with different percentages of Al and Ti). Other common coatings are TiC, Al_2O_3, TiCN. Such coatings are commercially available at Oerlikon Balzers® and Kobelco®. As a result there has been much recent interest

in the use of multilayer nanocoatings. As Trent outlines these multilayers may serve one or more of the following functions: promote strong adherence to the substrate, provide thermal insulation, prevent diffusion or add lubricity to decrease friction (Trent and Wright, Metal Cutting 2000, 214). These coatings must work in synergy to have all their individual effects work as a whole when introduced to the other layers. Such multi-layer coatings in theory would provide better performance than a single monolayer as the individual coating layers can disperse energy more efficiently and "arrest" a crack before it propagates any further throughout the coating, thus increasing the life of the coating (Trent and Wright, Metal Cutting 2000, 215). While many coatings are monolayers, multilayer coatings do exist and the ideal coating according to Fox-Rabinovich is a multilayer coating termed a "smart" coating where each layer serves a specific function that is needed in the process. An example structure might look as follows in Figure 2.34 (Fox-Rabinovich and Totten 2007, 257):

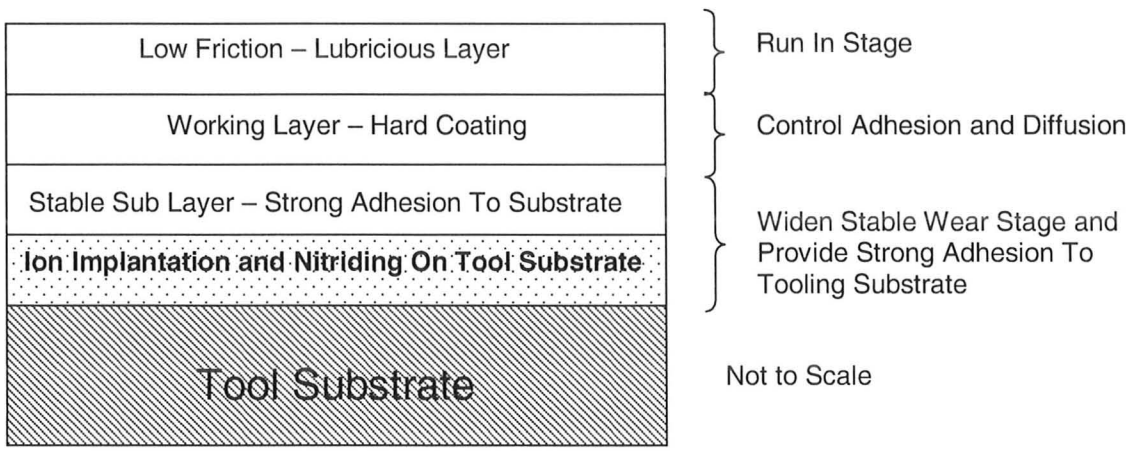

Figure 2.34: Illustration of a "Smart Coating" for Metal Cutting Applications

Because of the complexity of these coatings and the high number of combinations for the materials and layering of these "sandwich structures", much

testing is required to validate the beneficial role of each layer. This becomes expensive to do on an industrial scale. Thus a quick and reliable bench scale test in screening and selecting the most promising coatings for a set of potential coatings would be very beneficial. Thus it appears that many options exist for an engineer or operator to adjust to reduce wear. In general lubricants tend to work well but are costly and may pose health and environmental concerns. Coatings tend to be cheaper than lubricants and have been proven to work just as well. Operating parameters and material compatibility are typically worked out to an optimum (although not always the case) but they tend to often be a fixed variable in a process. Also, adding inclusions may be too costly or may be undesirable from a product point of view for performance or toxicity. Thus, assuming that the process is fairly optimized and appropriate materials are selected for the tool and workpiece, great promise and growth has been shown for surface engineered coatings in either dry or MQL conditions. Thus the ability to simulate surface engineered coatings realistically is a major goal of this thesis.

2.4 Design of Bench Scale Metal Cutting Experiments

The work of Trent outlines that "wear resistance is not a unique property of a tool material which can be determined by one simple laboratory test, or correlated with one simple property such as hardness" (Trent and Wright, Metal Cutting 2000, 224). Shaw has further noted: "metal cutting is an extremely complex process that cannot be described by a single mechanism. While a single mechanism may be predominant over a limited range of operating conditions, experience teaches that no single mechanism holds in general." (M. C. Shaw

2005). But industrial testing can be quite laborious and costly. There is a loss of manpower, loss of material and costs associated with purchasing test material, careful measurement is required and due to possible large scatter of data, multiple test repeats may be required (Trent and Wright, Metal Cutting 2000, 166). Machining and setup times for force dynamometers can take several hours and often subsequent tests require removal of the dynamometer which naturally leads to a different dynamometer setup each time it is assembled and dissembled. Also temperature measurement is difficult given the harsh nature of the environment and the fact that the most critical regions are not readily accessible. From personal experience it may take several days to test a few different tooling inserts on a workpiece material to determine based on limited test replicates which tool insert is better. Thus the advantages of using a bench scale apparatus to simulate metal cutting conditions on a preliminary basis become useful to screen tooling conditions and coatings. If it can be demonstrated that this bench scale approach correlates to the same friction and wear trends found in metal cutting, the number of coatings tested in a set period of time can be increased to complete a more detailed framework for the machining operation. Furthermore, temperature and stress in machining are a result of the inputs: operating conditions and material selection. In a bench scale test, stress and temperature may be designed as inputs to study the isolated effect of each variable. Once this information is known then operating parameters of the real machine may be tuned to capitalize on this knowledge. FEA machining models for example could be used to aid this design process. Thus a large matrix of testing conditions may be simulated on the bench

scale, narrowed down to a small number of top performing candidates and conditions which can then be validated on an industrial machine. Figure 2.35 is an illustration of the current feedback test setup in the MMRI and the proposed feedback test setup with a properly design bench scale test. In sum there is no substitute for the real test. That is, metal cutting is metal cutting and a simulation will never be exactly the same. However, in lieu of time and cost, a reliable bench scale test with proper design will be an added research tool that may act as a reliable and cost effective filter or snapshot to minimize testing and cost while expanding the matrix of testing conditions. Tests still require validation on the real machine. As a final direct quote Shaw notes: "While bench tests often serve a useful role in screening tests, there is unfortunately no satisfactory substitute for direct machining trials under conditions that are close to those being used in practice. The selection and application of metal cutting fluids is very much an art rather than a science as are so many other aspects of metal cutting. The main role of theory in metal cutting is often not to predict what will happen but to understand what is observed in order to reduce the number of trials required to reach the desired objective" (M. C. Shaw 2005, 300).

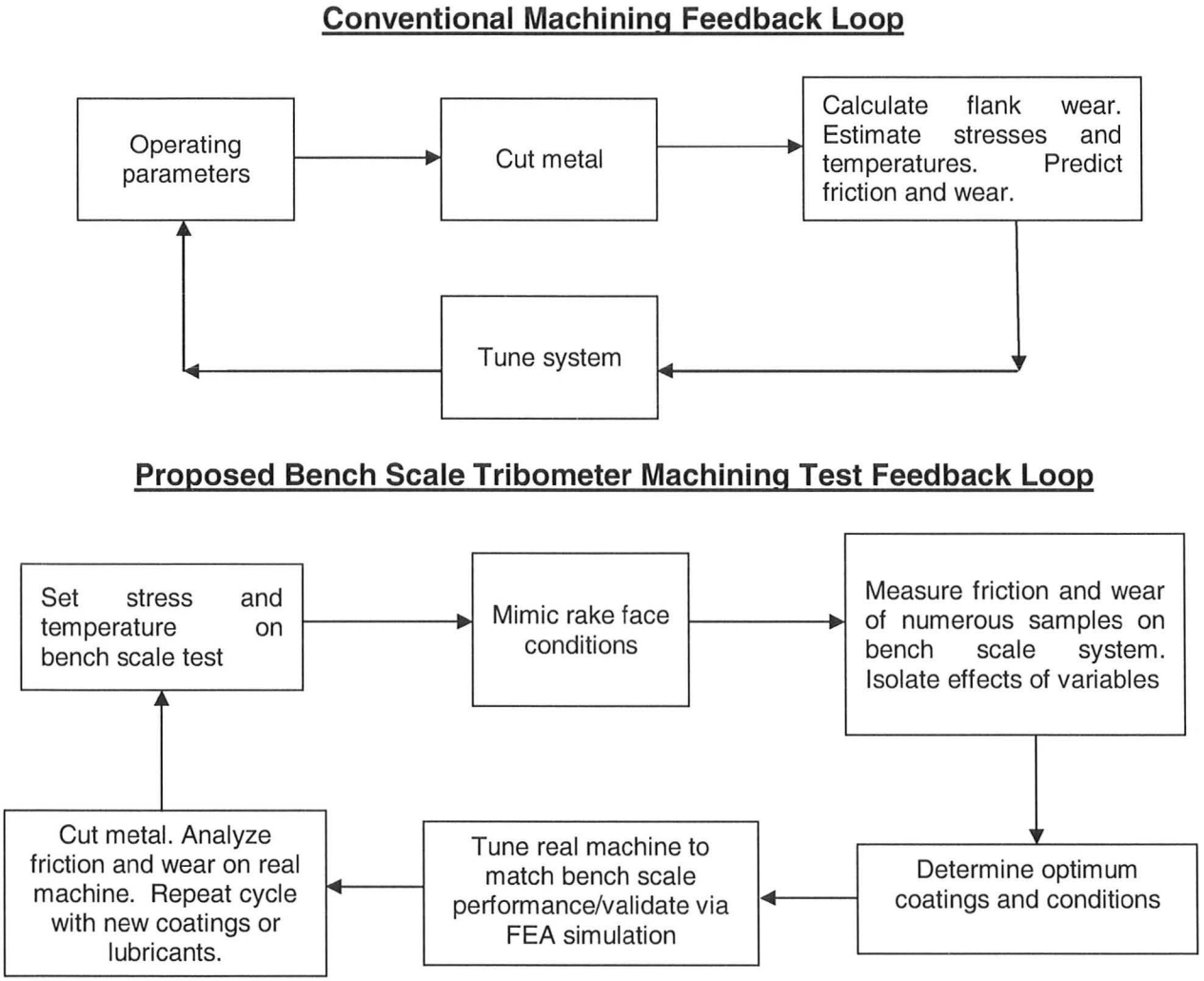

Figure 2.35: Machining Feedback Loops: Current vs. Proposed

2.4.1 Fundamentals of Tribological Design

Gwidon Stachowiak has concisely outlined the fundamentals of tribology testing in his text, *Experimental Methods in Tribology*. Arnell has also proposed valuable theory. No unifying theory of friction exists. As a result it is generally regarded that experimentation must supplement any theory (Arnell, et al. 1991, 29). Simply put, the phenomena dictate the theory in many cases rather than other disciplines like theoretical physics where the theory precludes the experiment or phenomena (Stachowiak 2004, 6). Arnell, who has over 20 years of extensive

tribology experience, cites the following quote from his experience which is a prime motivation for this experiment: "It is generally agreed that the only safe way to select materials to resist wear in a particular situation is on the basis of tests – first, realistic bench tests and then field tests" (Arnell, et al. 1991, 66-67). Stachowiak also states "in general, no single experiment can provide data relating to all the influences or factors controlling wear and friction" (Stachowiak 2004, 329). In general tribology becomes a highly empirical study to compensate for the lack of data and knowledge about all the controlling parameters that govern a highly complex scenario. Almost all published work on friction is based on correction factors for the theory to fit that particular experiment (Arnell, et al. 1991, 67). In general dominant mechanisms must be discovered, isolated and simulated in a repeatable compartmentalized approach. In general normal stress is one of the most important variables. While load is important, experimental loads do not need to match as long as the stresses generated are the same. This is because stress is fundamentally related to asperity and material characteristic response. Temperature also has a major impact on friction and wear. There are two types of temperature simulations. The first is an external heating whereas the second is due to friction alone from heat dissipation in sliding. In general the temperatures should be simulated as close as possible to the real situation (Stachowiak 2004, 18). Stachowiak notes in general as the fundamental law of tribology that every element should be simulated as closely as possible to the application. Sliding speed is a further variable of interest as it dictates temperatures. Surface finish will affect abrasion and fatigue wear. Contamination and surface films are

generally the final significant variables. Humidity should be constant and the samples should be free of contaminants not present in the real application. In general the sliding distance/time is important as a steady state value should be reached (Stachowiak 2004, 16-17). As a result, a well designed experiment is invaluable but in all modesty the user of such an experiment must be cautioned in the use of such data. The data and results must be analyzed in numerous ways from past experience, spectroscopy techniques, mathematical modeling and field testing to ensure the proper application of the results. Such experiments are not meant to replace field testing but rather enlighten or elucidate the situation to provide better screening and insight into the phenomenon in order to help design better engineered uses of materials. The experiment should be considered to add potential to finding a solution or be a component to a solution and not necessarily the complete solution. Stachowiak notes that it is widely recognized that a tribometer cannot replicate all aspects of metal cutting due to the number of experimental variables and the extreme conditions. Also the criterion of performance usually is more complex, as productivity, tolerance, surface finish and tool life are all competing factors. There is no single performance index.

Experiments may be carried out as conformal or non-conformal tests. A conformal test has the sliding surfaces "match" up whereas a non-conformal test does not. This is illustrated in Figure 2.36 (Arnell, et al. 1991, 30).

Figure 2.36: Conformal vs. Non-Conformal Tests

Non-conformal setups are typically desirable for an accelerated friction and wear test due to the more aggressive interaction with higher contact stresses. (Arnell, et al. 1991, 30). Furthermore a test should have repeatable and safe instrumentation with continuous data acquisition of all the key variables in order to capture all subtleties in the response of the system to friction and wear. High data logger sample frequencies should be used. Tests in general should be continuous and not stopped and re-started periodically. Samples should be analyzed before and after testing. A white light interferometer, a high resolution microscope with stitching capabilities and SEM are useful for these analyses. EDS (Energy Dispersive Spectroscopy) on an SEM is useful to characterize material transfer or diffusion. Stachowiak notes that simple changes in colour or texture may reveal a lot about the wear process. R_A, R_Q, R_{PV} should measured before and after the test.

Rabinowicz suggests two methods for cleaning a sample. One method is by cutting or abrading with a clean surface and/or lapping/polishing. The second method involves acetone and/or isopropyl alcohol (less aggressive). Samples should be prepared in a systematic fashion and result in consistent geometries. If grinding or polishing of the specimens is used the user should be aware that abrasive particles, contaminants or residual stresses may now be on the thin surface layer of the material (Stachowiak 2004, 152). Ideally the final cleaning

stage should be right before the test so that no contaminants from the air or other sources reach the surface. To avoid contamination after cleaning the specimens should be handled with gloves and tweezers.

Stachowiak notes that a tribometer that must operate in extreme conditions such as high temperatures, adequate care must be taken to protect the sensitive measurement devices from the high temperatures and also shield them from any potential noise sources that will damage or induce errors in the readings (Stachowiak 2004, 33). These observations and rules of thumb outlined by Stachowiak and Arnell also agree with the extensive work of Kuzmin et al in their paper entitled *An Approach to Tribotesting Simulation and Tribotesting* (Kuzmin, Shuvalova and Checkina 1996, 199-209). Stachowiak notes that as many experimental variables as possible should be recorded together in real time.

The Society of Tribologists and Lubrication Engineers (STLE) recognize over 200 different tribometer test rigs; however only a few are standard. As a result it is generally accepted that a test rig will need to be constructed as a hybrid of other designs or be designed from scratch to suit the specific needs of an experiment (Stachowiak 2004, 157). Although many tests vary they do share the common ground that no motion commences before all the variables of interest such as load and temperature have stabilized. One of the most common tribometer designs is the pin on disk tribometer. The pin is made out of one material and the disk of another material. Often the pin is the harder material. This design has the disk rotate with its centre of rotation offset relative to the stationary pin. The pin is

often flat ended or hemispherical. Schey notes that a hemispherical pin is better to avoid ploughing (Schey 1983, 210).

In general, ASTM has developed standards for pin on disk tests which is designated ASTM #: G99-05: *Standard Test Method for Wear Testing with a Pin on Disk Apparatus*. The document outlines several useful test parameters based on experience:

- Thickness of disks should range from 2mm to 10mm.
- Pin diameters should have a radius/curvature on the tip and should range from 2mm to 10mm.
- Disk diameters/cross sectional area may range but should be consistent with Brinell testing standards (to be detailed later).
- Surface finish of specimens should be 0.8 microns or lower using R_a.
- A minimum of 3-5 test replicates should be completed for each test.
- Coefficient of friction is a standard reporting value for performance.
- Standard deviation is usually sufficient in addition to the arithmetic average of the coefficient of friction.

Alignment is critically important so that vibration, damage or noise in the data does not ensue. As a result some pins are lapped with diamond paste, use chamfered edges or a spherical tip. If there is misalignment there will be uneven wear and the friction measurement will fluctuate with RPM of the disk. Also accumulation of material on the pin over a period of time will result in a very uneven surface. The work of Godfrey found that in general conventional tribometers that operate with the pin off centre to the disk rotation axis have

vibration issues which results in the load being reduced. Also the friction values in such a setup are typically noisy. As a result, reporting a single friction value at steady state becomes subjective and cumbersome. Godfrey noted that at very low speeds these oscillations will be removed, however the temperature generated may not be very high and require external heating as compensation (Godfrey 1995, 119-120). These conditions mentioned may not always be available or practical options but if possible, they are recommended as a way to reduce experimental variability (Stachowiak 2004, 160). These typical tribometer designs are not suitable for metal cutting conditions with high stresses and temperatures (Stachowiak 2004, 29). This is also noted by Bonnet et al. who found that a traditional tribometer does not reach the temperatures and stresses typically found in metal cutting (Bonnet, et al. 2008). Furthermore, as noted by initial testing in the MMRI, a traditional offset pin on disk will cause excessive ploughing and vibration. Grzesik also notes that a standard "off the shelf" tribometer pin on disk design is not suitable for metal cutting conditions (Grzesik 2000). This was also noted by Cristino et al. (Cristino, Rosa and Martins 2009, 170). However the concept and much of literature published on these pin and disk units are still useful as a starting framework.

Industrial tests have been completed by other researchers whereby the machine such as a lathe is modified to have a special temperature thermocouple and force sensor however this is still an estimate of the parameters since the cutting zone is not accessible. Furthermore, in addition to the high cost of such a setup the machine may need to be dedicated solely to this test (Rech, Kusiak and

Battaglia 2004). Setting up the unit and taking it apart would be time consuming and alter the setup each time it is completed. A similar design was also employed in the work of Bonnet et al. who used a modified lathe setup to test tribolgoical interactions in machining conditions (Bonnet, et al. 2008). Cost again was an issue and setup was noted by Bonnet to be non-trivial.

2.4.2 Brinell Hardness Testing

An elegant solution to these metal cutting tribological design issues is found in the Brinell hardness test approach. Due to the requirement for subsurface plastic flow and stresses in the range of 1-3GPa, the spherical tipped Brinell hardness test is a suitable candidate. The benefits of a spherical pin design allows for high stresses, isolating a point contact for the friction, a forgiving design for slight misalignment and the contact mechanics of this non-conformal test are well established. A Vicker's or Rockwell type interaction may have a sharp tip which if misaligned during sliding could cause damage and the pointed tip is difficult to manufacture (note all of these indenters are non-trivial to construct but Brinell is the least difficult). Thus a spherical tipped pin was found in literature to be the best design for reuse and safety. Several prominent researchers have used such a design and their applications will be discussed in further detail after outlining the key features of Brinell hardness testing. The contact mechanics of Brinell testing will be discussed at this point as well as the ASTM procedural aspects.

In Brinell hardness testing the pin is usually made out of a tungsten carbide. The workpiece or disk is a softer material mounted with a flat face perpendicular to

the direction of loading. The diagram in Figure 2.37 shows the evolution of the indentation in such a test. The disk will deform plastically up to a critical depth.

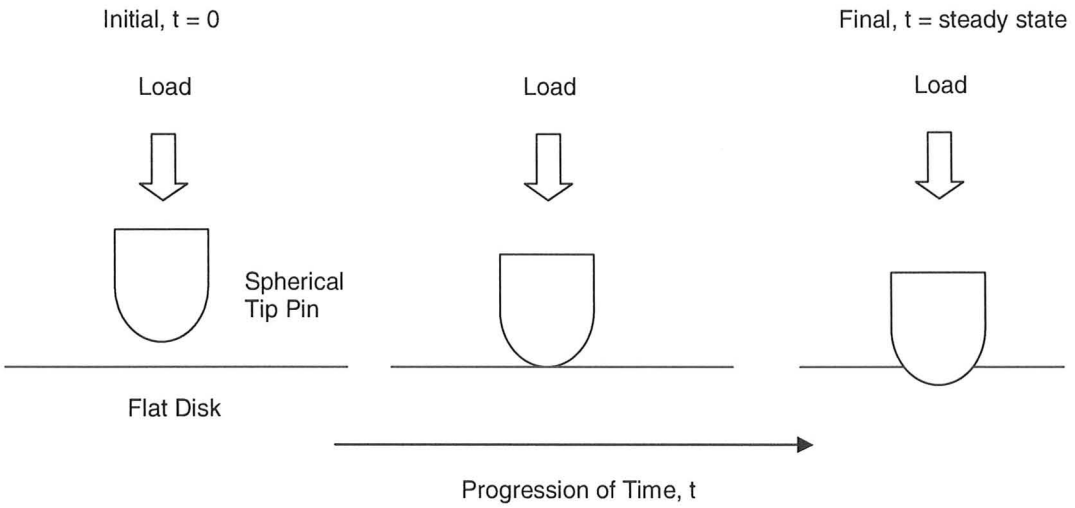

Figure 2.37: Illustration of Brinell Hardness Testing Over Time

Classical Hertizan contact mechanics do not apply as it is developed for elastic-elastic contact not elastic-plastic contact (Bowden and Tabor 1950, 10). As will be shown the stress at the interface is more or less of a uniform profile with a sharp drop off in stress at the edges of contact. Figure 2.38 is based on a modification of a sketch presented by Shaw (M. C. Shaw 2005, 65-66). The stress is a maximum at the centre and tapers off to a value of 0 at the outer radius of contact, R_{IND}.

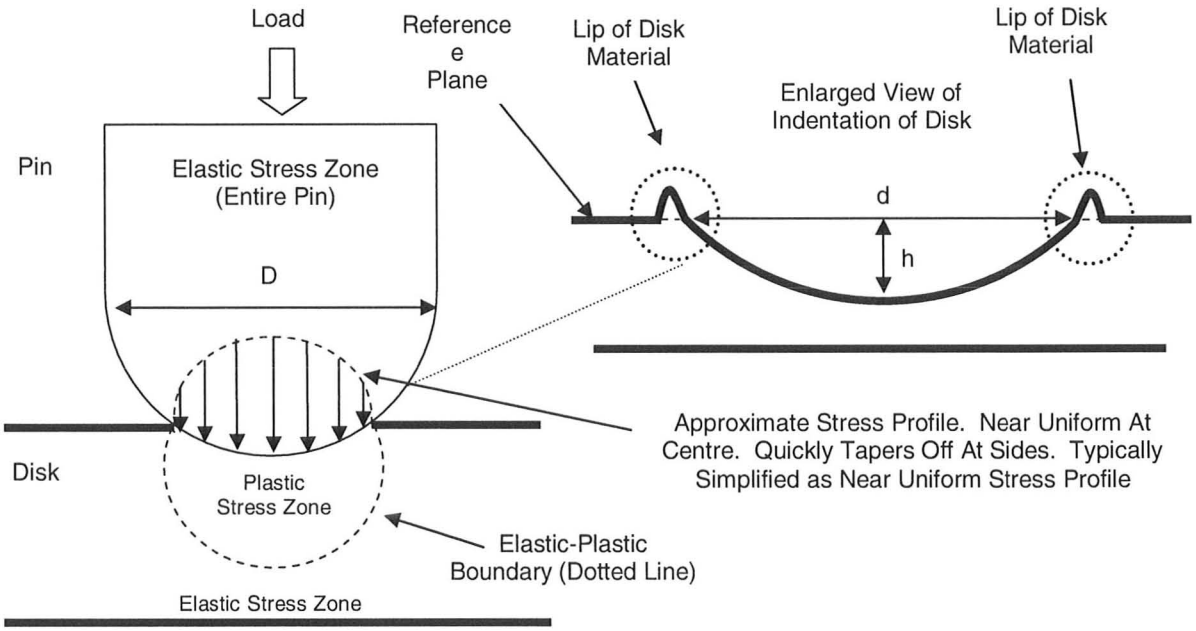

Figure 2.38: Illustration of the Stress Profiles at the Interface of the Brinell Hardness Test

Brinell hardness number, HB is defined as the load per unit area of spherical contact area (i.e. a stress). The standard is that the Load (L) is represented in kilograms (kg) and the surface area (A) of the curved contact surface in square millimetres (mm^2). The equation for the curved contact area (A) in this case equal to πDh as derived from an integrated surface of revolution calculation. This calculation was verified by Foster in his text, *The Mechanical Testing of Metals and Alloys*.

$$HB = \frac{L}{A} = \frac{L}{\pi D h} \qquad \text{Equation 2.42}$$

According to Foster and ASTM, the print diameter, d, should be measured in at least 2 places and averaged using a microscope with high resolution. The diameter should be measured in the reference plane of the specimen to avoid measuring build up or the deformed lip of the disk material. This is illustrated in

Figure 2.39 for a microscope measurement. If there is concentricity the 2 print diameters should be very similar.

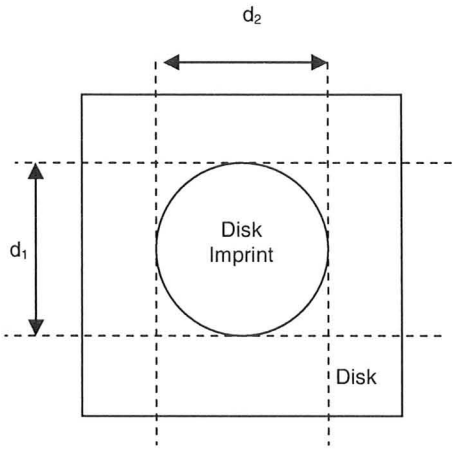

Figure 2.39: Measurement Method of Disk Impression Diameter, d

$$d = \frac{d_1 + d_2}{2} \qquad \text{Equation 2.43}$$

Using a white light laser interferometer for the same calculation two measurements can also be made. The interferometer will aid in verifying that the reference plane measurement is made and not the pile up diameter. The centre of the impression can be found by constructing two profile lines perpendicular to each other and moving the lines around until the maximum depths match in the centre.

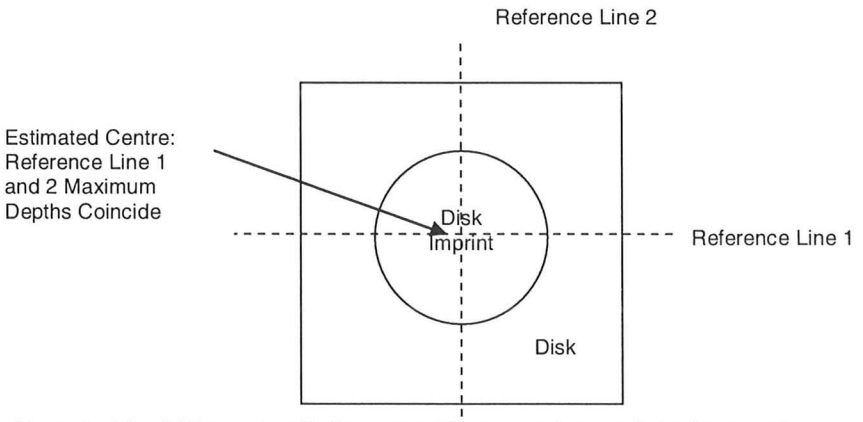

Figure 2.40: How to Find Diameter Reference Plane on Laser Interferometer

The result was found from testing that the optical microscope tends to slightly over predict d and as a result over predict h. The laser interferometer values correlated with theory well. One thought is that the optical microscope, while having an accurate resolution cannot discern between the edge of the pile up and the intersection of the indentation with the reference plane. This is illustrated in Figure 2.41.

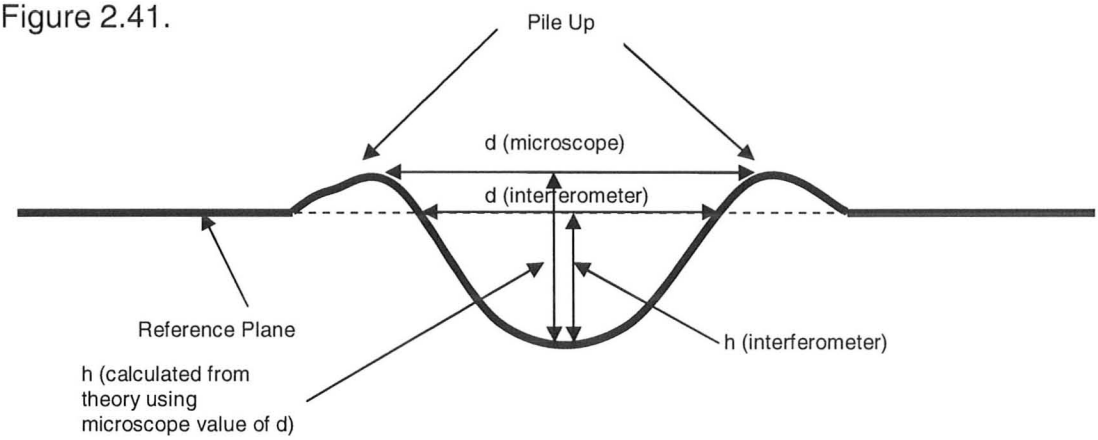

Figure 2.41: Interferometer vs. Microscope for Measurement of Indentation Diameter

Preliminary testing on Ti6Al4V showed the microscope over predicts the impression by about 5% on average when pile up existed. Meanwhile the laser interferometer agrees nearly perfectly with the theory. As a result the laser interferometer should be used for all analysis if possible if pile up exists. As an approximation however the lab microscope value of d can be multiplied by 0.95 to estimate the value of the real value of d if the interferometer is not available.

$$d_{interferometer} \cong 0.95 d_{optical\ microscope} \qquad \text{Equation 2.44}$$

With no build up or lip an optical microscope is sufficient. This will need to be evaluated on a case by case basis. The value of h is not as easily measured in a laboratory setting as the value d. As a result, Equation 2.42 will be expressed in terms of D and d to simplify the measurements performed in the lab. Figure 2.42

was constructed to help relate h to D and d. To help visualize this derivation Figure 2.42 is provided. Whether the situation is a full sphere indentation or a half sphere indentation, the contact mechanics are the same with d < D in all cases.

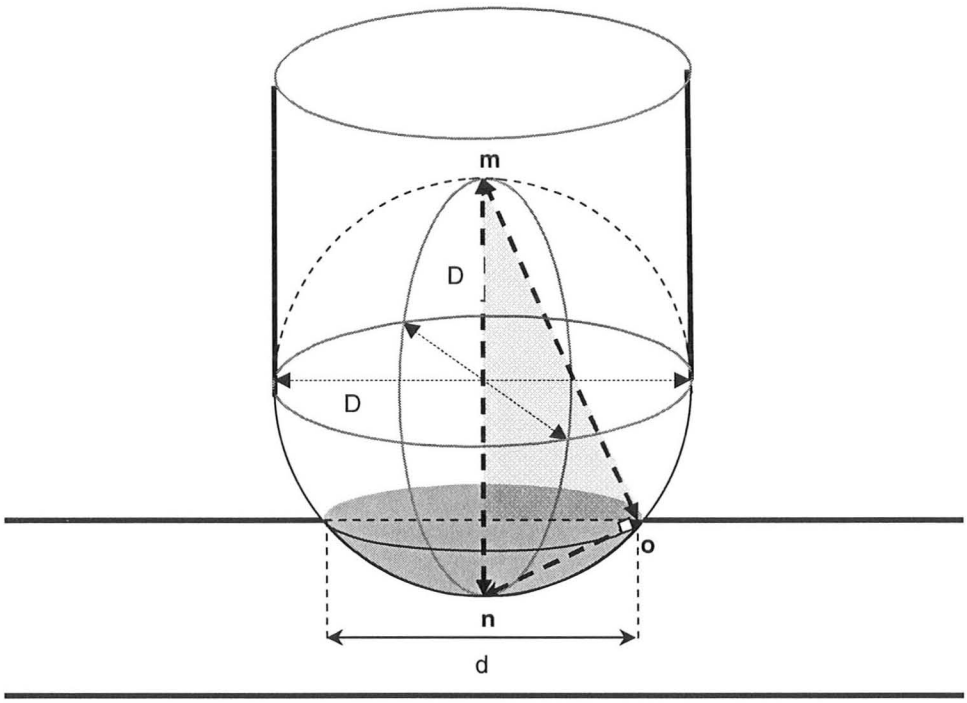

Figure 2.42: 3D Representation of Test Indentation – Spherical Projection Shown

From basic geometry, the angle **<nom** must be 90 degrees. From this representation, **mpo** and **npo** are similar triangles. This concept will be used to isolate the indentation depth h, as a function of the diameter of the sphere (D) and the diameter of the indentation (d). As a result, length **np** divided by **po** must be equal to length **po** divided by **pm**. This equates to:

$$\frac{h}{d/2} = \frac{d/2}{D-h} \qquad \text{Equation 2.45}$$

Rearranging this equation yields the following result:

$$h^2 - hD + \frac{d^2}{4} = 0 \qquad \text{Equation 2.46}$$

Solving we get

$$h = \frac{D \pm \sqrt{D^2 - d^2}}{2} \qquad \text{Equation 2.47}$$

In order for the diameter of the imprint to be less than the total diameter of the sphere, only the following solution is acceptable. As a result:

$$h = \frac{D - \sqrt{D^2 - d^2}}{2} \qquad \text{Equation 2.48}$$

As a result the surface area of the spherical print assuming a hard pin and soft disk can be written as:

$$A = \pi D h = \pi D \left\{ \frac{D - \sqrt{D^2 - d^2}}{2} \right\} \qquad \text{Equation 2.49}$$

This leads to the conventional solution for the Brinell hardness, HB which is commonly published in literature:

$$HB = \frac{2L}{\pi D[D - \sqrt{D^2 - d^2}]} \qquad \text{Equation 2.50}$$

Meyer hardness testing is the same testing as Brinell however it uses the projected contact area ($\pi d^2/4$) rather than the curved area of the contact. It has been shown that using either surface area makes minimal difference to the result and the Meyer approach is often taken over the Brinell method of contact area because it has been found to represent the mean normal compressive stress more accurately (M. C. Shaw 2005, 60).

In general if the impression is not too deep, the true contact area using Brinell will vary by only a few percent with the projected area measured by Meyer's approach (Tabor 1970, 146). Nevertheless this provides a basic approach to the key variables and the method of testing with Brinell. FEA and experimental studies

have been completed regarding the normal stress profile. The works of Johnson (1968), Yew and Goldsmith (1964) and Francis (1976) support a near constant stress profile or slightly convex profile with the stress being more or less uniform in the centre and dropping off rapidly to 0 at the edges (Biwa and Storakers 1995, 1318-1319). Based on a preliminary ABAQUS FEA model, the slightly convex stress profile with stress constant in the middle and dropping off to 0 at the edges was observed. Thus the modelling used in this research will assume for now a uniform stress profile based on the projected Meyer area.

Based on the work of M.C.Shaw (M. C. Shaw 1971, 2-3,15), Tabor (Tabor 1970, 147) and the established ASTM standards of Brinell testing (ASTM # E10-08), the following criteria and notes are of importance for a Brinell test to be accurate and reliable:

- Indenter should be made of tungsten carbide with 5-7% cobalt content. This material is listed in ASTM E10-08 as a top choice of spherical indenter material. Other materials are acceptable but they must be extremely hard.
- ASTM E10-08 notes that when the disk material is in the Brinell hardness range of 95.5 to 650 HB (note Ti6Al4V is approximately 334 HB and Inconel is approximately 360-400 HB) the required load of a 2.5mm diameter tungsten carbide ball is approximately 1839N.
- For a Brinell test to be valid ASTM E10-08 states that the diameter, d, of the indentation should be about 24-60% of the indenter diameter, D. The ASTM guide notes that a single force is acceptable for carrying out all Brinell hardness testing as long as it is sufficiently high.

- The diameter (d) of the imprint should be taken in at least two spots, ideally perpendicular to each other and averaged.
- The diameter measurement should be completed on a microscope with etched measuring lines and high resolution to capture the true value of d. The measurement resolution should be at least about 0.0025mm. A valid Brinell hardness test should not have the two measurements of d vary by more than 0.1mm.
- The load should be held a minimum of 10-30 seconds in a test.
- The indenter material needs to be at least 2 times harder than the disk material.
- The cross sectional area of the disk specimen surface must be several times larger than the diameter (d) of the impression.
- The thickness of the disk should be at least 10 times the depth of the indentation (h).
- If multiple indents are completed on the same surface, the indents should be separated from each other by approximately 3 to 4 times the diameter (d) of the indentation from edge to edge of the indentations so that the impressions do not influence each other.

Shaw also notes that surface finish in a Brinell hardness test is of minimal significance as the high loads flatten the asperities such that the real area approaches the apparent area (Blau 1971, 34). That is not to say an extremely rough surface is acceptable, however typically grinding operations that produce a R_a around 0.5-0.8 microns or better is usually acceptable. ASTM E10-08 does not

specify a typical roughness value other than the disk specimen should be ground or machined sufficiently in order that the edge of the indentation is smooth enough to accurately pick up on a microscope. Researchers have modified this test for friction testing, which is known commonly as a modified Brinell hardness test. This test produces a Brinell print and then rotates either the indenter or the disk with the indenter centre being on the axis of rotation of the disk. As a result a Brinell print is made and a friction reaction torque from the interaction is produced. External heating has been implemented in one case to simulate metal cutting conditions. This will now be discussed in further detail.

2.4.3 Published Modified Brinell Hardness Tests for Metal Cutting Simulation

Two notable bench scale machining simulations have been completed to date based on the modified Brinell hardness test. Notably the first was pioneered by M.C Shaw in 1960 in the *Journal of Basic Engineering*, with the journal title: *Friction Characteristics of Sliding Undergoing Subsurface Plastic Flow* (Shaw, Abraham and Mamin 1960, 342-346). M.C. Shaw was a leader in metal cutting and proposed an idea for such a bench scale test to simulate metal cutting on the rake face of a tool. Shaw's work was all performed under near zero velocity (due to being on centre) seizure conditions. This test specifically isolates the plastic flow in the seizure zone of the rake face. Similar tests were used by Schey who outlines 6 variations of this type of test, one of which was Shaw's setup. An alternative name proposed by Schey is a twist compression test. Reid also cited Schey's work as a potential source for metal forming tribology based on numerous successful lubricant tests using this setup (Reid 2005, 50-52) Schey notes the

advantages of this test as developing high plastic loads in a stable manner because the ploughing component is negligible, the speed is low and thus the plastic adhesive mechanism in near seizure conditions is isolated (Schey 1983, 211-212). As metal cutting is a highly loaded slider, Shaw anticipated simulating such conditions in regions 2 and 3 from Figure 2.14 where the real area of contact approaches the apparent area of contact.

This experiment by Shaw is also briefly outlined with additional references on page 163 of his 2005 *Metal Cutting Principles* text.

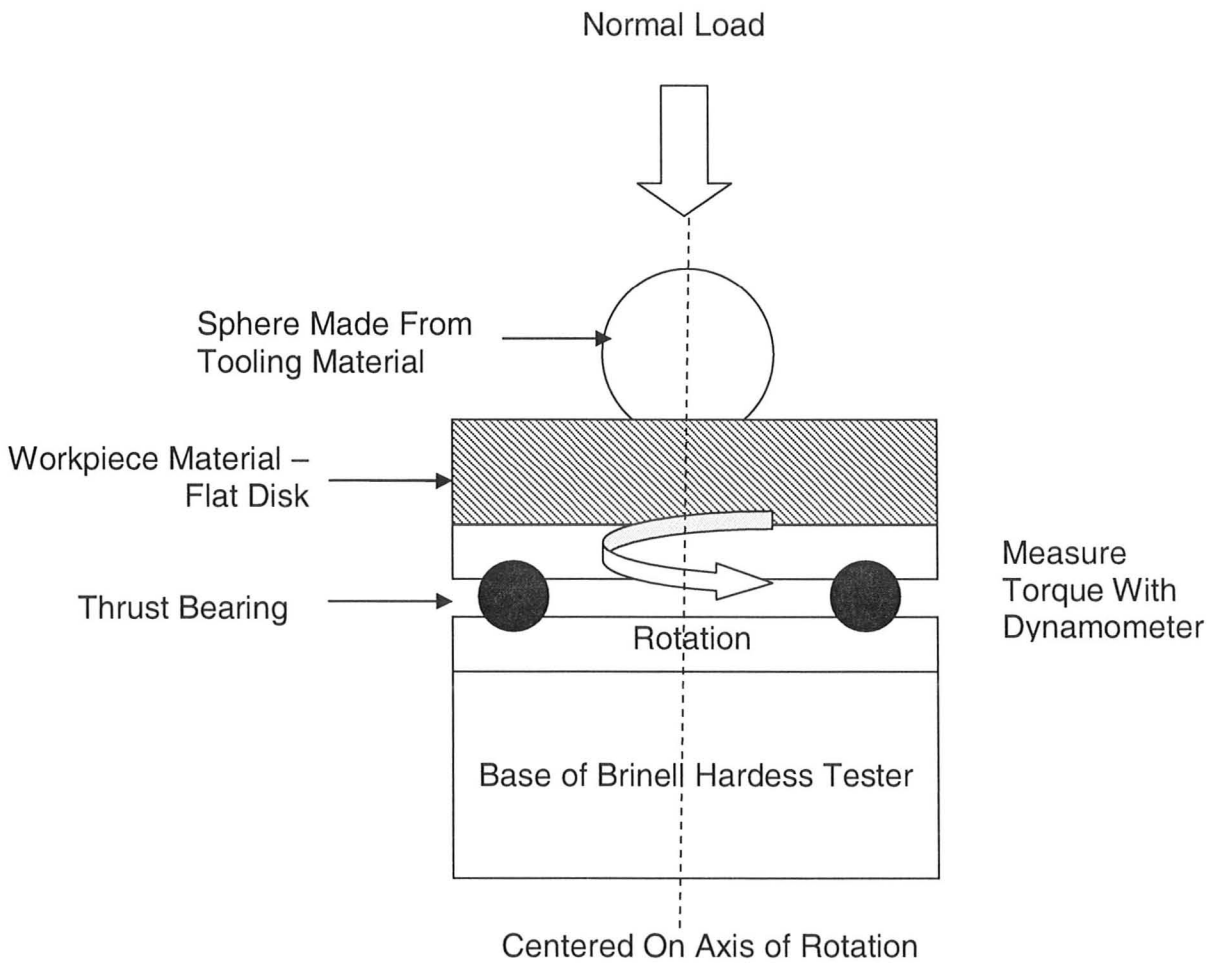

Figure 2.43: Shaw's Modified Brinell Hardness Test for Subsurface Plastic Flow On Rake Face

The result is a hemispherical impression in the disk after the test. The radius of the imprint is measured and related to the torque measurement to determine the coefficient of friction. Shaw noted that speed of rotation had minimal influence (2-1000RPM) and that steady state tended to be found for most materials by at most 1 complete revolution of the disk (Shirakashi, Komanduri and Shaw 1978, 197).

Shaw's results followed the trend for frictional shear stress vs. time (Shirakashi, Komanduri and Shaw 1978, 198) shown in Figure 2.44.

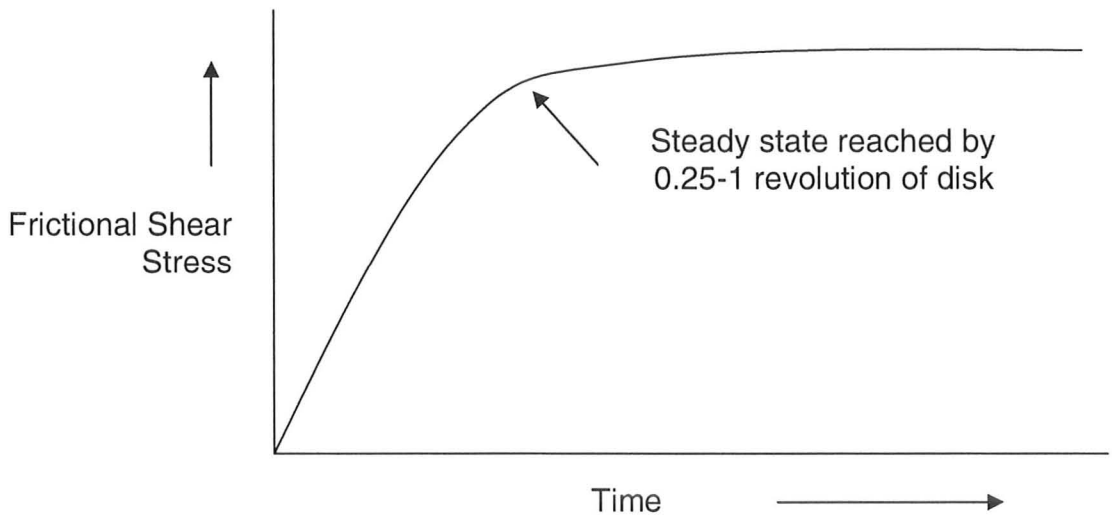

Figure 2.44: Trend of Frictional Shear Stress Reported by Shaw for Modified Brinell Test

Shaw's initial testing used normal stresses that averaged around 1 GPa. Shaw reported coefficients of friction using this setup ranging from 0.05-0.3 depending on the setup conditions and materials (Shirakashi, Komanduri and Shaw 1978, 197). Shaw however did not simulate metal cutting temperatures. The second test of a similar nature is by the work of Dr. L.S. Shuster which is outlined in detail by Lyapin (Lyapin 1969). Dr. Shuster devised a setup like Shaw's by constructing a modified Brinell hardness test with several improving

modifications. Shuster used electrical resistance heating to heat the interface up to 1000°C (whereas Shaw used no external heating and the frictional heat dissipation was minimal). Shuster also used loads to generate normal stresses in the range of 1-3GPa. Shuster used a 2400N constant load for a 5mm diameter hemispherical pin. A sketch of Shuster's setup is in Figure 2.45. Shuster rotated the pin relative to a stationary disk whereas Shaw rotated the disk relative to a stationary pin. Shuster's design has the advantage of minimizing alignment issues.

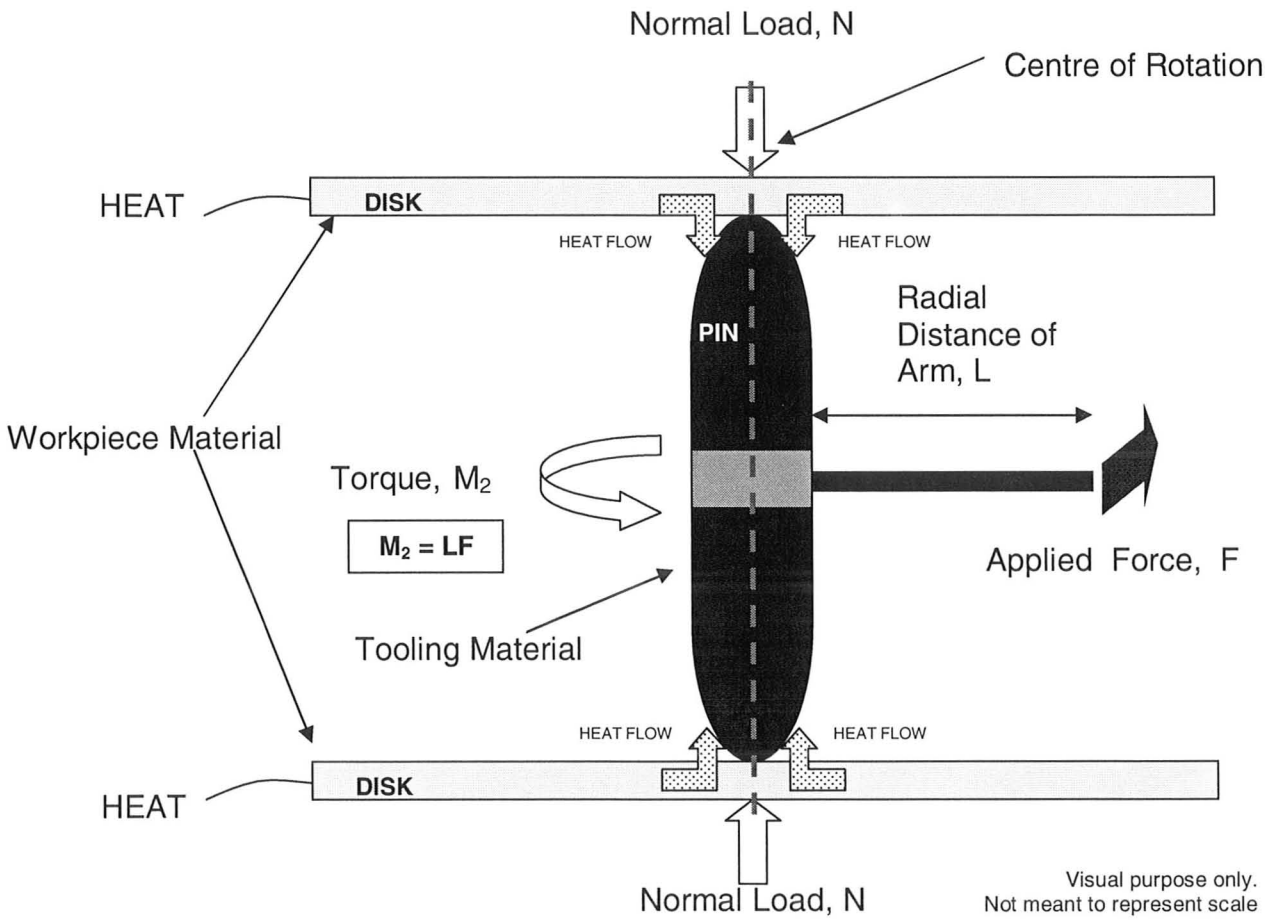

Figure 2.45: Shuster's Modified Brinell Setup

Because of Shuster's design there are 2 contact points to analyze for friction which are assumed to be identical.

Shuster uses 1RPM for rotation of the pin however the length of test varies on a case by case basis. Similar work by Plakhtii using Shuster's setup and 8 RPM of rotation stated that the rotation should be slow to eliminate temperature effects, add mechanical stability and mimic seizure as closely as possible (Plakhtii 1990, 217). Shuster's plots the evolution of COF with temperature for a constant load as his output. The collaboration of the MMRI with Dr. Shuster via Dr.G.Fox-Rabinovich has shown in several cases that the trends in coefficient of friction in such a test agree with metal cutting wear trends. Four cases will be outlined. All COF values are from Shuster and are the average result of 3 replicates per test point and contain a maximum of 5% deviation from the listed average test point value. For each case, the 1st graph is COF from Shuster's tribometer as a function of temperature. The 2nd graph below is the MMRI machining data for the same tribo-pair.

Table 2.7: 4 Cases Based on Shuster's Design

Test Case	Operation	Tool Material	Workpiece Material	Cutting Speed (m/min)	Feed Rate	Depth of Cut (mm)
1	End Milling	Tungsten Carbide	H13 Die Steel	220	840mm/min	5 (axial) 0.6 (radial)
2	Turning	Tungsten Carbide	Inconel 718	40	0.125mm/rev	0.25
3	Turning	Tungsten Carbide	Inconel 718	60	0.125mm/rev	0.25
4	Turning	Tungsten Carbide	Ti6Al4V	150	0.125mm/rev	0.25

Sources:
Case 1: (Fox-Rabinovich, Yamamoto and Veldhuis, et al. 2006)
Case 2: (Fox-Rabinovich, Yamamoto and Aguirre, et al. 2010)
Case 3: (Biksa, et al. 2010)
Case 4: (Biksa, et al. 2010)

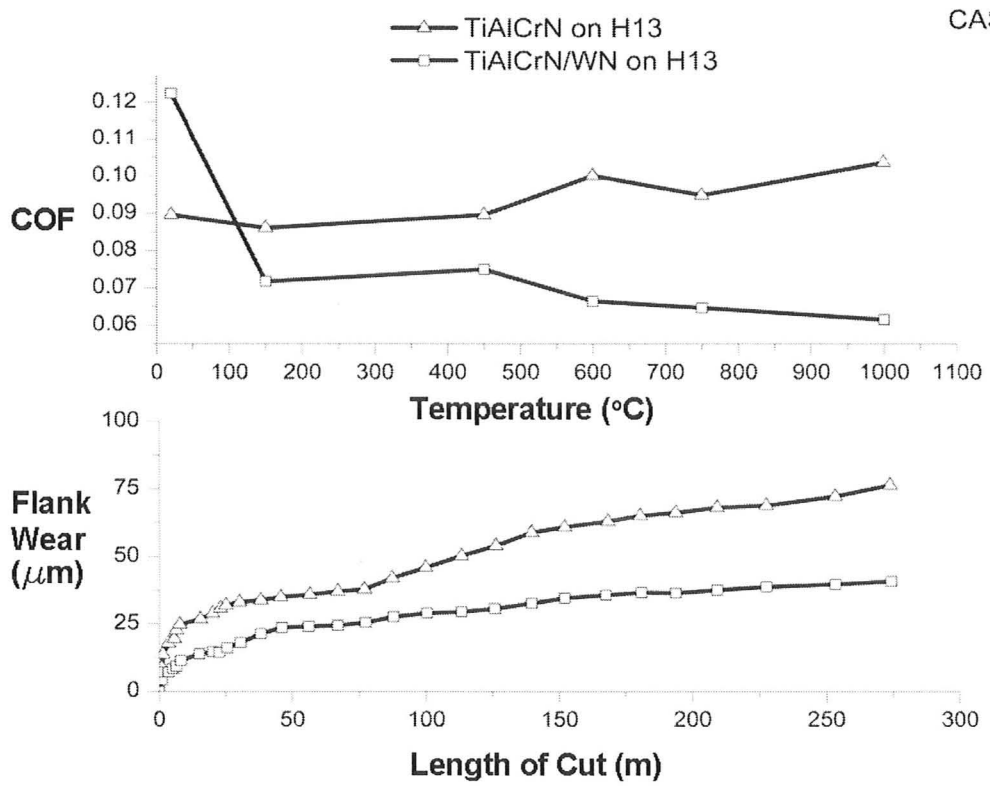

Figure 2.46: Shuster Case 1

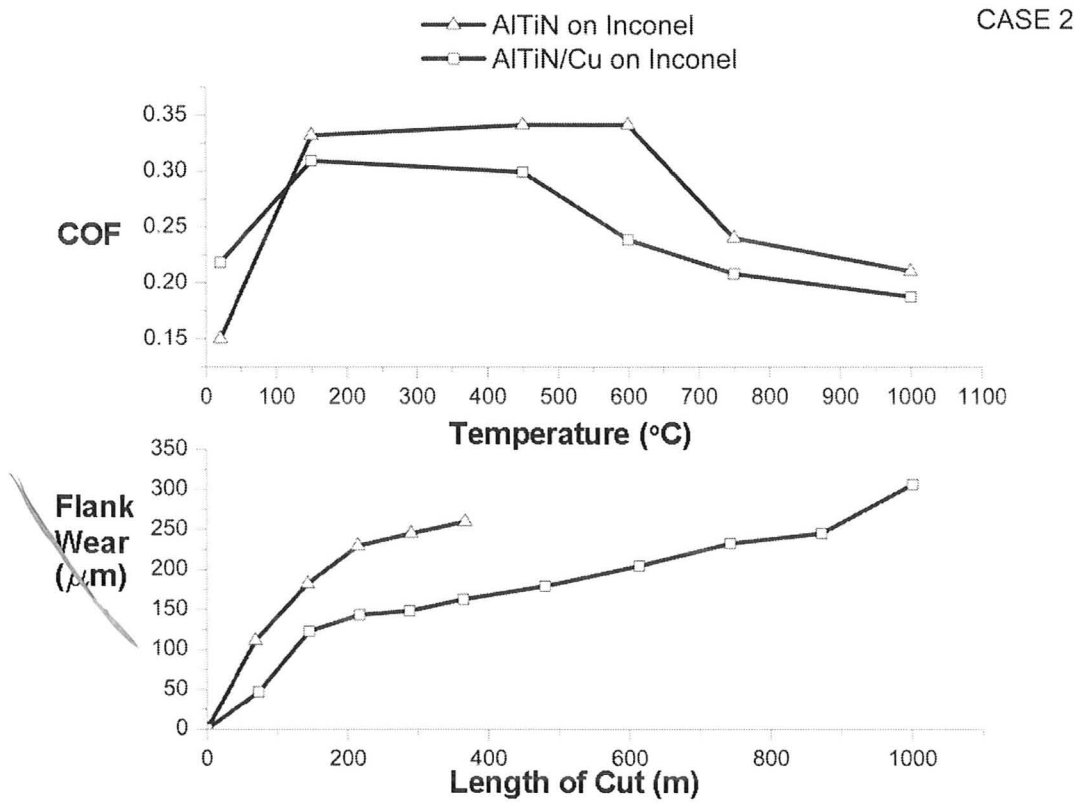

Figure 2.47: Shuster Case 2

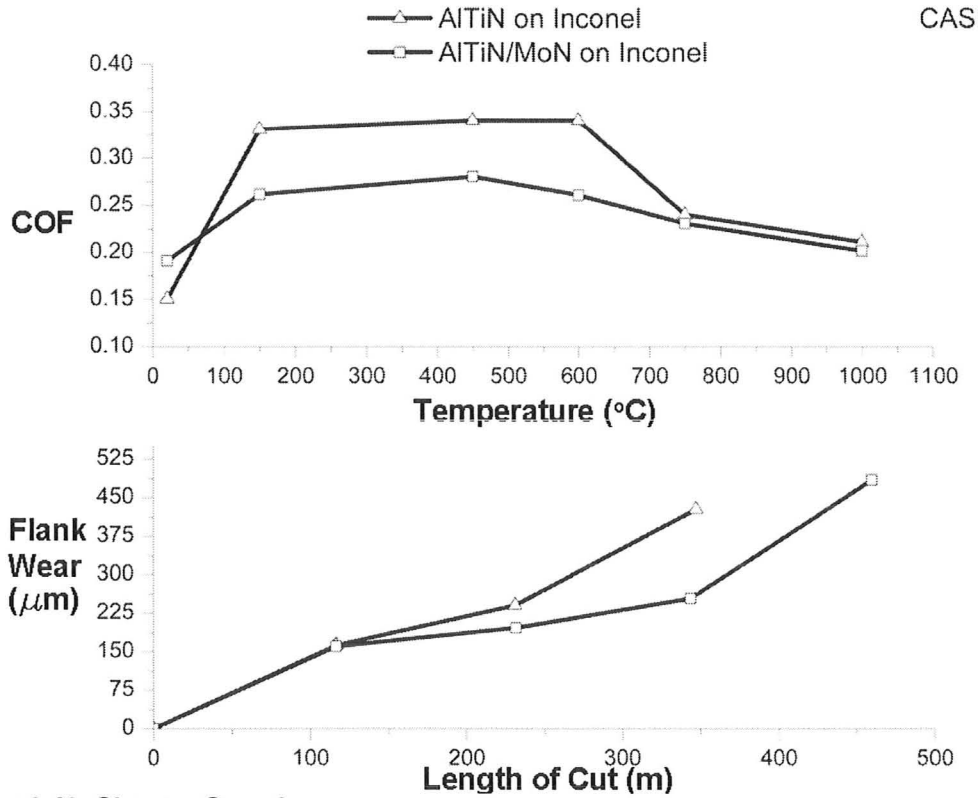

Figure 2.48: Shuster Case 3

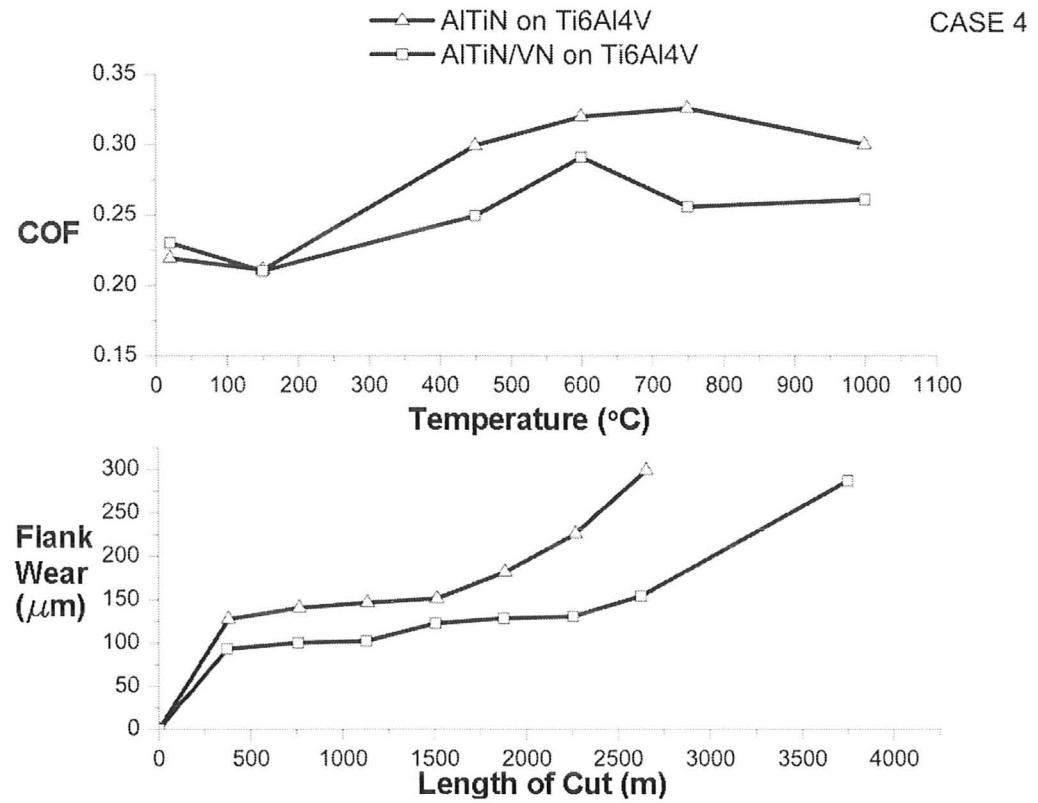

Figure 2.49: Shuster Case 4

Thus as an estimate, the COF in such a setup should fall in the range of 0.2 to 0.35 based on Shuster's work. It is expected that uncoated pins for each setup will have a higher COF than a properly selected coated pin.

A search for an appropriate tribometer to replicate these tests yielded no commercially available units. Thus crucial components of the unit were purchased individually from various suppliers and constructed and tuned within the MMRI as the majority portion of this thesis work.

Our goal was to use the prior work of Shaw and Shuster to take the positive design aspects and meld them into our own unique design. It is worth noting one recent test before moving on. While not based exactly on Shaw and Shuster's setup, another approach taken by Brocail et al. from France in 2010 and published in the International Journal of Machine Tools and Manufacture used a V-block to hold a workpiece specimen (AISI 1045 steel) and using 1 GPa of normal stress rolled a circular disk of tooling material (uncoated tungsten carbide) against a stationary workpiece. An induction heater was used to simulate high temperatures up to around 1000°C. From their studies, they found the following empirical friction relationship for COF (Brocail, Watremez and Dubar 2010, 1-31).

$$\mu = 0.919\sigma^{-0.251}V^{-0.463}T_{int}^{0.480} \qquad \text{Equation 2.51}$$

Here σ is the normal stress, V is the velocity and T_{int} is the interface temperature. Under high plastic stress, increasing the normal stress decreases COF as expected. Also COF was found to be directly proportional to temperature with temperature having a stronger effect than the normal stress. This agrees with

theory and Shuster's experiments. Thus significant emphasis was placed on temperature control as it is the most significant and difficult variable to measure/control.

2.4.4 Limitations of Modified Brinell Hardness Testing for Metal Cutting

The modified Brinell hardness tests simulate important aspects of metal cutting but do not capture all aspects of metal cutting. These modified Brinell simulations have the following limitations:

- This test has no shear plane to induce temperature and we are applying the heat externally. The temperature gradients will differ from machining. Also there is no rake angle or clearance angle to simulate.
- There is no simulation of the shear and strain rates in metal cutting.
- This test does not simulate run in and exit of cut. Also it does not simulate depth of cut, feed rate, width of cut or the dynamic aspects of metal cutting such as chatter.
- With the tribometer we have no knowledge of chip contact length, microcrack formation, chip compression ratio or cutting forces.
- The geometry of the parts are different than metal cutting (i.e. no cutting edge radius or nose radius).
- Shaw notes that chip curl and flow cannot generally be predicted by a bench scale test (M. C. Shaw 2005, 300).

While the tribometer may show increased or decreased COF there is no guarantee this will also show up in real metal cutting. In general we use the COF

as an indicator or filter. It allows a possibility to predict wear but the COF is just one element of machining, albeit an important element.

2.4.5 Coefficient of Friction for Modified Brinell Hardness Tests

Two cases will be discussed. Case 1 follows Brinell hardness theory and replicates the work of Shaw, Shuster and Schey and should be selected as the primary test to replicate adhesive metal cutting conditions under subsurface plastic flow. Case 2 is the reversal of the materials with the pin being the workpiece material and the disk being the tooling material. Due to the difficulty and cost in forming a spherical tipped pin in some cases (i.e. CBN, Diamond, and Ceramics), Case 1 is not always possible. Case 2 does not follow the method used in Brinell hardness testing nor does it create the same form of subsurface plastic flow as the pin deforms against the hard disk and makes a circular wear pattern with no indentation in the disk. Case 2 cannot generate high enough stresses (1-3GPa) as the pins will more than likely buckle or catastrophically fail. Also the deformation of the pin will vary in Case 2 making the contact area a variable. This will likely lower test repeatability. This deformation may cause vibration and/or damage to a sensor. Two preliminary cases with CBN and Diamond disks were tested against cast iron and titanium pins respectively using Case 2 and were found to correlate well with the results of machining tests. Lower loads (i.e. 500N) were used for safety. These 2 cases appeared to be strongly governed by tribofilms, diffusion and coatings which may explain why this arrangement was successful. Case 2 testing will not be elaborated on further but the reader should be aware of the concept. The derivation of COF for both cases will be outlined separately. It

should be noted that a paper from Rice and Wayne showed that specimen reversal (i.e. switching the pin and disk) does in some cases change the result so caution should be used in interpreting Case 2 results. In the paper titled *Specimen Material Reversal in Pin-on-Disc Tribotesting* it was the author's conclusions that the chemical reaction and flow of material due to hardness differences when switching the specimens can change the results (Rice and Wayne 1983, 85-92).

Case 1:
Hemisphere print on disk

Case 2:
Circular wear track on disk.
No imprint

Figure 2.50: Illustration of Case 1 and Case 2 Tests

Case 1

The coefficient of friction calculation for this test is derived from first principles in this section. Based on the literature, there are 2 types of the Case 1 modified Brinell hardness test. The first, by Shaw is a single point Brinell hardness test and may be considered the traditional Brinell hardness test. Shuster uses two contact points (each assumed relatively the same) and as a result Shuster's derivation of COF includes a factor of 2 in his equation.

The work of Shaw measured the normal stress and the frictional torque but did not explicitly derive an equation for coefficient of friction. Shuster on the other hand stated the final equation for COF for a 2 point contact modified Brinell hardness test but provided minimal background derivation. Thus, as part of this literature review, the derivation will be completed from first principles for 1 and 2

points of contacts. Shuster's equation is below and has been verified through personal conversation with Dr.German Fox-Rabinovich and 2 separate journal paper's translated from Russian to English based on Shuster's experiments (Shuster L.S 1997, 57-60) and Lyapin's (Lyapin 1969, 36-40).

$$\mu_{shuster} = \frac{3M}{4F_N R_{IND}} \qquad \text{Equation 2.52}$$

Here M is the torque moment applied to the pin from friction, F_N is the normal load and R_{IND} is the outer radius of the indentation print on the disk material. It is assumed that R_{IND} is the same for both of the disks in Shuster's experiment. R_{IND} is the linear distance (essentially d/2) from the outer edge of the indentation to the centre of the indentation. The side flow or lip on the indentation is exaggerated in Figure 2.51 to show where the measurement should be taken from.

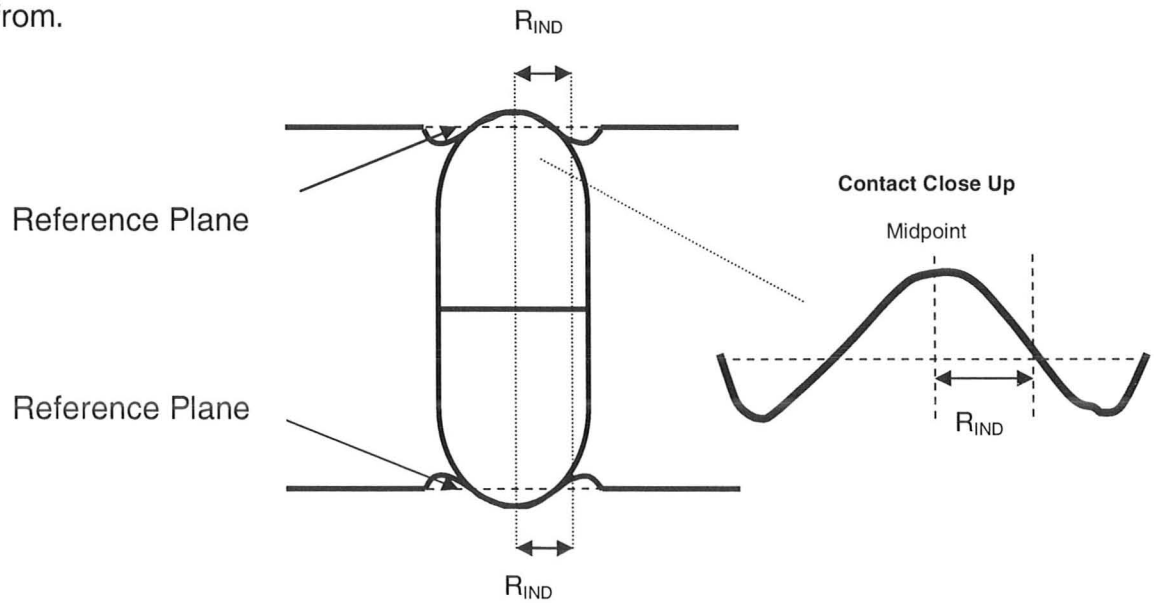

Figure 2.51: Illustration of the Contact Points in Shuster's Experiments

First it is assumed that the friction shear stress, τ, throughout the contact area and tangential to the normal load, F_N, can be represented by a single average

value, τ_{AVG}. Thus at any particular point on the contact area of the pin to the disk, the frictional force, F_F, is equal to the following, assuming an infinitesimal real area of contact, dA:

$$dF_F = \tau_{AVG}\, dA \qquad \text{Equation 2.53}$$

The next step in the derivation was to relate the torque measurement to the average frictional shear stress, τ_{AVG}. Setting up a spherical coordinate system is most convenient to solve this problem since the indentation is from a hemisphere. Here ψ is the radial angle in the XY plane and Θ is the angle from the Z-axis to the XY-plane. This is illustrated in Figure 2.52.

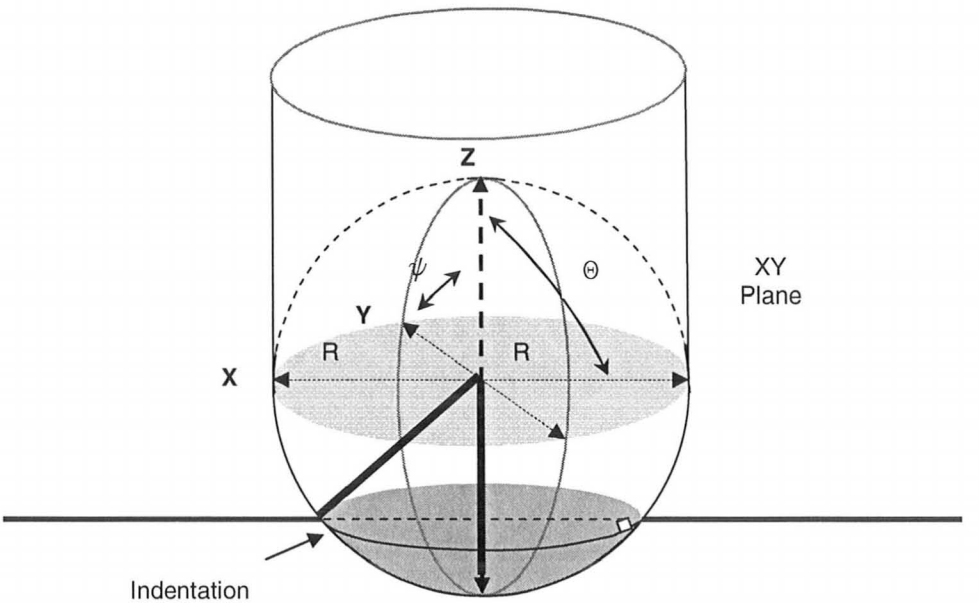

Figure 2.52: Spherical Coordinate System for Single Point Modified Brinell Hardness Test

If constant rotational speed is achieved, the applied torque of the motor must equal the frictional reaction torque in order for the steady state net force to

total 0. The easiest way to visualize the derivation is to look at an infinitesimal slice from the indentation surface.

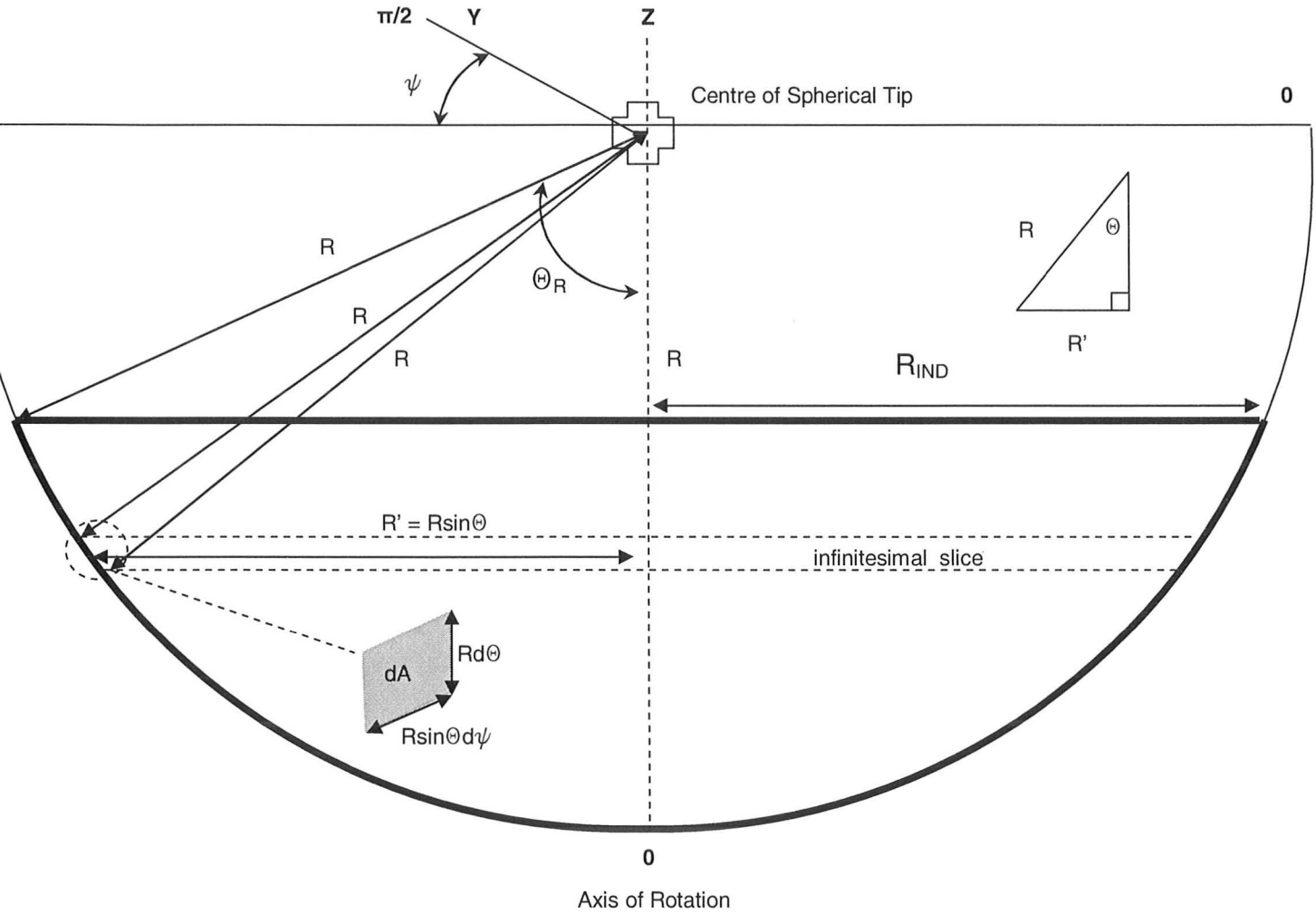

Figure 2.53: Close-up View of the Indentation Coordinate System

R is the radius of the pin in these calculations and R_{IND} is the outer indentation radius. Thus, $dA = R^2 \sin\Theta d\psi d\Theta$. As a result the integration of the angle Θ with respect to the Z-axis takes place from 0 to Θ_R as illustrated. A simple sketch in Figure 2.54 shows this more clearly.

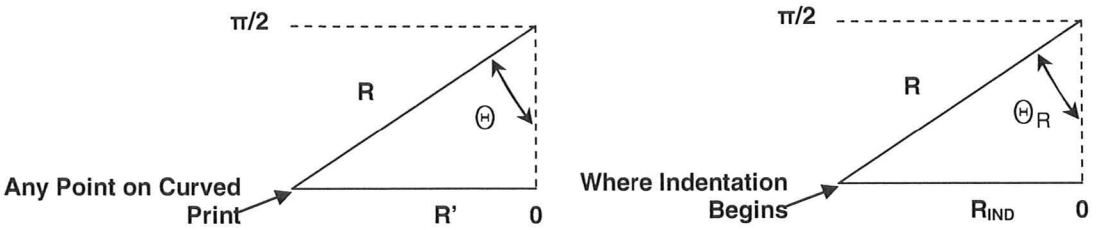

Figure 2.54: Definition of the Indentation Angle Θ and Θ_R

Where the edge begins, R' = R_{IND}. Also R'= RSinΘ holds true for any point along the curve indentation surface. Now the moment, M and shear stress, τ_{AVG} relationship can be derived (Note that, dM = R'dF and dF = τ_{AVG}dA). Thus, for a single point Brinell contact (note all angles are in radians):

$$M_1 = \int_0^{\Theta_R}\int_0^{2\pi} R'\tau_{AVG}R^2 \sin\Theta d\psi d\Theta \qquad \text{Equation 2.54}$$

M_1 represents 1 contact point of the pin. Making the substitution that R' = RSinΘ:

$$M_1 = \int_0^{\Theta_R}\int_0^{2\pi} \tau_{AVG}R^3 \sin^2\Theta d\psi d\Theta \qquad \text{Equation 2.55}$$

$$M_1 = 2\pi R^3\tau_{AVG}\int_0^{\Theta_R} \sin^2\Theta d\Theta \qquad \text{Equation 2.56}$$

The exact solution to this equation is:

$$M_1 = \pi R^3\tau_{AVG}(\Theta_R - \sin\Theta_R\cos\Theta_R) \qquad \text{Equation 2.57}$$

By making the assumption that $Sin\Theta \approx \Theta$ this exact solution can be simplified.

MMRI testing typically yields the following (to be shown in detail later):

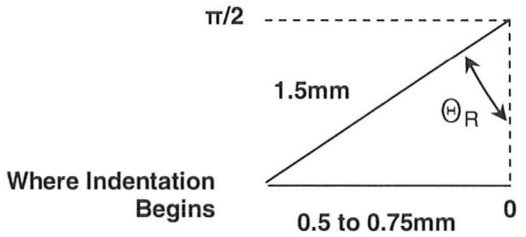

Figure 2.55: Illustration of Typical Dimensions Seen in MMRI Testing

Where the indentation begins, R_{IND} is typically equal to about 0.5mm to 0.75mm for a 3mm pin with 1900N load. As a result Θ_R varies from $Sin^{-1}(1/3)$ to $Sin^{-1}(1/2)$ or 0.34 radians (19.5°) to 0.52 radians (30°). If Equation 2.56 makes this $Sin\Theta \approx \Theta$ substitution, this leads to the following integral:

$$M_1 \approx 2\pi R^3 \tau_{AVG} \int_0^{\Theta_R} \Theta^2 d\Theta \qquad \text{Equation 2.58}$$

Using the relationship, $R_{IND} = R\, sin\Theta_R \rightarrow \Theta_R \approx R_{IND}/R$:

$$M_1 \approx \frac{2}{3}\pi R^3 \tau_{AVG} \Theta_R^3 \qquad \text{Equation 2.59}$$

$$M_1 \approx \frac{2}{3}\pi R_{IND}^3 \tau_{AVG} \qquad \text{Equation 2.60}$$

Table 2.8: Comparison of Angular Assumption in Derivation of COF

Θ_R Degrees)	R_{IND} (mm)	$Value\ of\ \frac{2}{3}\pi R_{IND}^3 \tau_{AVG}$	$Value\ of\ \pi R^3 \tau_{AVG}(\Theta_R - sin\Theta_R cos\Theta_R)$	% Error Using Exact Solution As Base
0	0	0	0	-
5	0.13	$0.0047\tau_{AVG}$	$0.0047\tau_{AVG}$	0%
10	0.26	$0.0370\tau_{AVG}$	$0.0374\tau_{AVG}$	-0.91%
15	0.39	$0.1226\tau_{AVG}$	$0.1251\tau_{AVG}$	-2.04%
20	0.51	$0.2828\tau_{AVG}$	$0.2934\tau_{AVG}$	-3.61%
25	0.63	$0.5336\tau_{AVG}$	$0.5652\tau_{AVG}$	-5.61%
30	0.75	$0.8836\tau_{AVG}$	$0.9605\tau_{AVG}$	-8.01%

As a result the approximate solution will be taken as the method used for the calculation of COF. Its implementation is simpler and a more convenient form

to work with. Since the work involves assumptions to being with, this small error should not make a large difference. Taking into account that Shuster's design uses two points of contact, Shuster's value for the moment, M_2 to cause this shear stress is greater than the value calculated in Equation 2.60 by 2 times. As a result, $M_2 = 2M_1$. Thus

$$M_2 \approx \frac{4}{3}\pi R_{IND}^3 \tau_{AVG} \qquad \text{Equation 2.61}$$

Rearranging this equation, to find the value of τ_{AVG}

$$\tau_{AVG} \approx \frac{3M_2}{4\pi R_{IND}^3} \qquad \text{Equation 2.62}$$

Taking into account that FEA studies as well as literature studies show that the normal stress profile is near constant for such a setup, the normal stress in Shuster's design is calculated as follows using the projected Meyer area as the area of contact:

$$A_{Proj} = \pi \mathrm{R}_{\mathrm{IND}}^2 \qquad \text{Equation 2.63}$$

The numerator and denominator are then multiplied by 2 because there are two surfaces. However the values divide out.

$$\sigma = \frac{2F_N}{2A_{Proj}} \qquad \text{Equation 2.64}$$

$$\sigma = \frac{F_N}{\pi \mathrm{R}_{\mathrm{IND}}^2} \qquad \text{Equation 2.65}$$

$$\mu = \frac{\tau_{AVG}}{\sigma} \qquad \text{Equation 2.66}$$

$$\mu = \frac{\frac{3M_2}{4\pi R_{IND}^3}}{\frac{F_N}{\pi \mathrm{R}_{\mathrm{IND}}^2}} \qquad \text{Equation 2.67}$$

$$\mu = \frac{3M_2}{4F_N R_{IND}} \qquad \text{Equation 2.68}$$

This is same solution as Shuster listed originally in Equation 2.52 where M_2 is the same as M. Thus we can be confident of the assumptions and work Shuster completed for calculating COF. The two final equations are contrasted below (Shuster = 2 contact points and MMRI = 1 contact point):

$$\mu_{Shuster} = \frac{3M_{TOT}}{4F_N R_{IND}} \qquad \text{Equation 2.69}$$

$$\mu_{MMRI} = \frac{3M_{TOT}}{2F_N R_{IND}} \qquad \text{Equation 2.70}$$

In the case of the MMRI solution, $M_{TOT} = f$ (Temperature, Materials, Normal Load, Coatings, Velocity). Note the velocity effect is extremely weak for the MMRI setup.

Case 2

It needs to be reiterated that this case does not produce subsurface plastic flow nor does it conform to Brinell standards. It is not the desirable test setup but rather an additional analysis tool if the pin cannot be made of the harder material easily. For this case, the wear track was found to be circular during preliminary testing. This setup is a circular scratch not an indent on the disk. As a result a polar coordinates approach is used as shown in Figure 2.56. This derivation will be shown for only one contact point.

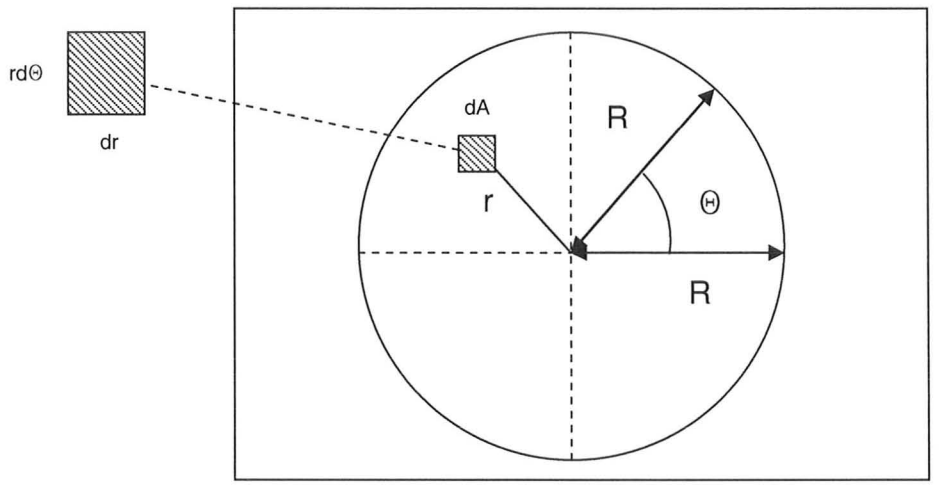

Figure 2.56: Illustration of Case 2 Coordinate System

Assuming that an average frictional shear stress applies on an infinitesimal area noted above, the following equation applies for a single point contact:

$$dF_F = \tau_{AVG}\, dA \qquad \text{Equation 2.71}$$

$$M_1 = \int_0^R \int_0^{2\pi} r\, \tau_{AVG}\, dA \qquad \text{Equation 2.72}$$

$$M_1 = \int_0^R \int_0^{2\pi} \tau_{AVG}\, r^2 d\Theta dr \qquad \text{Equation 2.73}$$

$$M_1 = \int_0^R 2\pi\, \tau_{AVG}\, r^2 dr \qquad \text{Equation 2.74}$$

$$M_1 = \frac{2\pi \tau_{AVG}\, R^3}{3} \qquad \text{Equation 2.75}$$

Note this is the same result for M_1 as with the hemispherical impression in Case 1 using an approximation. As the spherical impression in Case 1 is typically very shallow (noted from experiments) it makes intuitive sense that the results for

Case 1 and Case 2 should be very similar. As a result, since the projected contact stress is the same as in Case 1, the final result for Case 2 becomes the same:

$$\mu_{MMRI,CASE\ 2} = \frac{3M_{TOT}}{2F_N R_{IND}} \qquad \text{Equation 2.76}$$

This exact result was published by Pytel and Kiusalaas in 1994 using a similar approach (Pytel and Kiusalaas 1994, 346-347). This adds confidence to both the Case 1 and Case 2 results. Thus regardless of the testing, the equation for COF is approximated as the same.

Chapter 3. Experimental Design

The following photo contains the complete experimental design. Each element will be discussed in detail.

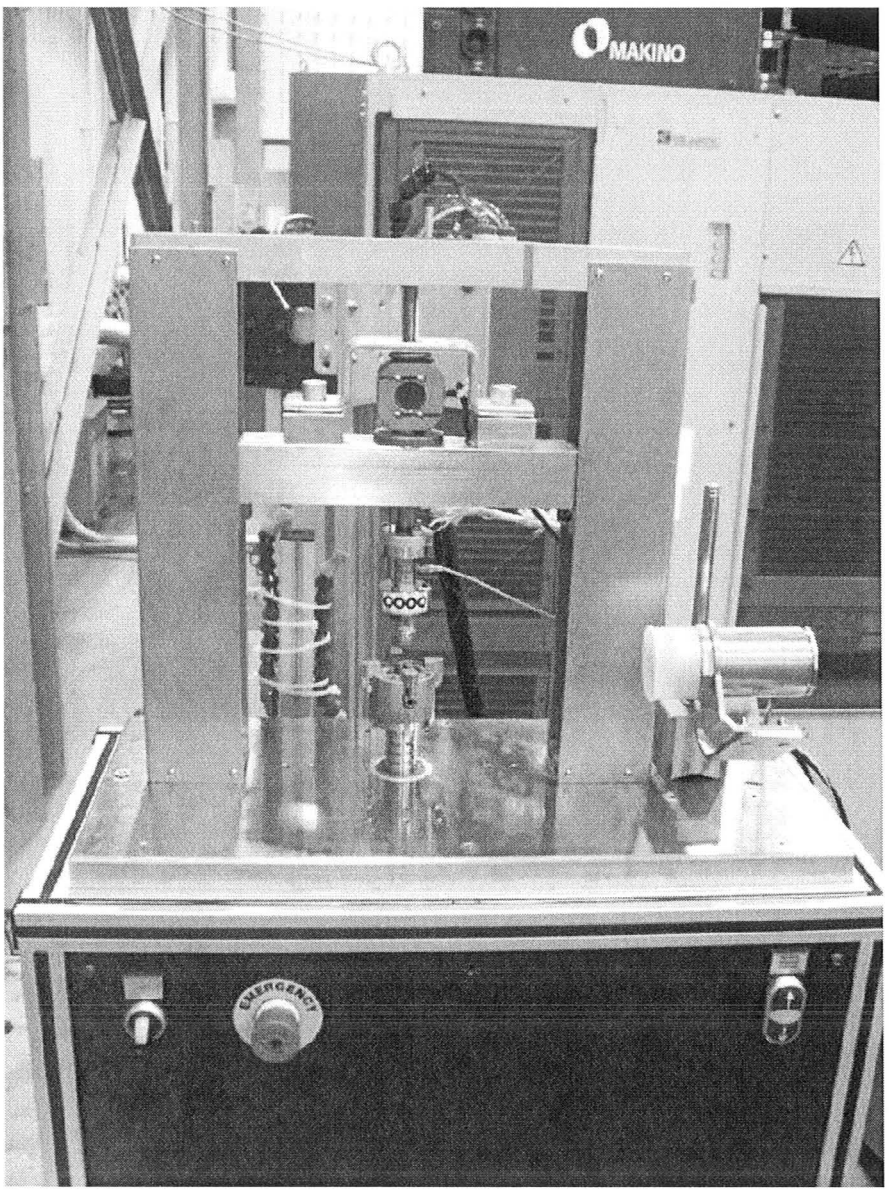

Figure 3.1: Overall View of the MMRI Tribometer for Modified Brinell Hardness Testing

The unit contains an upper and lower limit switch which prevents damage (obscured from view). The MMRI design is also sketched in Figure 3.1.

MMRI Design

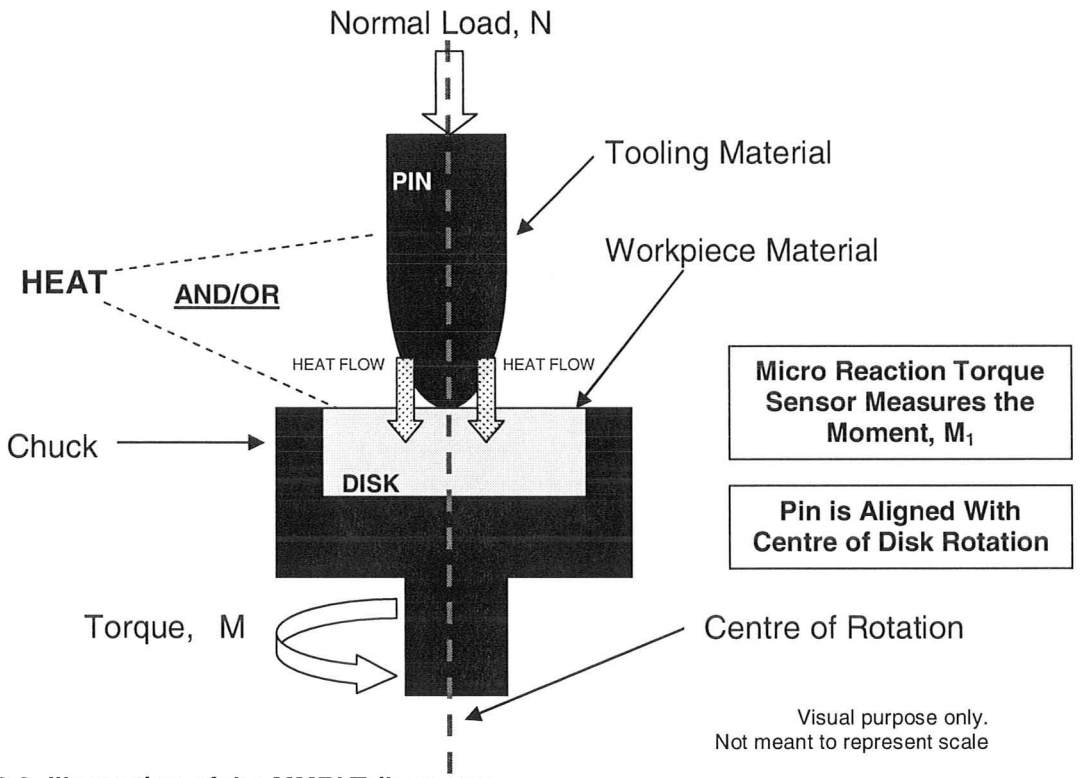

Figure 3.2: Illustration of the MMRI Tribometer

This design is now compared and contrasted to the setups of Shuster and Shaw.

Design Similarities to Shaw:

- Both designs operate with a spherical tipped pin which is made of the tooling material. Also the designs use the disk as the workpiece material.
- The pin is on the centre of rotation with the interface having near zero velocity.
- Normal stresses are around 1 GPa or higher.

Design Differences to Shaw:

- Shaw does not provide heat to get the interface temperature up to 1000°C.
- Shaw did not test multifunctional coatings as they were not developed sufficiently in the 1960s.

- Shaw did not have closed loop controllers.

Design Similarities to Shuster:

- Both designs operate with a spherical tipped pin which is made of the tooling material. Also the designs use the disk as the workpiece material.
- Both designs have a high normal stresses from 1-3GPa and use external heating to get the interface to 1000°C.
- Both designs test multifunctional coatings developed within the last 10 years.

Design Differences to Shuster:

- Shuster uses two identical points of contact with the same pin (assume both imprints in the disks are the same) while the MMRI uses one point of contact.
- Shuster does not use closed loop controllers while the MMRI does.
- Shuster uses a thermocouple to measure temperature and the MMRI uses a pyrometer.
- Shuster rotates the pin rather than the disk which reduces alignment issues. The MMRI test setup rotates the disk which requires accurate setup of the pin.

As a result each setup has its advantages and disadvantages. However, the MMRI solution has designed in most of the positive aspects of Shaw and Shuster and attempted to improve them.

3.1 Design Frame

The photos in Figure 3.3 and Figure 3.4 are of the design frame and components purchased from Nanovea®. The unit came with electronics and computer software to control motion. Heating, temperature controllers and torque measurement devices were purchased from different suppliers and integrated.

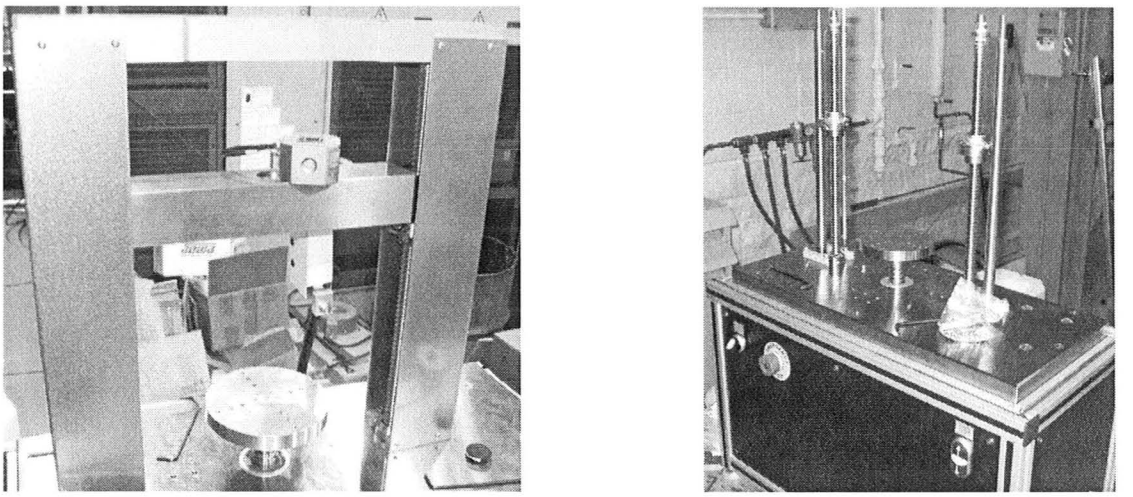

Figure 3.3: MMRI Design Frame (External)

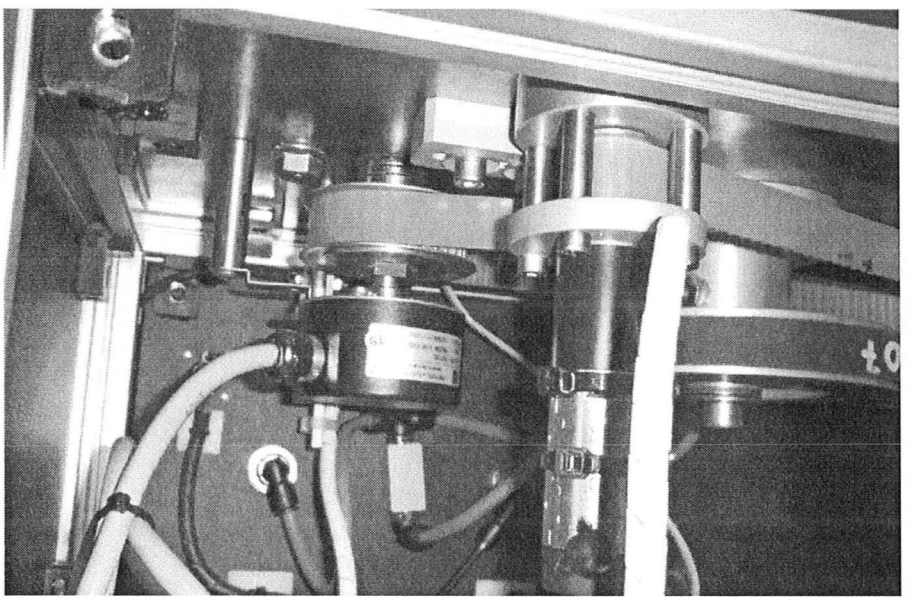

Figure 3.4: MMRI Design Frame (Internal)

The unit also came with a central rotating column capable of 0 to 1000RPM rotation. This motion was closed loop with encoder feedback and adjustable via computer software. An optical tachometer was used to verify the RPM correct within 5% for the entire operating range. An independent 4 jaw chuck was added to easily grip disk specimens. The chuck was coated with TiN to prevent any rusting. Typically in a machine shop setting a part will be oiled however in a test where lubrication or contamination control is a serious issue, oil was avoided and substituted for a rust inhibitor coating.

Figure 3.5: Chuck and Spindle Motor

3.2 Pin Design

The pin was designed as a hemispherical pin to conform to Brinell hardness testing, aid the run in process, avoid vibration and result in a point contact. As mentioned, the ASTM standards for Brinell hardness testing stated that for a 2.5mm diameter sphere, 1839N is recommended to achieve full plasticity on specimens with workpiece materials such as Titanium and Inconel 718. Thus, the design was selected to have 2000N of load and a 3mm pin design. Using the range of print prints (R_{IND} from 0.5 to 0.75mm) found from experimentation and the

2000N load, the following calculations were carried out in Equation 3.1 and Equation 3.2.

Using 1.5mm as the print diameter, the mean compressive stress is

$$\sigma_{min} = \frac{2000N}{\pi(0.00075m)^2} = 1.13\ GPa \qquad \text{Equation 3.1}$$

Using 1mm as the print diameter, the mean compressive stress is

$$\sigma_{max} = \frac{2000N}{\pi(0.00050m)^2} = 2.55\ GPa \qquad \text{Equation 3.2}$$

These stresses are consistent with the 1-3GPa range required for simulating machining stresses and they agree with Brinell hardness testing print sizes for full plasticity. The pin was designed to have a hemisphere on both sides to have 2 usable sides (i.e. reusability). All pins for this test were made of tungsten carbide with 6% cobalt binder and a 0.8 micron grain size with 92.5 Rockwell C hardness. They were manufactured from Canada Carbide® in Woodbridge, Ontario. This grade of tungsten carbide is the same as that commonly used for tooling inserts in the MMRI (Kennametal K313). The pins were designed to be 35mm long from tip to tip. This was to ensure adequate space for heating devices as will be seen later and to provide enough material for a collet to grip. The length was kept to a minimum to increase stiffness to avoid catastrophic compressive buckling under the high loads and temperatures. This length calculation was estimated based on the transverse rupture strength of tungsten carbide which is commonly listed. As mentioned an advantage to this pin design is that a point is isolated to study friction. This advantage is illustrated in Figure 3.6.

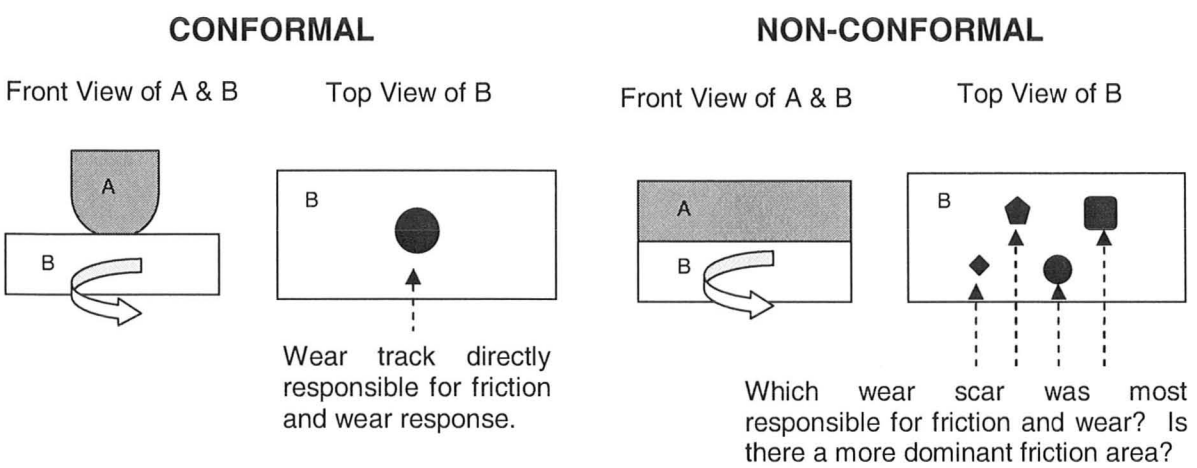

Figure 3.6: Illustration of the Advantages of a Non-Conformal Pin Test Setup

This design does have the disadvantage of cost. To make these pins with high precision costs about $50 per pin depending on the manufacturer. 25 pins were initially purchased at a lower introductory cost. However these pins have been shown to be useful for several tests because tungsten carbide is a strong and robust material. If several coatings need to be applied, upwards of 25 pins could be required for a single batch of testing which could run upwards of $600 to $1250. Canada Carbide's® pins were verified to be within tight dimensional tolerances and showed excellent surface finish. This cost issue also exists for HSS pins. The recommendations sections will discuss this issue in further detail. A sketch of the overall pin design is shown Figure 3.7.

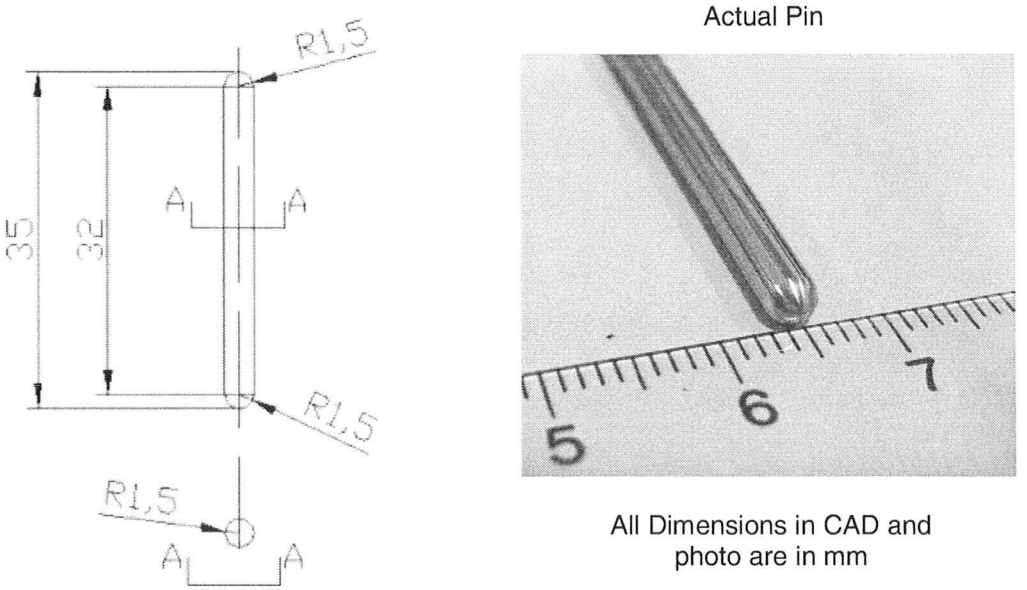

Figure 3.7: Overall 3mm Pin Design

Using this pin design, the velocity at the interface can be estimated as follows using 1 RPM disk rotation on centre (test standard) and a 1-1.5mm diameter print:

$$V_{min} = \frac{1\,Rev}{min} x \frac{\pi(0.001m)}{Rev} x \frac{1\,min}{60s} \approx 0.00005m/s \quad \text{Equation 3.3}$$

$$V_{max} = \frac{1\,Rev}{min} x \frac{\pi(0.0015m)}{Rev} x \frac{1\,min}{60s} \approx 0.00008m/s \quad \text{Equation 3.4}$$

Thus the near zero or near seizure conditions are simulated as these are extremely small velocities.

3.3 Disk Design

The disk design revolves around 2 key points:

1) The disk must be flat, i.e. the opposing surfaces are parallel and are ground to a maximum R_a of about 0.8 microns. The shape of the disk is not that critical however the disk should have edges that will fit well into a ceramic V-block that was manufactured to protect the chuck and heat the interface more efficiently.

2) The disk must be a minimum of 5mm thick and a maximum of 8mm thick. The length and width of the disk must not exceed about 10mm. Thus an approximate volume of the disk should be about 500 to 800mm^3. From extensive experimentation the disk must be small to get temperatures above 500°C in an open room temperature environment.

This small disk size is an advantage in that only minimal material is required. Using these disk size requirements, about 4 or 5 tests can be completed before the surface needs re-finishing. After testing the disk surface it can be reground to remove damaged material and regenerate the desired surface finish. It should be noted that due to the small size, gripping the specimens in the grinder may be difficult. Thus for the first set of trials, take a large piece of disk, grind the surfaces parallel and then cut the specimens to small pieces using a diamond saw, water jet cutting or some other appropriate cutting method.

3.4 Central Column

The central column contains the pin that is loaded into the disk. This column must centre the pin on the axis of the rotation of the disk. This column must be stiff and have adjustment for alignment. It must also contain the load cell, the torque measurement sensor (connected to static pin) and a temperature control component. This central column is essentially the nucleus of the design as it contains all the significant controlling and measurement components. These items will be addressed from top to bottom of the central column as listed:

- Load Cell
- Splined Shaft and Crosshead

- Reaction Torque Sensor
- Vortex Chilling Unit and Air Line Design
- Pin Collet
- Induction Coil and Temperature Controller
- Disk Chuck Design

3.4.1 Load Cell

The load cell provided by Nanovea® with the design frame is a strain gauge with a range of 0-3000N (However software only permits loads up to 2000N as a safety factor). The desired load is input in the computer software provided and a PID control loop controls the motion of the crosshead to achieve the desired force. Compliance was added to the force loop through the use of a bevel washer (metal and polymer hybrid), bracket and linear splined shaft to add finer load control. Currently the unit is repeatable and offers fine control within +/- 3N across the 2000N range. The bevel washers are removable and interchangeable depending on the load control desired.

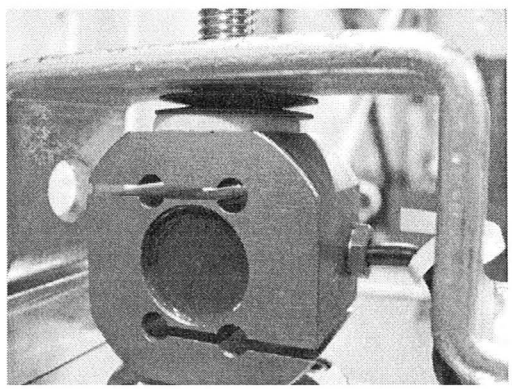

Figure 3.8: Load Cell Setup

At low loads the polymer bevel washer adds compliance and at high loads the steel bevel washers offer compliance. The splined shaft operates only

linearly with 30 Nm of torque resistance. By placing the load cell above the extremely stiff stainless steel crosshead vibration issues were minimized. The splined shaft sits in a bearing within the crosshead and is attached with a flange.

The load cell was calibrated by Nanovea®. To confirm the accuracy of this sensor, a calibration was completed using a 9121 Kister® dynamometer in the MMRI. The Kistler® dynamometer was a 3 component unit (F_x, F_y and F_z) rated for +/-3kN (compression/tension) loads in the $F_{x,y}$ directions and +/-6kN (compression/tension) in the F_z in directions. The F_z direction was chosen because the F_z direction on the dynamometer is sensitive to a vertical load whereas F_x and F_y measure force due to shear. It was thought that the shearing effect may be less accurate than the pure vertical load despite the fact that the F_x and F_y directions are closer to the force range in question. Furthermore the F_z direction was the most stable mechanical setup for the dynamometer. The Kistler® dynamometer was independently calibrated using an E-Z Weigh® scale which could handle up to 2000N load. Weights were stacked on the E-Z Weigh® scale, measured and then stacked on the Kistler® dynamometer to measure how close the values were. Up to about 750N was tested using the E-Z weigh scale. The Kistler® dynamometer agreed within a few Newton's across the entire range indicating that the Kistler® dynamometer was functioning and calibrated properly. For setup of the Kistler® amplifier, the gain was set appropriately so that approximately 5V of the 0-10V output range was used for each test. This ensured safety of overloading the amplifier and operating in the so-called "sweet spot" of the sensor. The following forces were selected for the Nanovea® strain gauge

sensor to calibrate against the Kistler® dynamometer: 10N, 50N, 100N, 250N, 500N, 750N, 1000N, 1250N, 1500N and 1800N. Each test was done 3 times to test for repeatability. As a result 30 test points were collected across the 0-1800N range. Table 3.1 and Figure 3.10 illustrate a high level of agreement between the strain gauge and the Kistler® dynamometer. This indicated that the Nanovea® strain-gauge sensor was well calibrated and is capable of accurate and repeatable results. In addition to this load calibration, a static indentation test was made under Brinell conditions for a Ti6Al4V disk. Using the microscope and white light laser interferometer the Brinell HB number was calculated. The calculated HB value for Ti6Al4V indicated only 5% deviation from the listed theoretical value, thus adding further confirmation to the accuracy of the strain gauge load cell and the controller.

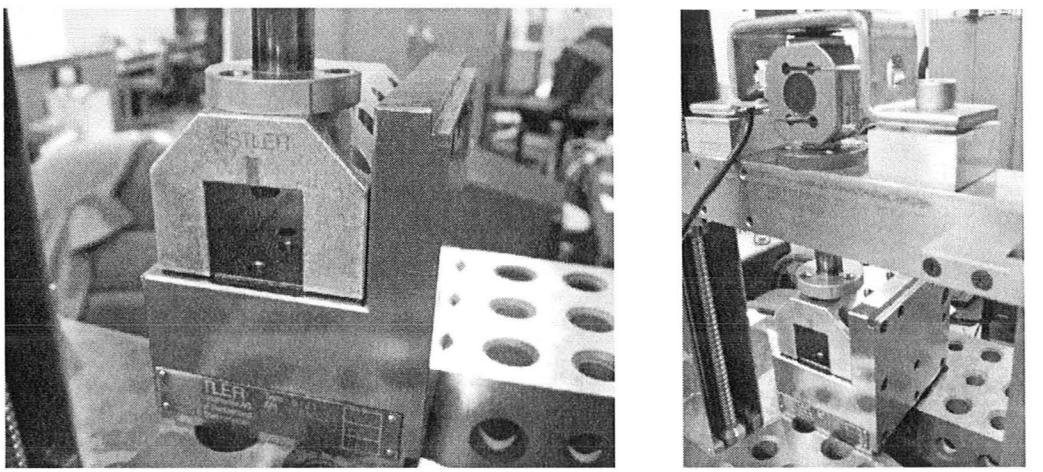

Figure 3.9: Load Cell Calibration on Tribometer

Table 3.1: Vertical Load Cell Calibration Data.

Set Point Load (N)	3 Trial Nanovea Average Load (N)	3 Trial Average Kistler® Load (N)	Curve Fit Load (N)	% Error (Kistler® Average As Base)
10	10.05	14.37	15.57	8.31%
50	50.53	54.91	55.71	1.47%
100	103.94	108.29	108.68	0.37%
250	251.76	255.56	255.28	-0.11%
500	501.89	504.38	503.33	-0.21%
750	751.80	752.77	751.17	-0.21%
1000	1005.20	1003.49	1002.46	-0.10%
1250	1257.51	1252.65	1252.68	0.00%
1500	1512.75	1505.26	1505.80	0.04%
1800	1811.83	1801.25	1802.40	0.06%

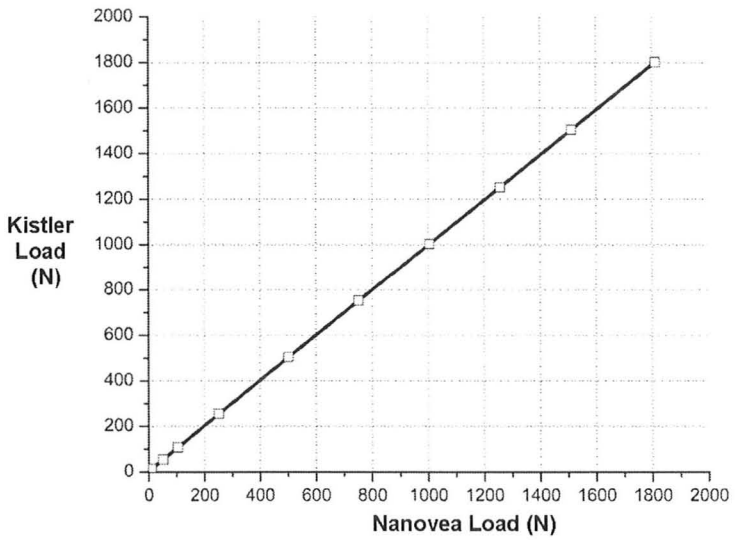

Figure 3.10: Load Cell Calibration Curve

The calibration equation is as follows:

$$F_{N,KISLTER} = 0.9917F_{N,NANOVEA} + 5.605 \qquad \text{Equation 3.5}$$

Thus the Nanovea® load cell value will be used and assumed correct.

3.4.2 Splined Shaft and Crosshead

The crosshead is made of a solid stainless steel bar that is extremely heavy and stiff. Its dimensions are 49mm deep, 42mm tall and 240mm long. This

prevents the central column from vibrating. The crosshead contains a bore with its centre aligned with the centre of rotation of the disk. The splined shaft, model LT16 from THK® with housing and flange fit into the crosshead and are attached via screws. The splined shaft is case hardened and 16mm in diameter. It is specified to withstand up to about 4000N of normal load and can withstand up to about 30Nm of torque. The top of the splined shaft is screwed into the bottom of the load cell and the bottom of the splined shaft is press fit into a steel connector for the torque sensor to be attached to. The splined shaft and connector were precision ground before and after press fitting to ensure alignment and parallelism.

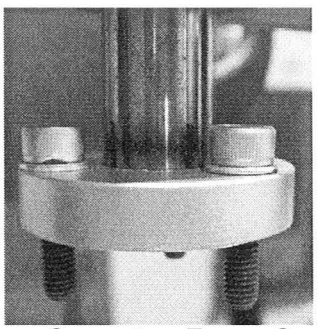

Figure 3.11: Splined Shaft Torque Sensor Connector– Torque Sensor Removed

3.4.3 Reaction Torque Sensor

The reaction torque is measured when the disk rotates against the vertically loaded static pin. Because the pin is on centre with the disk rotation, low torque is generated and as such a reliable and high resolution reaction torque sensor is required. For this application the torque sensor must be sufficiently stiff and have a natural frequency at least 4 times that of the frequency typically observed in the operation (i.e. RPM). Also there should be minimal cross talk. Furthermore the resolution should be such that there is at least 1% accuracy within a readable range (M. C. Shaw 2005, 100-101). The measurements should also be relatively

stable with time (i.e. drift), and not subject to variations in temperature and humidity within an allowable tolerance band. Also the instrument should be relatively insensitive to environmental conditions such as dust, grease and oil or any other particles in the surrounding area that could affect the calibration. Based on these requirements a Kistler® reaction torque sensor was deemed to have all of these qualities and was available in a compact size to suit this application. To determine the torque range for this sensor, the maximum torque anticipated had to be determined in order to purchase a unit with the narrowest measurement range. Typically COF for these experiments does not exceed about 0.5 based on past testing experience from Shaw and Shuster. Also the largest imprint for a 3mm pin is about 1.5mm in diameter. Doing a simple calculation, if the load is 2000N and the COF is 0.5, the friction force is 1000N. Thus, if the radial distance is 0.75mm at the max, the approximate maximum reaction torque is about 750Nmm or 0.75Nm. Thus as Kistler® offers a +/-1Nm torque sensor (Model 9329A) with 0.000005 Nm resolution (0.1 pC resolution from amplifier divided by sensitivity of 2170 pC/Nm according to Kistler®) this unit was purchased. This leaves a 0.25Nm safety factor to allow for overloading (Kistler® notes that 1Nm is the maximum reliable measurement but 1.2Nm is the threshold for damage).

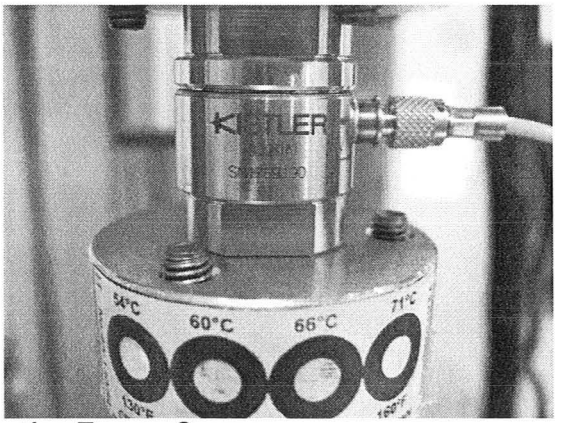

Figure 3.12: Kistler® Reaction Torque Sensor

The plate at the base of the torque sensor has a Tempil® thermal sticker matched to the maximum temperature that the sensor can take in steps. If the dots darken the heating is turned off to protect the sensor and so avoid reaching the 80°C design limit of the sensor. There are 3 connecting screws which are tightened to the top of the torque sensor. The torque sensor is dial indicated as will be explained later via the pin to ensure that it is aligned with the centre of rotation of the disk. A Kistler® charge amplifier type 5010 was used to convert the piezoelectric charge signal to a voltage. This torque sensor has the following operating characteristics:

Table 3.2: Reaction Torque Sensor Critical Specifications

Measuring Range (Nm)	+/-1
Resolution (Nm)	0.000005
Overload Range (Nm)	+/-1.2
Sensitivity (pC/Nm)	2170
Crosstalk (mNm/N)	<0.01
Maximum Compressive Load (N)	9000
Natural Frequency (kHz)	>53
Operating Temperature Range (°C)	-20 to 80

Based on discussion with a Kistler® representative this sensor was not commercially available until the end of 2003, which means that this design is relatively new and is a unique feature of this unit. The reaction torque sensor

calibration was checked in the lab with the use of a CDI torque reader, model 151LDIN with a 0 to 1.8Nm range. The CDI torque was found for the 0-0.5Nm range to match the Kistler® torque sensor within 5% deviation for 3 test replicates. A bolt was placed in the collet as shown in Figure 3.13 and the manual CDI torque gauge was turned. While watching the CDI readout, it was compared to the Kistler® readout in LabVIEW® in real-time.

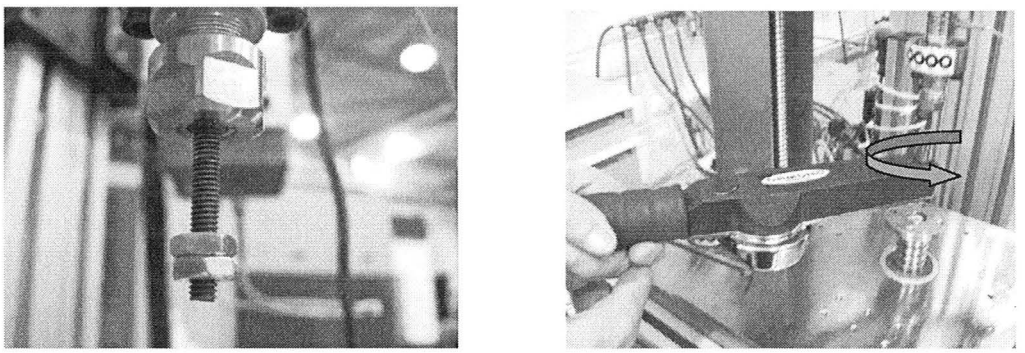

Figure 3.13: Reaction Torque Sensor Calibration

3.4.4 Vortex Chiller and Air Line Design

The entire central column was kept as short as possible to ensure stiffness and minimize propagating misalignment errors. Thus, with the pin being about 6cm from the reaction torque sensor, there are thermal issues. The reaction torque sensor cannot reach 80°C and the pin disk interface may be glowing red hot up to 1000°C. To keep the heat from reaching the sensor a vortex chilling unit was used with air directed by a short section of Loc-Line®. Together this emits cool air between 0°C and -10°C that cools the collet region near the pin. 2 additional shop air lines with Loc-Line® are adjustable and provide air placed against the reaction torque sensor to minimize thermal variation.

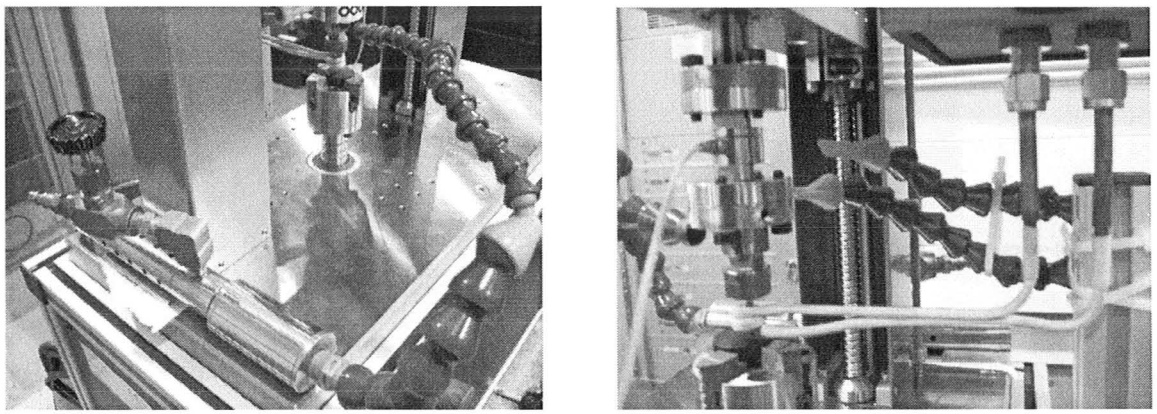

Figure 3.14: Chilling Units for the Tribometer – Vortex Chiller Left – Air Lines Right

3.4.5 Pin Collet Design

A self-centering ER11 collet from Sowa® was chosen that could hold a pin of 3-3.5mm in diameter. The collet was coated in TiN to inhibit rust and the threads required high temperature anti-seizure paste. This design is versatile in that collets can be purchased for the same holder for sizes ranging from 0.5mm to 7mm. The shank was cut down and press fit into a titanium disk. A set screw was drilled into the side of the titanium to ensure that in addition to the resistance of the press fit, the shank could not rotate. Grinding was done on all parts as a finishing process to ensure proper alignment. Titanium was selected for the components because of its low thermal conductivity (5 W/mK), compared to steels (15-20 W/mK). This then slows down the conduction of heat from the pin to the torque sensor. Along with the chilling units this was deemed the best solution to minimizing the temperature change in the torque sensor. The pin was aligned to the centre bore of the reaction torque sensor and three screws were tightened to maintain alignment. As this dial indicating process was critical it took about 4 hours to ensure that the pin was aligned to the centre of the torque sensor. Alignment

within 0.0025mm (0.0001") using a precision dial indicator was achieved. Once the 3 connecting screws were tightened they were never removed again. These screws were painted red to indicate they are not to be loosened or removed. This ensures the frictional torque measurement is accurate. Also, Kistler® states that the centre of the reaction torque sensor cannot deviate more than 0.02mm with the centre of rotation or the offset load will cause the sensor to break. To insert a new pin or replace a pin, the Kistler® and collet unit is removed from the splined shaft connector and the entire sensor and collet unit is placed on a soft and clean surface. Opposing torque wrenches adjust the collet while a LabVIEW program motors the torque in real time to ensure that it is not overloaded. The reason the unit is removed to place the pin in the collet is for safety of the Kistler® sensor. If the sensor opposing side is free then it is less likely to build up torque..

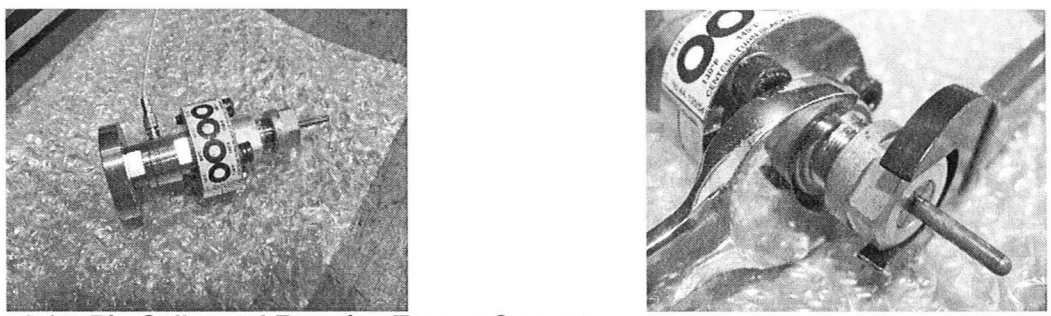

Figure 3.15: Pin Collet and Reaction Torque Sensor

Once the pin is safely in the unit, the assembly is attached to the splined shaft connector. A special dial indicator stand is attached to the chuck and the unit is moved and tightened until the pin is dialled into the centre of rotation of disk within 0.02mm. This process can take from 5-15 minutes to ensure proper alignment. This process is shown in Figure 3.16.

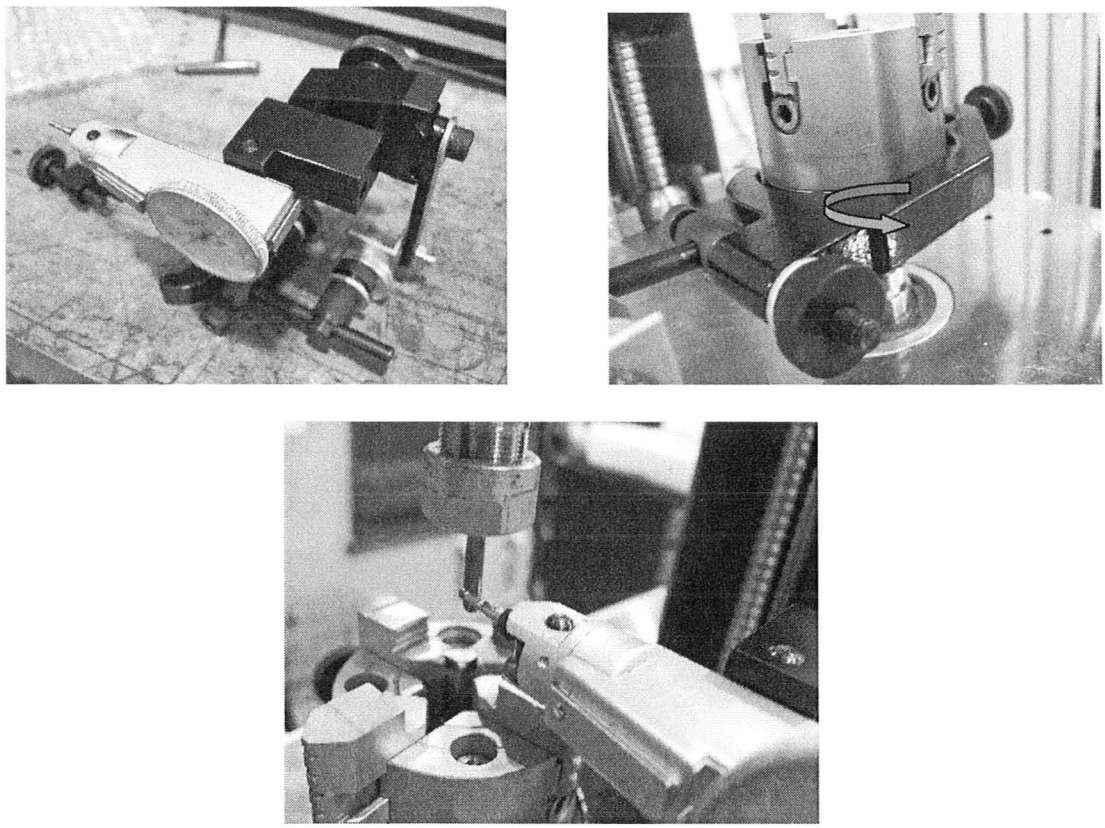

Figure 3.16: Dial Indicator Process

3.4.6 Induction Coil and Temperature Controller

An induction coil was chosen to heat the interface up to 1000°C. The unit purchased was a 1 kW unit from Ameritherm®. Initial supplier demos showed 1000°C heating was achievable on a small bench scale test performed in the MMRI and Ameritherm's laboratory. The impact the induction waves have on the torque sensor was tested and it was found to not affect the reaction torque sensor measurement. This was verified with the distributor before purchasing based on placing the coil near various sensors and monitoring the sensor signal as the heater was turned on and off. The theory for the induction heater operation was obtained from *High Frequency Induction Heating* by Frank W. Curtis (Curtis 1944). Induction heating works on eddy currents and heats by an electrical resistance

mechanism to heat metals. Induction works opposite of many heating processes. Materials with high electrical conductivity such as copper heat slowly with induction and materials with lower electrical conductivity like titanium or steel heat rapidly. Induction coils are made of copper tubes and a system circulates cooling water within the tubes to ensure that the coils themselves do not heat up. The coils are typically placed in high temperature fibreglass wrap to prevent the copper coil from directly touching the metal specimen being heated which could electrically short the system. Induction was chosen for the following reasons (Curtis 1944):

- Induction can heat to 1000°C in less than 10s which produces a similar temperature and heating rate to metal cutting.
- Induction coils are made of standard copper that can be purchased in any hardware store in various sizes and shapes and easily bent to whatever shapes are required. Solder for household plumbing is acceptable to use to join copper of various sizes.
- Induction coils allow for various heating profiles such as heating a local spot or heating a surface uniformly.
- Induction theory is well developed and induction systems come with programmable controllers which allow ramp up rates and heating profiles to be adjusted.
- Induction coils are a non-contact heating method.
- Thin copper sheets can be positioned to shield parts that an experimenter does not want to heat.

Three types of coils have been used to date: a round coil for heating the pin, a "pancake" coil for heating the disk and a hybrid pancake round coil for heating the pin and disk simultaneously. Round and pancake coils are shown in Figure 3.17. The round coil has higher efficiency (60-70% efficiency) than the pancake coil (35-50% efficiency). The key point for any coil design is that the current flow be in the same direction at all points (Curtis 1944, 66) and that the leads of the coil are close together (Curtis 1944, 54). Overall induction coil design is very much an art and several designs may need to be tested before finding the best one for an application.

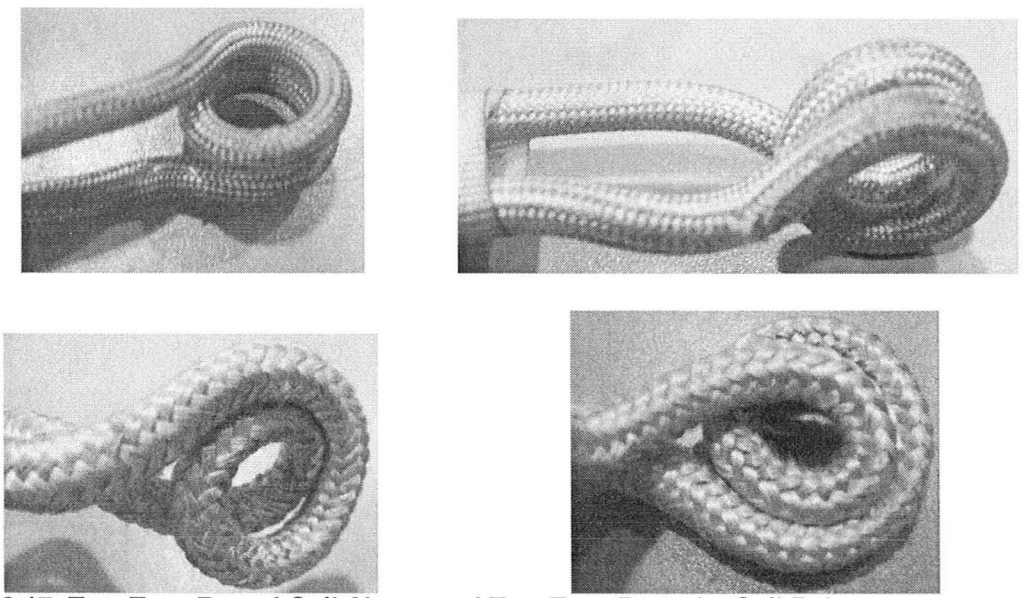

Figure 3.17: Two Turn Round Coil Above and Two Turn Pancake Coil Below

The interface temperatures were verified statically in initial trials by using a 0.25mm diameter K-type thermocouple sandwiched between the pin and disk under about 1500N of load. Two other K-type thermcouples were silver soldered 1mm and 10mm away from the interface to a dedicated tungsten carbide calibration pin to give 3 points for the temperature profile. Omega® temperature paints, Tempil® temperature stickers and a FLIR® thermal image camera were

also used to aid the calibrations. When running the tests a PIXSYS® temperature controller was used to maintain the interface temperature (to be discussed in more detail later). A closed environmental chamber was not designed due to the fact that in machining the whole environment is not a uniform temperature but rather a gradient exists. To measure and maintain the temperature during actual testing 2 options were available: 1) using a thermocouple or 2) using an infrared sensor.

For an infrared sensor:

$$T = \sqrt[4]{\frac{Q}{\varepsilon k}} \qquad \text{Equation 3.6}$$

Here Q is the radiated energy, ε is the emissivity (value 0-1) of the heated surface, k is the Stefan-Boltzmann constant and T is the temperature. As a result the emissivity is the most critical factor as it changes with temperature and surface films/roughness. Thus special high temperature near constant emissivity paint is usually applied to the surface being measured. It also should be noted that if the angle of the pyrometer changes, the emissivity may change as well as emissivity varies slightly depending on the incident angle of the beam. The one benefit of the 4^{th} power relationship in Equation 3.6 is that a 100% error in emissivity only leads to a 20% error in the temperature reading. Thus using a black body emissivity paint listed near 1 will inherently minimize calibration errors. Listed below are the advantages and disadvantages of pyrometers and thermocouples:

Advantages of a Thermocouple:

- Simple to use and very well established theory.

- Cost effective.
- Sufficient temperature range available (over 1000°C with K-type).

Disadvantages of a Thermocouple:

- Slow response time to large rates of temperature change. This is generally true for an inexpensive thermocouple. Specialty thermocouples can be purchased at a higher cost with a faster response time.
- Measures bulk temperature rather than surface temperature. This experiment is concerned with surface temperature.
- Contact method, meaning it is hard to repeatably install and avoid interfering with the mechanical motion of the disk.

Advantages of an Infrared Sensor:

- Non-contact method.
- Much faster response time than a thermocouple for steep temperature rise times (on the order of 5-10 times faster) (Trout 1980, 10-13).
- Measures surface temperature rather than bulk temperature.

Disadvantages of an Infrared Sensor:

- Dependent on emissivity which may not be known and may change in-situ.
- Operate on line of sight.
- Can be costly.

At this stage an Optris® CTLaser infrared sensor (single colour) was selected for temperature measurement. The emissivity problem was solved by purchasing stable calibration high temperature (up to 1100°C) black body emissivity paint from Aremco®. Using Omega® temperature calibration paint (accurate within +/-1°C

and available from 120°C to 1100°C in 100°C increments), K-type thermocouples and a FLIR T-300® thermal imagining camera the emissivity of this paint was found to be 0.85 for a straight on incident beam angle (i.e. zero degrees).

Temperature measurements from room temperature to 800°C were done in triplicates over 100°C increments (over 800°C was not attainable with this setup in the end). The calibration errors only varied at most by 5%. This paint is applied as a single or double coat with a paintbrush, allowed to dry for about 20 minutes and then is ready to use. Re-applying the coating every 5 tests or so was deemed appropriate (judged on a case by case basis).

A two-colour pyrometer is able to self-calibrate and avoid the need to know the emissivity of the surface being measured. However, the cost is much higher than a single colour pyrometer (can on the order of 10 times greater) and according to the sales offices of many prominent pyrometer distribution centres, the cancellation of the emissivity is not 100% perfected. The purchased Optris® sensor emits two beams and they converge at a distance of 15cm to form a 1.9mm spot size where the temperature is being read. The infrared sensor has the following operational characteristics:

Table 3.3: Optris® CTlaser Measurement and Operational Characteristics

Temperature Range	-40-975 °C	Class	2
Repeatability	+/-0.5 °C	Model #	LT-CF2
Accuracy	+/-1 °C	Type	Laser Diode CW
Resolution	0.1 °C	Lasing Medium	AlGaInP
Response Time	120 ms	Maximum Output	1 MW
Output Signal	0-10 V	Operational Wavelength	630-650 nm
Emissivity	0.1-1.1	Emergent Beam Diameter	1.9 mm

Shown in Figure 3.18 and Figure 3.19 are the 2 possible cases of temperature measurement: 1) measuring the static pin (paint near tip of pin) or 2)

measuring the disk temperature (emissivity paint near top edge of disk). Because the disk rotates, the temperature is measured in a new spot continuously. This was found to be beneficial based on thermocouple calibration to attain near uniform disk surface temperatures. A mechanical arm is attached to the infrared sensor to ensure the position of the beam remains constant during operation. This mechanical arm is adjustable with screws to allow for linear and rotational adjustment. Using both methods the beam spot is about 1-5mm from the interface. The interface temperature cannot be directly measured due to line of sight issues with the pyrometer. On the other hand a thermocouple directly at the interface would skew the friction results. Thus there is no direct and simple way to measure the interface temperature.

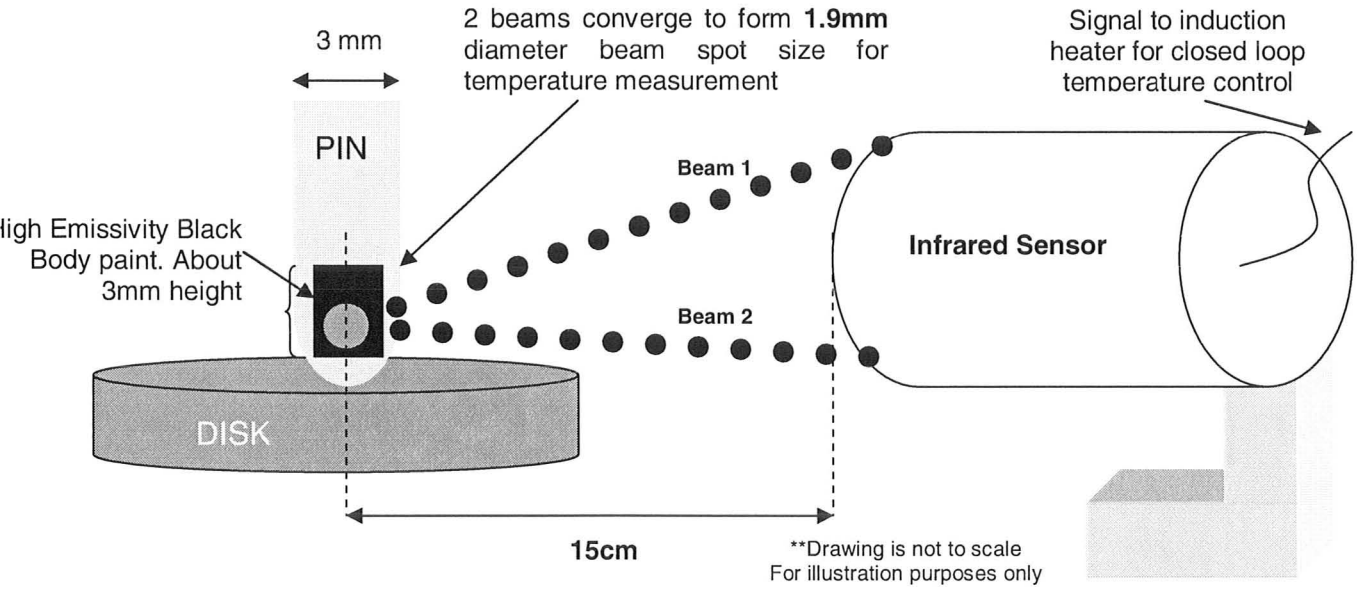

Figure 3.18: Pin Measurement of Temperature

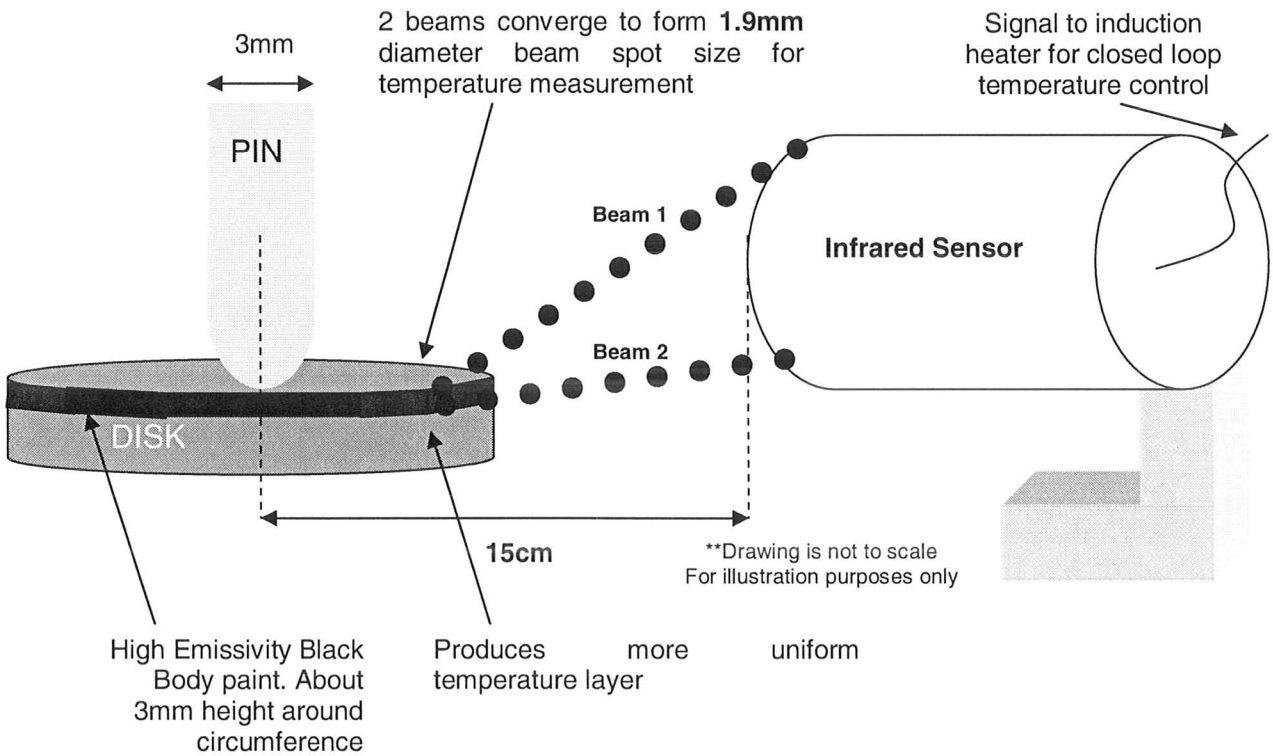

Figure 3.19: Disk Measurement of Temperature

Temperature can also be inferred from the post test colour of the disk surface. The disk surfaces tended to be a blue and purple colour at high

temperatures. The temperature control is closed loop with the temperature signal from the pyrometer being sent to a PIXSYS® PID controller which then sends a signal to the induction heater to either increase or decrease the current to the induction coil to maintain the desired setpoint temperature. To control the ramp up rate of the heater, the PIXSYS® output power limit is adjusted. A value of 100% lets the induction heater use up to 300A maximum and a value of 0% 0A maximum. The PID parameters of the PIXSYS sensor were tuned so that the system is overdamped and never/barely overshoots the desired temperature setpoint. The feedback loop is shown in Figure 3.20.

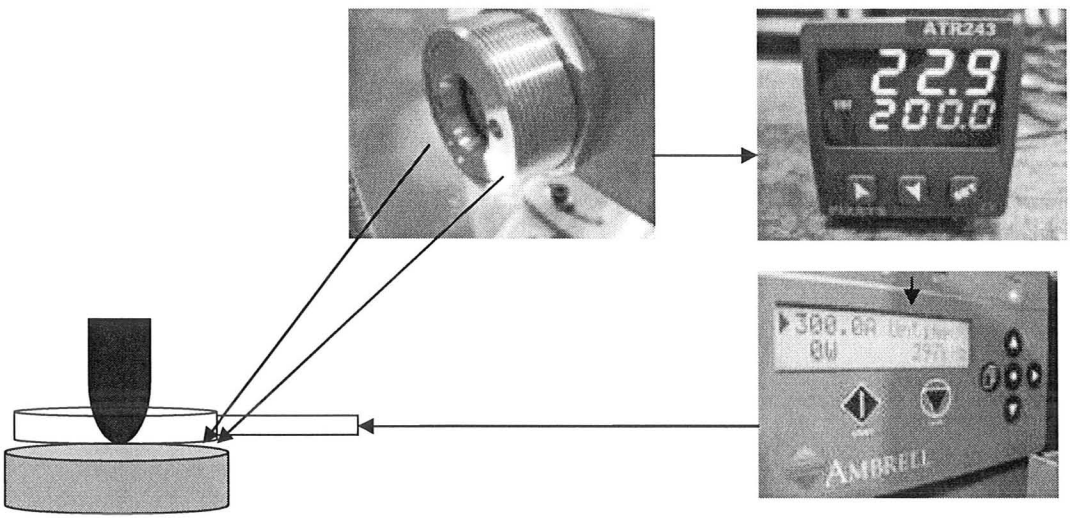

Figure 3.20: Temperature Control Feedback Loop

3.4.7 Disk Holder Design

An independent 4 jaw chuck was selected to hold the disk. An independent 4 jaw chuck has the advantage of being able to hold and move a variety of disk shapes. In addition to the chuck a ceramic holder was manufactured to avoid the chuck acting as a heat sink to reduce the efficiency of the heating.

The ceramic chuck has 4 aluminum strips with the same radius as the ceramic holder to place between the chuck jaws and the ceramic holder to avoid the chuck jaws damaging the brittle ceramic holder. Two sets of chuck 4 jaws are available, a smaller set and a larger set, depending on the specimen.

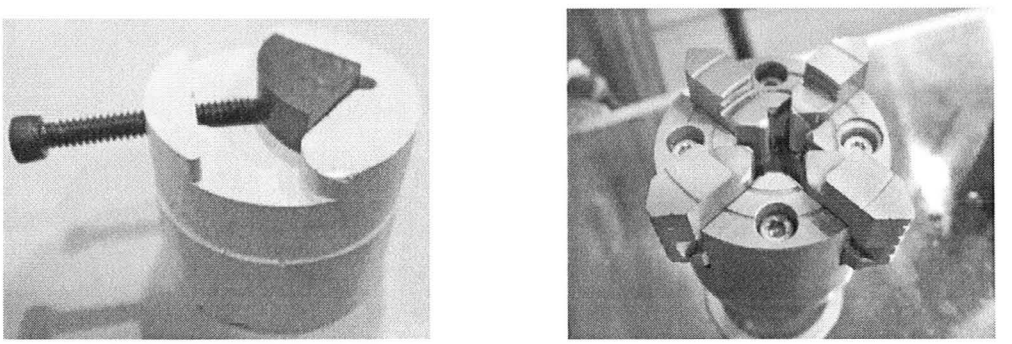

Figure 3.21: Ceramic Holder (Left) and Chuck Design (Right)

3.5 Computer Software and Data Acquisition

Computer controlled software was provided with the unit to control the unit. The load PID controller needed to be re-tuned. The original data acquisition software with the unit was not sufficient for collecting all the data points now used during testing. The original data acquisition rate also was not high enough. For this reason a LabVIEW program was created to allow the user to monitor the load, reaction torque and temperature in real time or data acquisition mode. All variables are graphed on the same time scale which makes comparisons between the data relatively easy. Figure 3.22 shows a sample screen shot of the LabVIEW software. The Nanovea® software is programmed such that no disk rotation occurs until the setpoint load is achieved.

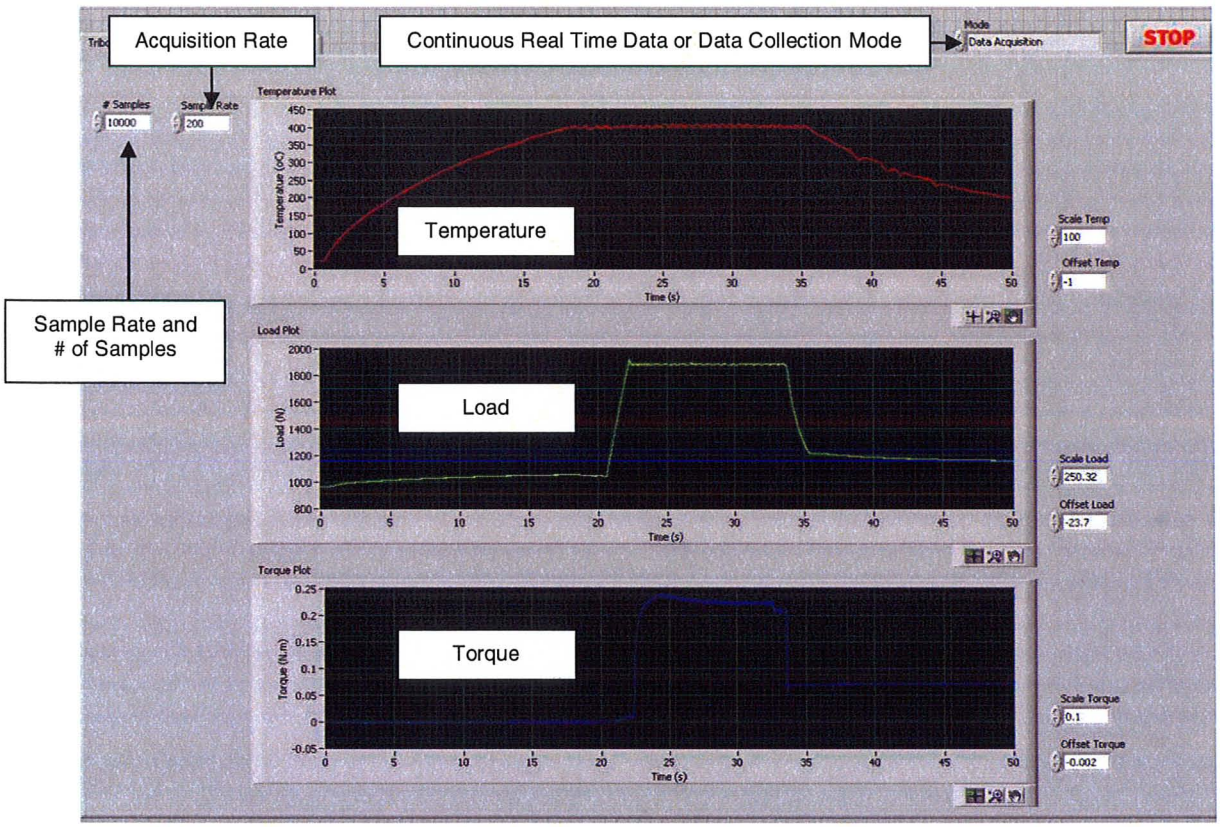

Figure 3.22: Screenshots of LabVIEW Computer Software

Chapter 4. Testing Procedure

The testing procedure is critical. The following steps are listed in the order that they were followed for each result collected in this thesis. Some calibration steps only needed to be processed once. The test procedure is broken into two parts: 1) Operation of the tribometer and 2) Data processing.

4.1 Operation of the Tribometer

1. Prior to starting any of the tests, the reaction torque sensor charge amplifier and infrared sensor instrumentation was turned on and allowed to warm up for a minimum of 6 hours. The longer these instruments were on prior to testing the better. Next it was ensured the charge amplifier was set to charge mode at a

value of 2160 pC/MU and a scale is 0.1 MU/Volt. The emissivity of the pyrometer was set to 0.85. The tribometer itself was turned on right before testing.

2. Next the Nanovea® tribometer software application and the LabVIEW® data acquisition program was opened. The LabVIEW data acquisition program was then placed in continuous data collection mode with the torque sensor in operate mode. This ensured that during setup the torque can be monitored to avoid breakage.

3. Next the temperature needed to be calibrated. A coil was chosen and a dedicated tungsten carbide calibration pin was placed in the collet and properly dialled in. The Kistler® sensor and collet needed to be removed from the attachment connected to the splined shaft before placing the pin in the collet. Before tightening the collet, high temperature anti-seizure paste was applied to the threads of the collet. Next the torque sensor assembly was reattached to the splined shaft assembly. The unit was positioned so that the centre axis of the pin matched the centre of rotation of the disk. A dial indicator with a resolution of 0.01mm was used. While a potentially tedious step, once the pin is in position, several tests can be completed before having to re-do this stage. Even though the temperature calibration stage is static (meaning the disk does not rotate) the pin was always dialled with the reaction torque sensor to prevent overloading issues due to misalignment. The calibration pin had 2 k-type thermocouples soldered on the surface. A 3rd thermocouple was sandwiched under high load in-between the pin and disk.

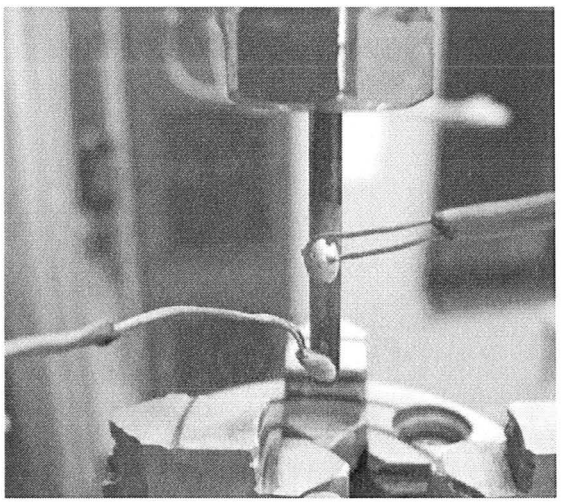

Figure 4.1: Temperature Calibration Pin

4. Next a sample disk was inserted into the ceramic holder. The ceramic holder with the disk was then placed the chuck. The ceramic holder was tapped down once the jaws were fairly tight to ensure the surface was level. A dial indicator was placed on the flat part of the disk while spinning the chuck to ensure it was flat.

5. Now the induction heater was moved into place. The induction heater moves on a hinge and can be moved up and down via a set screw type retort stand. It also swivels in and out on a hinge. The induction coil was placed such that it was not touching the pin or the disk.

6. Next the temperature calibration was made. Disks may be of different shapes, sizes and materials and thus the heating requirements may differ from test to test. Black body emissivity paint was added to the pin or disk. The output power % on the PID controller was tuned from 0-100% to achieve the desired heating rate. The pyrometer beam was positioned so that the two beams converged on the appropriate spot whether heating the pin or disk. Ideally the

pyrometer beam was placed overtop of the K-type thermocouple on the pin 1mm away from the interface. Three trials were completed from room temperature up to the maximum power settings to determine the range and repeatability. In all cases it was found that the pyrometer and K-type thermocouple agreed within a few degrees Celsius so the pyrometer values could be trusted. The interface temperature tended to only be about 5% higher than the pyrometer reading. This error bar may need to be adjusted on a case to case basis. . During this test the vortex chiller was aimed at the collet to avoid overheating. The 2 air lines were aimed at the reaction torque sensor.

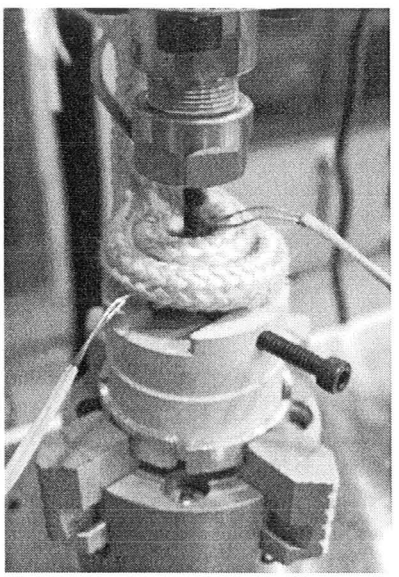

Figure 4.2: Temperature Calibration

A reality check during this calibration is that once temperature reaches the 600-700°C range, the disk or pin interface should in most cases be glowing cherry red or orange. Also the disk surface near the interface should resemble the chip colours from the actual machining process. If the specimens do not show these

colours then it is possible that the temperature calibration is incorrect and needs an adjustment.

7. Once the temperature calibration was completed the actual test specimens were retrieved. The pins and disks were cleaned before use. If they were being reused they need to be polished first (this will be explained in detail in a later step). The disks were cut to the appropriate dimensions. If the disks were being reused they were ground down so that the impressions of previous tests and contaminants were removed. A grinding wheel was used, taking 0.005mm per pass to minimize the impact of high temperature and strain hardening on the disk sample. The amount of material to be removed is based on experience and judgement. In general at least 2 passes were required so that the impressions were no longer visible to the naked eye. Gloves were worn so that handling all specimens did not lead to contamination of the samples. Medical grade gloves worked well. Next 2 coats of Aremco® black body high temperature emissivity paint was applied on the pin or disk depending on the heating scheme. The first layer dried in room conditions for 10 minutes and then a second coat was applied. A new coat was applied once a specimen was tested 4 or 5 times. The pin and disk were cleaned using isopropyl alcohol and a compressed air canister to remove any larger debris. Isopropyl alcohol is less aggressive than acetone which may affect some of the coatings on pins. At all times the specimens were handled with tweezers if possible to avoid recontamination.

8. Next the standard tribometer checklist and documentation sheets (approximately 5 sheets of data) were filled out (note this document contains pre

and post testing information). A Phillips SEM-515-LAB60 was used before and after testing with energy dispersive spectroscopy (EDS) for elemental analysis. A stitching microscope was also used to acquire high resolution colour images of the wear patterns.

9. The appropriate elements of steps 3-8 were then repeated for the actual test specimens to align and position on the tribometer. The data acquisition rate was set to 200 samples per second for 6000 samples (i.e. 30 seconds of recording) to ensure all the data was captured. The system was manually loaded to 1000N, held for 1 minute (to ensure plastically deformed), then the data acquisition system was started and the induction heater activated. Once the setpoint temperature was reached the system was loaded to 1900N via computer control. Once the load stabilized, 1 RPM of disk rotation commenced for 10 seconds. A small amount of coolant was placed between the pin and disk before heating and motion to simulate what happens on the industrial machine. Coolant was not supplied once testing started. 10 seconds was used for test time as it allowed enough time to reach steady state, prevent overheating and excessive oxides from forming. While the unit is capable of 2000N the effect of load on COF at this high level is negligible, also the software has a built in safety subroutine that shuts off the test if 2000N is reached so backing off to 1900N ensured the unit would not shut off unexpectedly during the test. It was found with this pin arrangement that the stresses generated using these loads were in the range of 1-4 GPa which was a requirement for this type of test. Test temperatures started at

room temperature and went up by 100°C or 200°C increments. Each test point was repeated 3 times in succession.

10. After each test the tribometer checklist and documentation was filled out. The pin was left in the collet so that alignment process did not need to be repeated. It was found that after about 25 consecutive points the pin is no longer usable. After each test the pin tip was polished and pickup material removed while still in the collet. To do this the pin was spun at 2N load for 5 minutes at 500RPM on a piece of soft cast iron placed in the chuck. Next a 2N load was applied for 5 minutes at 500RPM on a soft nap cloth with 0.05micron alumina oxide polish in the chuck. Then the pin was then cleaned with isopropyl alcohol and an air duster. This cast iron and nap cloth cleaning test was verified using the SEM images to verify that pickup material was removed but that hard protective coatings were not damaged. Cast iron is abrasive enough to remove pickup but not hard enough to remove a hard coating. Ideally the piece of cast iron has a print in it from a heavily applied load made earlier (acts like a polishing die). The test steps are then repeated until all data points are obtained.

4.2 Data Processing

Once the data was collected, it was processed in Excel® or MatLAB® and graphed in Origin® so that the data could be represented on the same screen with the same time axes in high resolution. The coefficient of friction (COF) was represented as the steady state value. In our testing, each test point value was the average of the last 2 seconds (200 samples per second x 2 seconds = 400 samples) of testing. Thus using 3 replicates for each test point, 1200 points were

used to calculate the single listed average COF value and standard deviation for a particular temperature. This 2 second time length average was determine based on extensive experimentation and may be adjusted if deemed appropriate. From experience the steady state value is reached within the first 5 seconds of the test. The disks are measured under the microscope if no lip exists and the average radius (R_{IND}) of 2 perpendicular indentation points is recorded. At this point COF can be calculated. The pins along with the disks can be analyzed by the white light interferometer, SEM and stitching microscope to look for pickup material and wear scars. A typical friction curve produced by this unit is listed in

Figure 4.3 if aggressive adhesion is successfully achieved in machine like conditions. This curve was found both in this testing and with the results of Shuster. This result was also found by the work of Blau who identified 8 typical COF vs. time graphs based on a significant number of tests.

Figure 4.3 is viewed as one of the most common break in curves (Blau 1971, 30).

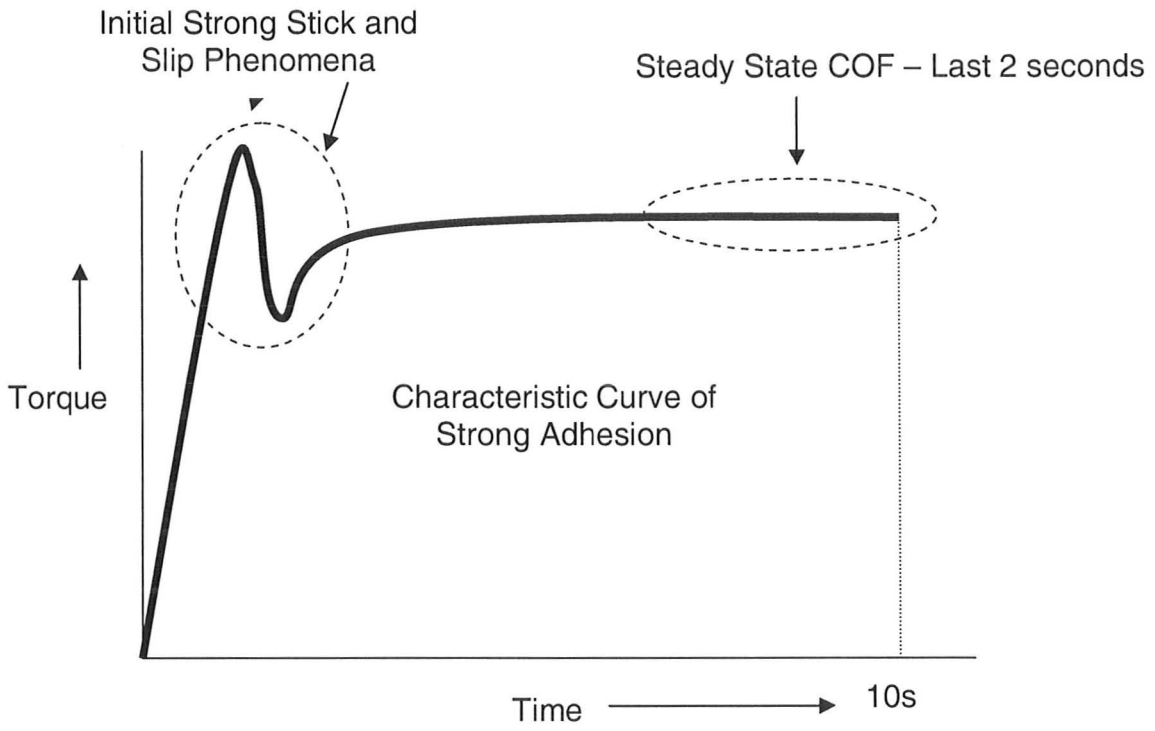

Figure 4.3: COF vs. Time for Aggressive Adhesion

The graph in Figure 4.4 is also one of the 8 common curves found by Blau but for less aggressive adhesion at the start.

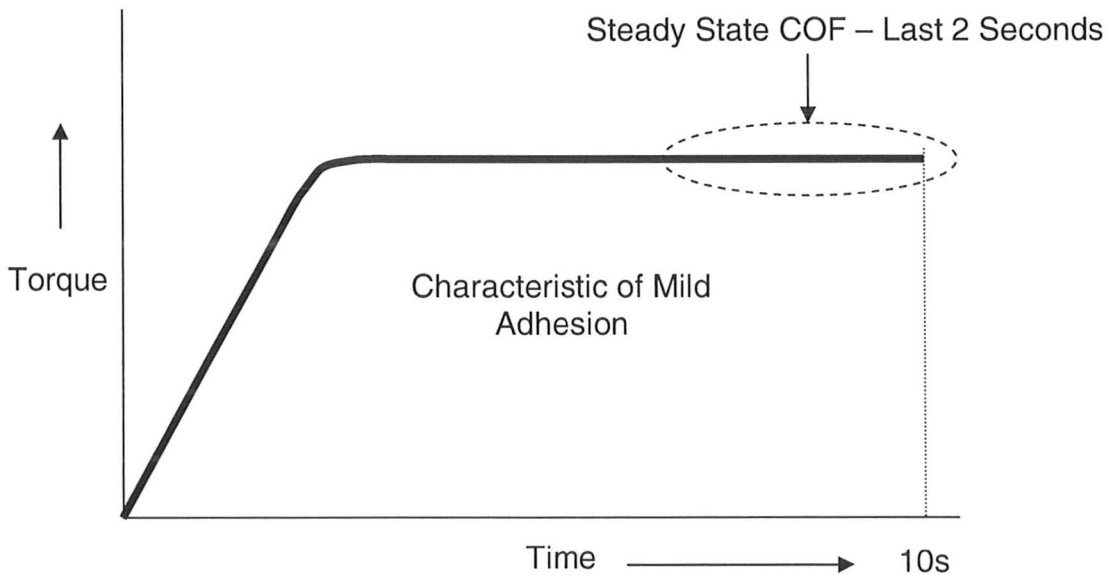

Figure 4.4: COF vs. Time for Non-Aggressive Adhesion

It was found based on extensive testing and verified by the work of Godfrey (Godfrey 1995, 124) that if the pin is not uniform or the pin is off centre from the axis of rotation, the torque curve will resemble a sinusoidal wave with the frequency matching the rotational RPM of the disk as sketched Figure 4.5. For a 10s test at 1 RPM only $1/6^{th}$ of a cycle would be shown. Tests using up to 100RPM showed that indeed this repetitive sine wave form existed.

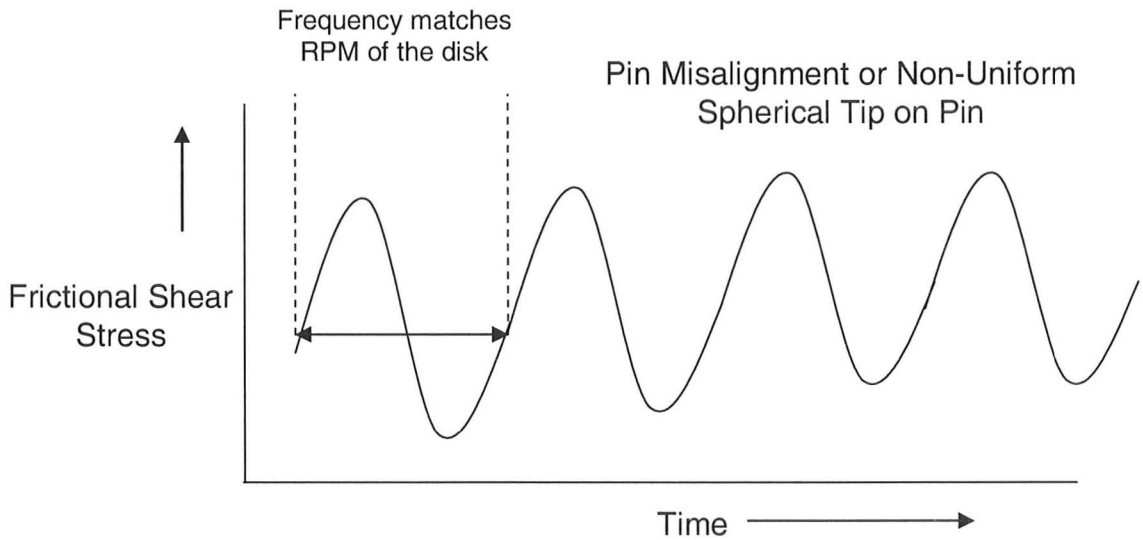

Figure 4.5: Friction Curve for Pin Misalignment or Non-Uniform Pin Tip

If this sinusoidal signature occurs it is recommended to repeat the test and check the alignment and/or produce a higher quality pin. If this is not possible, then the RMS value of the signal may be taken as a quasi average result for the friction. Once this testing is completed an important question arises: How much better does a coating have to be on the bench scale to translate into better performance on the machine? Shuster has shown in several cases that if the COF is lowered by a minimum 0.05-0.10 and the standard deviation error bars do not overlap then wear improvement on the industrial machine is highly probable. This finding will be compared to the MMRI results.

Chapter 5. Experimental Test Results and Discussion

To validate the MMRI tribometer results, 2 sets of data are being used: 1) data collected from a custom tribometer made by Dr.Shuster which was shown previously in Case 3 and 4 in Chapter 2 and 2) MMRI machining tests. Uncoated and Balzers® AlTiN Xceed® tungsten carbide pins were used. The workpiece materials were Ti6Al4V (37 Rockwell hardness) and Inconel 718 (51 Rockwell hardness). These materials were selected as the MMRI has the most experience and data on these alloys. The 3 types of induction coils as described earlier were tested. For all data listed, the temperature plotted is the estimated temperature at the interface. Preliminary testing showed that RPM had minimal effect on the results. Thus 1 RPM was used for stability and near seizure conditions.

Table 5.1: MMRI Testing Matrix

Pin	Pin Coating	Disk	Types of Induction Coils
WC – 6% Cobalt	Uncoated	Ti6Al4V	3
WC – 6% Cobalt	Balzers Xceed - AlTiN	Ti6Al4V	3
WC – 6% Cobalt	Uncoated	Inconel 718	3
WC – 6% Cobalt	Balzers Xceed - AlTiN	Inconel 718	3

The test conditions for all tests were as follows:

Table 5.2: Proposed Testing Matrix Test Conditions

Disk Rotation Speed	1 RPM
Normal Load	1900N
Temperature Range	Room Temperature – 975°C
Test Time Once Rotation Starts	10s

The reasoning behind using 3 different coils was that during preliminary testing, it was found that not only does the interface temperature matter but of equal importance the temperature gradients within the disk or workpiece material also matters. These 3 coils offer vastly different temperature gradients for similar interface temperatures. Titanium was tested first because of its lower hot

hardness when compared to Inconel. Based on this property it is easier to assess the thermal sensitivity of the measurements.

Case 1: 2 Turn Round Coil

A 2 turn round coil was placed around the pin about 5 mm away from the interface and the pyrometer beam was placed approximately 1mm from the interface which is as close as possible due to space constraints. Three thermocouples were used to validate temperatures as outlined in the tribometer procedure to verify the pyrometer measurements. A thermocouple was also added to the disk about 1mm away from the pin-disk interface to assess the temperature gradient on the disk. The results showed that the diameter of the pin print grew steadily with temperature up to 800°C. Due to power constraints and setup issues over 800°C was not attainable with this setup.

The COF for this test remained near constant across the entire temperature range. 3 test replicates per test point found a COF value around 0.23 +/- 0.01 on the Ti6Al4V disk. Based on the results shown in the literature such as Shuster (Fox-Rabinovich, Yamamoto and Veldhuis, et al. 2006) it was expected that the COF would rise with temperature and then fall. This puts the results achieved in this setup into question. Further investigation revealed that the disk print area was the same colour as before testing, which indicated that the disk material in this region did not reach a high temperature. Additional temperature measurements from the disk thermocouple, about 1mm from the pin-disk interface indicated that the material near the contact point was lower than expected. This also indicates that there is a very steep temperature gradient over the approximately 1mm

distance between the interface and the thermocouple measurement on the disk. This was not expected. Furthermore, SEM images and EDS analysis showed minimal adhesion or pick up of workpiece on the carbide pin. Under machining conditions, intensive worjpiece pickup is typically observed. However SEM images did indicate cobalt oxide formed on the pin tip for the uncoated pins. This cobalt was visible to the naked eye as a blue residue and indicates the pin reached a high temperature.

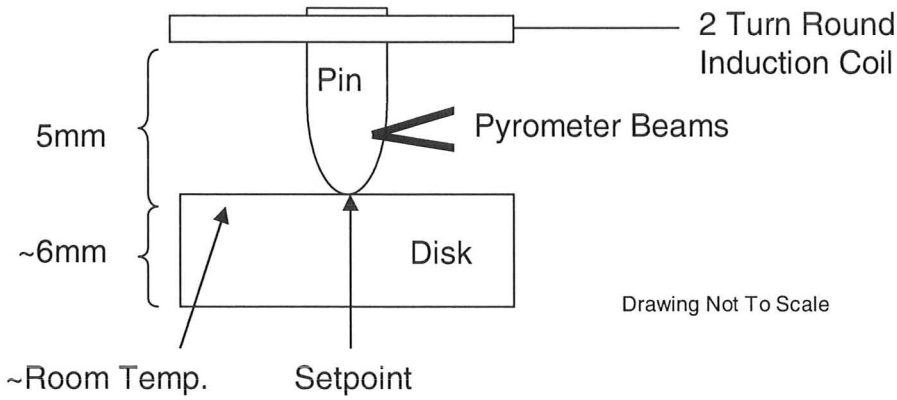

Figure 5.1: Case 1 Heating Illustration

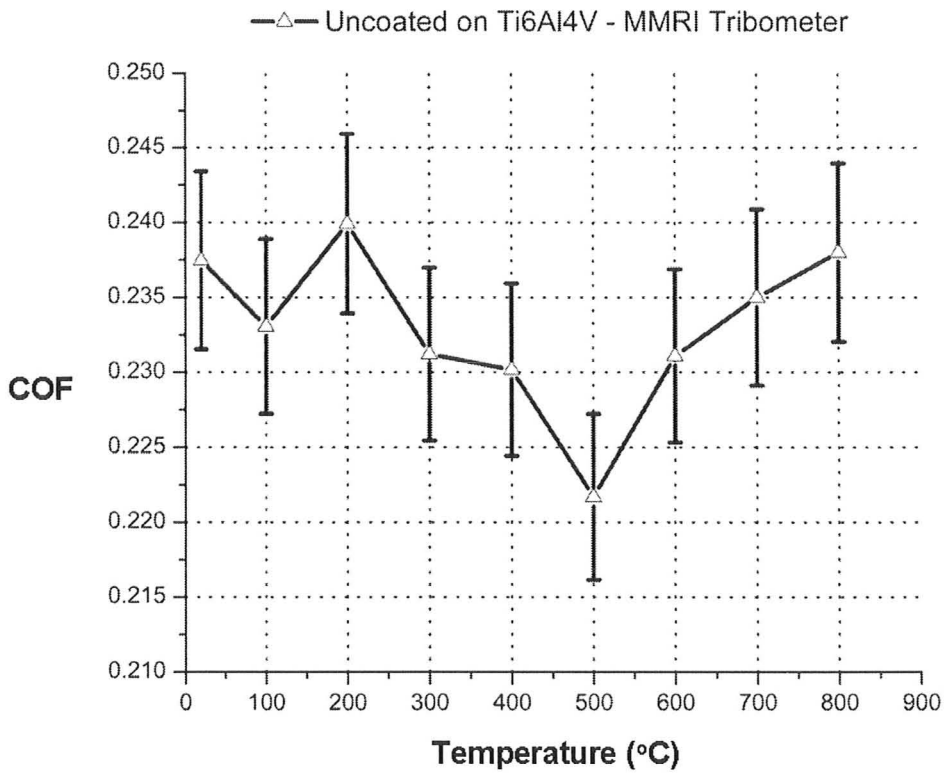

Figure 5.2: Illustration of COF Dependency on Temperature for Case 1 Type Heating

Preliminary testing was also completed on coated pins and Inconel however the initial trials exhibited similar friction and SEM results. Thus Case 1 testing was halted and deemed a poor simulation of metal cutting conditions. This also avoided exhausting workpiece specimens on an inappropriate test.

To investigate the temperature distribution further a pancake coil design was attempted which heats the flat surface of the disk as well as the pin more uniformly rather than in a focused point like Case 1. The pancake coil is placed directly on top of the disk with the pin in the centre. The pyrometer was aimed at the disk and in this way more heat energy is supplied to the disk rather than just to the pin.

Case 2: 2 Turn Pancake Coil

The pancake coil was setup such that the coil was about 1mm above the disk and the pyrometer was as close as possible to the top edge of the disk. Heating the edge of the disk showed a near uniform disk temperature across the top surface of the disk including the interface. This is attributed to the nature of the coil and the disk rotating slowly which changes the surface that the pyrometer beam measures.

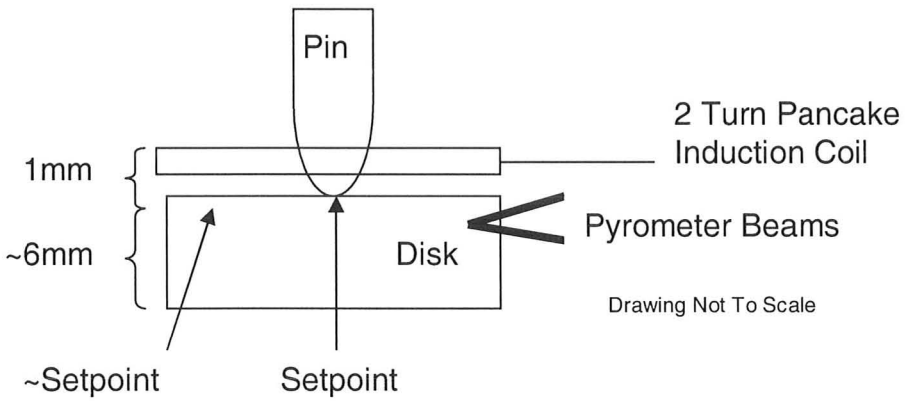

Figure 5.3: Case 2 Heating Illustration

The result for Case 2 using the workpiece materials was that COF increased at a catastrophic rate. At around 700°C the torque sensor was reading about 0.8-0.9 Nm, which is nearly the limit of the sensor. Coincidentally about 700°C was the highest temperature this setup could reach. In Case 1 about 0.35Nm was the maximum reaction torque. As a result, testing was halted at this temperature to preserve the sensor. It was found that the pin did not have the cobalt oxide blue colour which indicates that the pin was cooler. The entire surface of the disk was now blue and purple indicating that high temperatures typically seen in chips produced during metal cutting were reached. The impression on the

disk from the pin approached the diameter of the pin (3mm) indicating the majority of the Titanium was too hot and softened thus leading to internal friction or shear which is not desired in this case. At 600-700°C range the COF was in the range of 0.4-0.6 which was much higher than the values recorded in the literature by Shuster (Fox-Rabinovich, Yamamoto and Veldhuis, et al. 2006). SEM data indicated more pickup of the Titanium to the pin than Case 1. However this pickup of material on the pin was not severe and was only visibly under x500 magnification or higher. This was a surprising finding as we expected large amounts of pickup under these conditions. Thus some feature of the surfaces and temperature do not match machining. The coated AlTiN pin was tested in this setup to verify that the catastrophic friction was not due to the fact that the first pin tested had no lubricious coating.

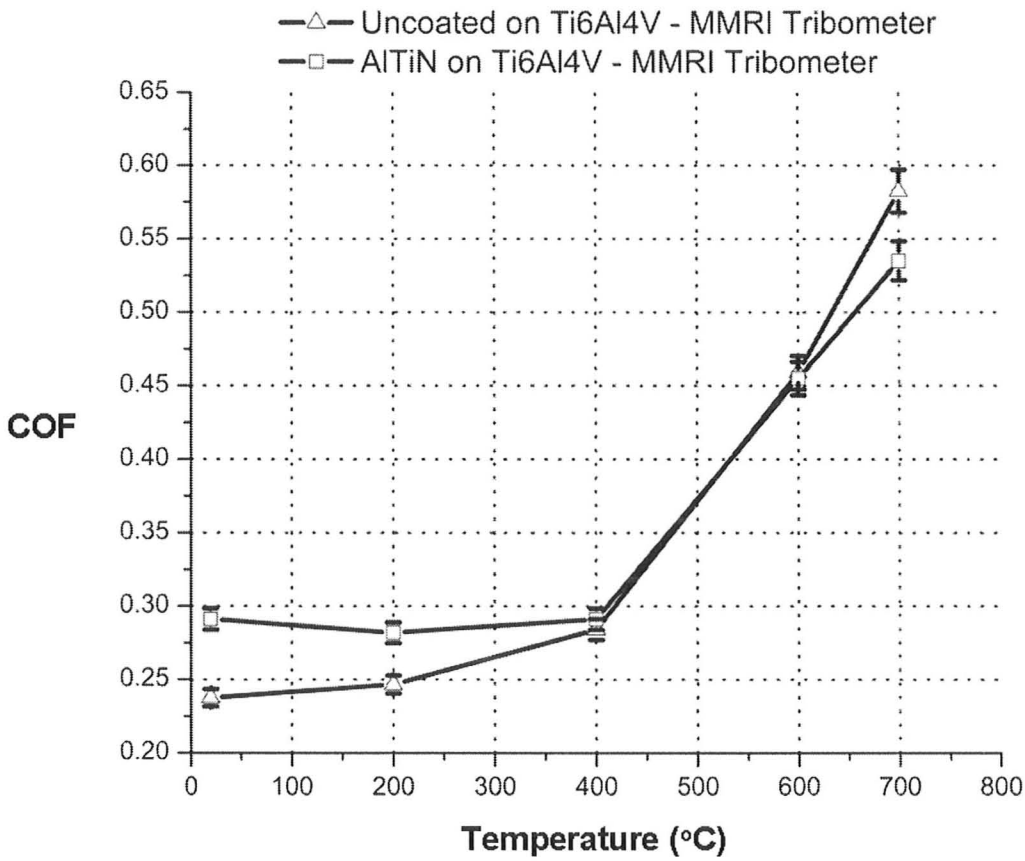

Figure 5.4: Illustration of COF Dependency on Temperature for Case 2 Type Heating

As a result it was determined that there was a strong likelihood that the proper heating regimen to get adhesive interaction and the typical COF curve that rises and falls with temperature was a heating coil which would heat the pin and the disk simultaneously with a gradient somewhere in-between Case 1 which was "cold" and Case 2 which was "hot". As a result, a hybrid coil was constructed (Case 3) that combined the beneficial qualities of the coils in Cases 1 and 2.

Case 3: 1 Turn Pancake Coil and 2 Turn Round Coil

This hybrid coil was placed about 5mm from the disk surface with the pyrometer beam on the pin. Constructing induction coils was found to be both an art and a science. The logic for the number of turns for this hybrid coil was based purely on experience developed over the course of this research. This Case 3 coil

allowed the entire disk surface to be heated with the heat energy focusing on the contact region. This meant that the region around the contact point only reached a level of 50% of the interface temperature as verified by thermocouples.

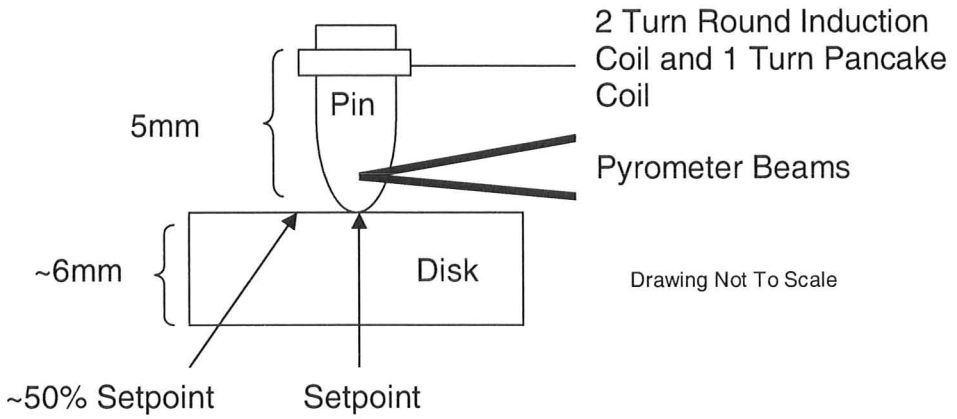

Figure 5.5: Case 3 Heating Illustration

The pin prints on the disk using this heating regime had localized blue and purple colours which are typical of chips from machining at high temperatures rather than the whole disk surface being coloured. Also the disk when handling after the test was hot to touch by hand indicating that more than just the interface was hot. Shown in Figure 5.6 is a visual comparison of a Ti6Al4V disk heated for each case type.

Overall View of All 3 Disks (Case 1 - Left, Case 2 - Centre, Case 3 - Right)

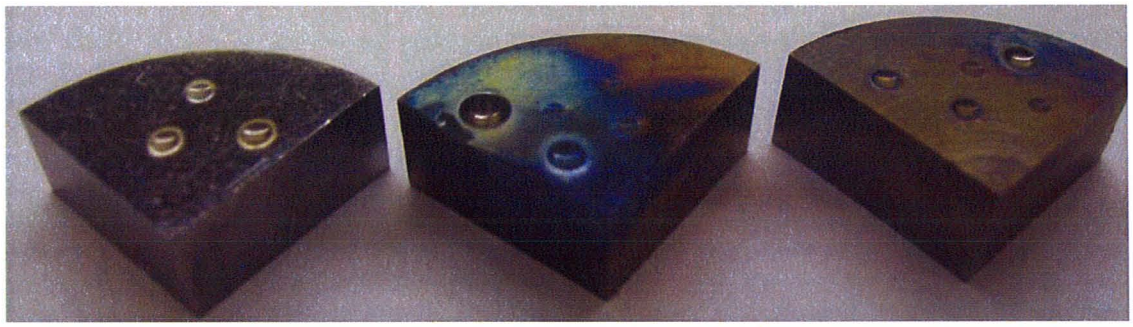

Case 1 Close Up	**Case 1 Comments**
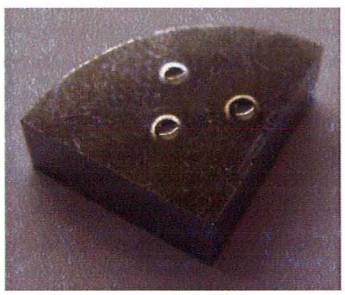	• Near constant COF over entire temperature range. • Disk does not change colour with increased temperature.
Case 2 Close Up	**Case 2 Comments**
	• COF rises catastrophically. • Print diameter approaches pin diameter. • Disk very discoloured.
Case 3 Close Up	**Case 3 Comments**
	• COF rises and falls with temperature. • Disk slightly discoloured.

Figure 5.6: Photo Comparisons of Ti6Al4V Disks for Cases 1-3.

Heating could not get above 700-800°C for this Case 3 arrangement. Based on this heating procedure, the Ti6Al4V and Inconel material were tested with and without coating as this was deemed the most appropriate heating regime. SEM images confirmed adhesion pickup of the disk materials in both cases but still did not exhibit the extreme pickup behaviour expected. In all 3 cases white light interferometer, stitching microscope and SEM before and after images did not provide significant insight as expected. Images before and after testing looked nearly identical. Only EDS elemental analysis proved very useful. Cobalt oxide formed on the uncoated pins but not on the AlTiN coated pins. Thus AlTiN acted as a diffusion barrier. SEM images for all tests indicated after testing that the AlTiN was still intact on the pin surface. The COF values matched the range of values shown by Shuster (Fox-Rabinovich, Yamamoto and Veldhuis, et al. 2006) and followed the expected increasing/decreasing trend with temperature. The performance results are shown for COF, friction shear stress (τ), compressive stress (σ) and pin print radius (R_{IND}) with respect to temperature for all Case 3 results. The COF standard deviation for all trials was found to be within approximately +/- 2.5% of the listed average value (both for Ti6Al4V and Inconel). COF for both materials were in the same range of about 0.20-0.35 (coated and uncoated). The coated pins showed slight improvement for Inconel at high temperatures (600-700°C) and stronger improvement for Ti6Al4V in the 600°C range.

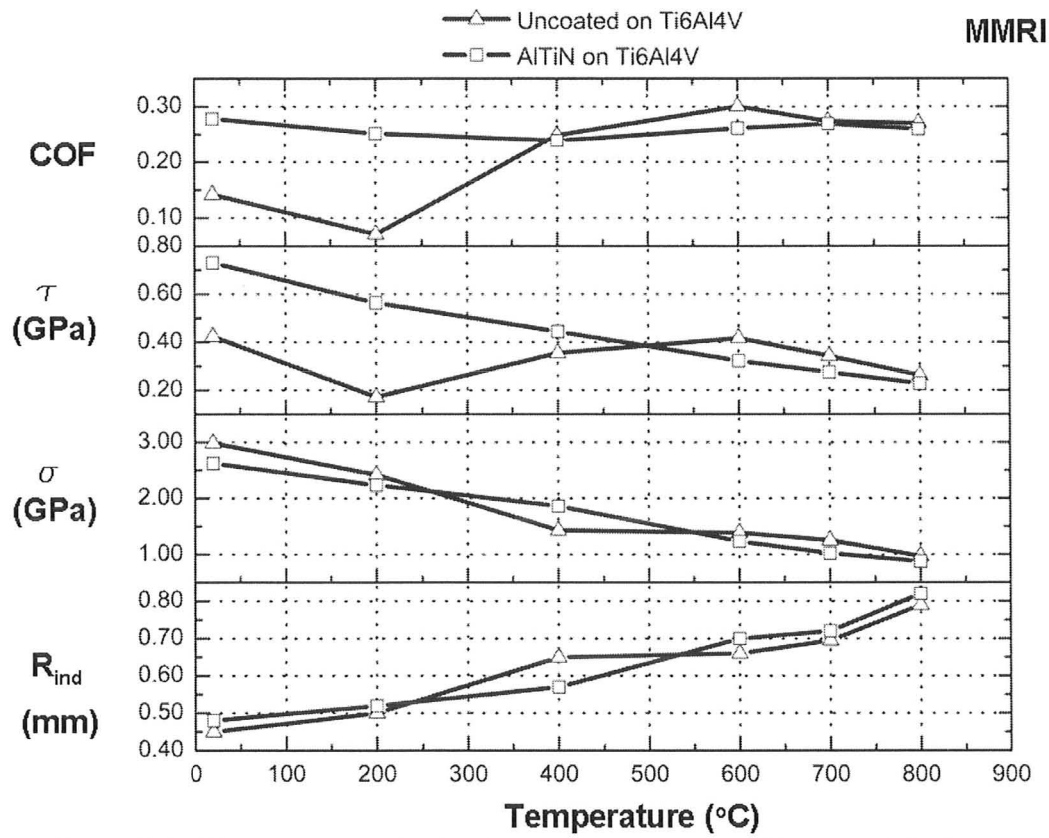

Figure 5.7: MMRI Tribometer Results for Coated and Uncoated Pins on Ti6Al4V

These results showed that for 600°C the AlTiN coating outperformed the uncoated samples on Ti6Al4V. COF for the AlTiN pin was 13% +/- 3% lower than the uncoated pin at 600°C. It is worth noting that Shuster's COF tests shown earlier in Cases 1-4, showed only a 0.05-0.1 improvement in COF yet resulted in significant improvement in machinability in the 400°C and higher range. The compressive stress (σ) decreased like Shuster's and had very similar values within 5% (using a 1900N load for all temperatures). R_{IND} increased for a constant load with increasing temperature as would be expected. This test showed that the compressive stress and imprint size is independent of a coating which makes intuitive sense. Figure 5.8 compares the MMRI tribometer results to flank wear tests completed in the MMRI for Titanium. The flank wear tests were done on an

end milling process and showed that the AlTiN insert strongly outperformed the uncoated insert. While COF shows a small improvement based on the MMRI friction measurements in the 600°C range, the performance in machining is far more pronounced. Three possible reasons may explain this result. Firstly, the findings of Rabinowicz stated earlier showed that wear for metals is often proportional to μ^4 (Rabinowicz 1995, 167). Thus a small improvement in COF will have a dramatic effect on wear. In this case a COF of 0.26 for coated vs. a 0.3 COF value for uncoated would produce a wear reduction by a factor of 2 according to Rabinowicz's findings which is close to the observed wear trends if the process interface temperature was around 600°C as shown in Figure 5.8. The COF results in Figure 5.8 are highlighted from 400°C to 800°C as this is a more relevant temperature range to machining. Figure 5.9 shows a high level of agreement for compressive stress between Shuster's tribometer and the MMRI's tribometer for the Ti6Al4V disk.

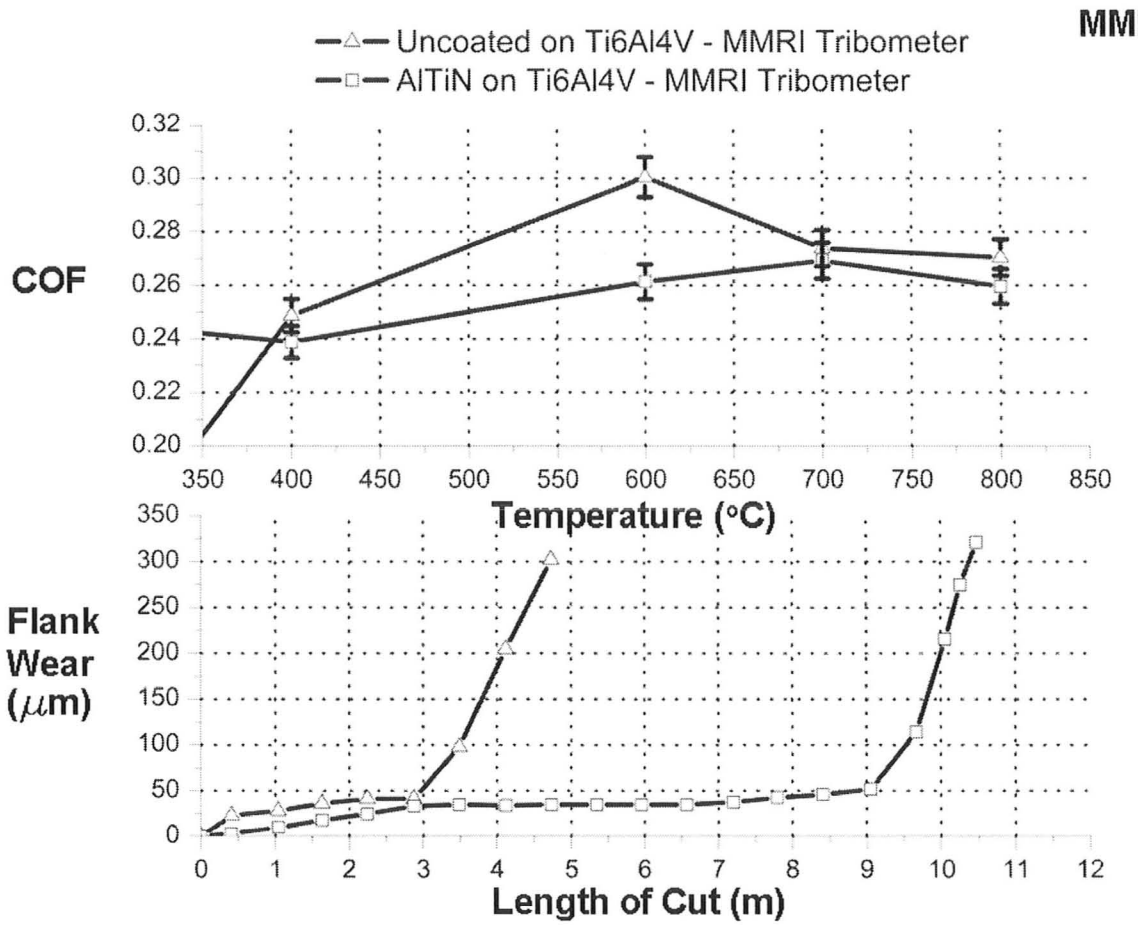

Figure 5.8: Comparison of Tribometer Data and Machine Data for Ti6Al4V

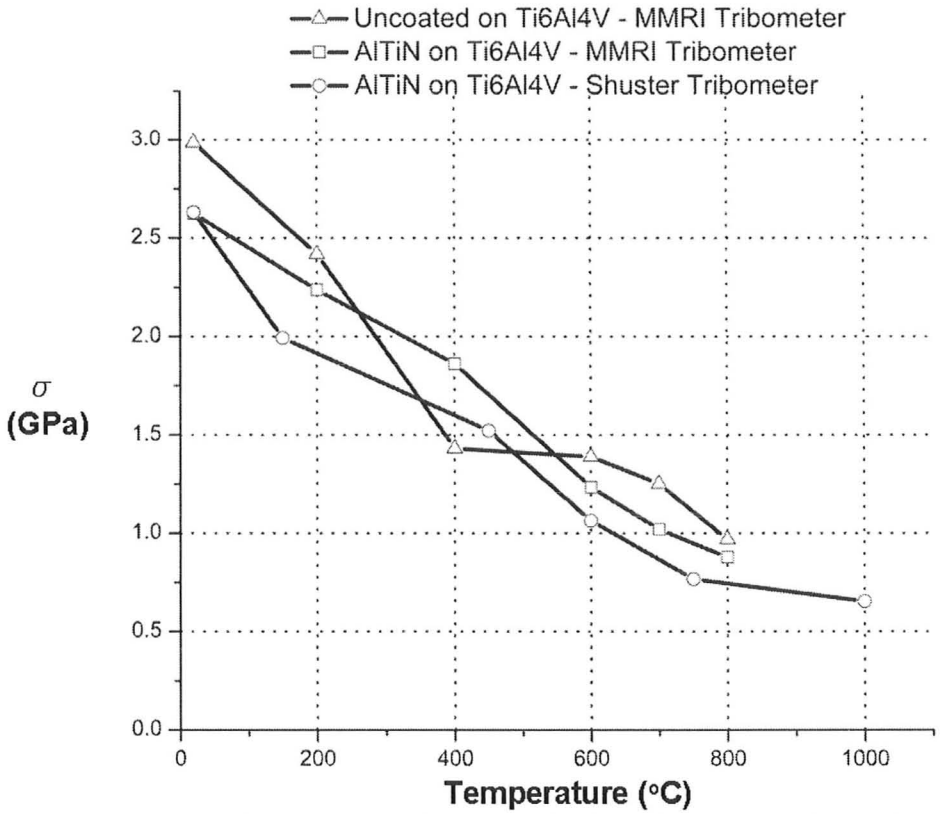

Figure 5.9: Comparison of Compressive Stress for MMRI and Shuster Tribometer on Ti6Al4V

Figure 5.10 lists the same type of comparison chart for Inconel for the MMRI tribometer results and contains the same experimental errors. At the high end of the temperature scale, which is relevant for machining, the results indicate the coated pins perform slightly better than the uncoated pins.

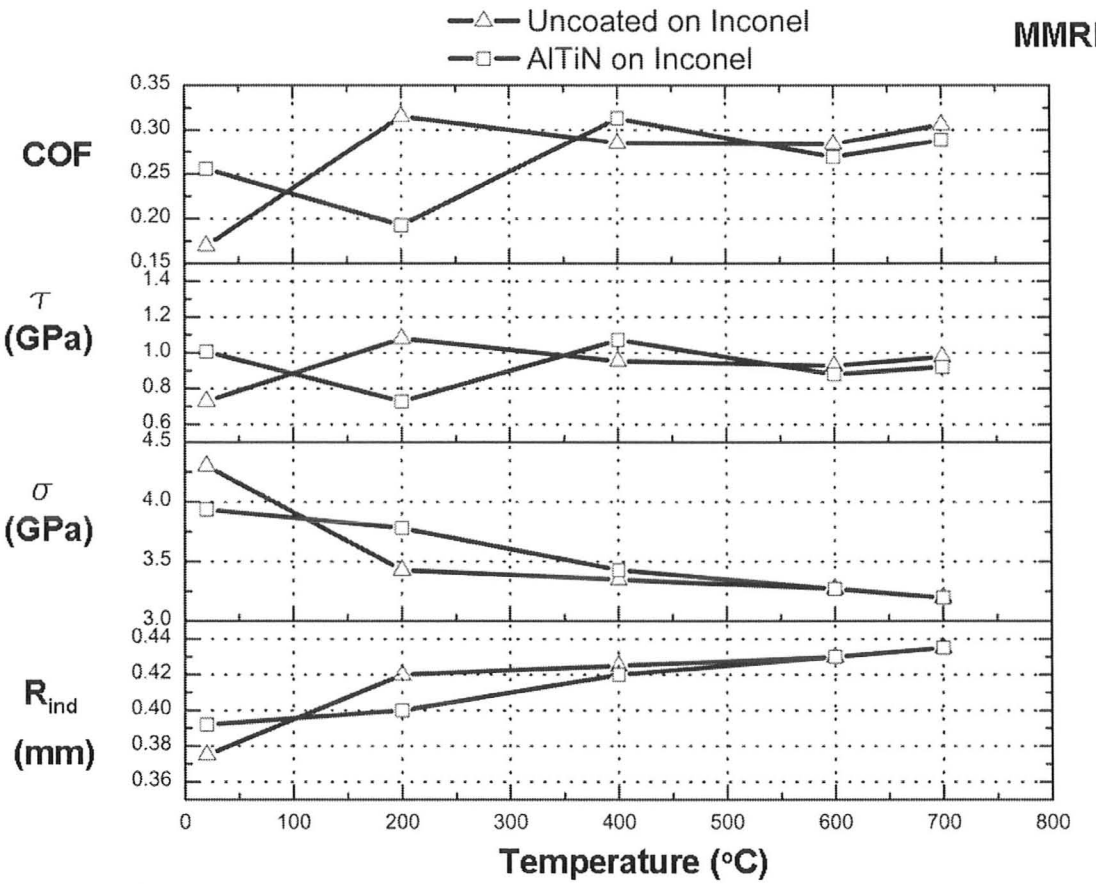

Figure 5.10: MMRI Tribometer Results for Coated and Uncoated Pins on Inconel

It can be seen that the compressive stresses are higher here than for Ti6Al4V. The load of 1900N was the same as the Ti6Al4V case but the Inconel was far harder than Ti6Al4V and retains its strength at higher temperatures thus the compressive stress was greater and the R_{IND} was much smaller. This is consistent with the results presented by Shuster (Biksa, et al. 2010). These compressive stresses for Inconel followed the same trend as Figure 5.9 for Ti6Al4V. The results of Figure 5.11 compare the MMRI tribometer results and flank wear tests completed in the MMRI. The flank wear tests were done in turning and show that the AlTiN inserts strongly outperform the uncoated insert in machining. While COF with a coating shows a slight improvement in the MMRI

tribometer results for Inconel the contrast does not match the large difference in the machining results. This may be due to the aforementioned reasons for Ti6Al4V. The COF results in Figure 5.11 are highlighted from 400°C to 700°C as this is a more relevant temperature range to analyze the data.

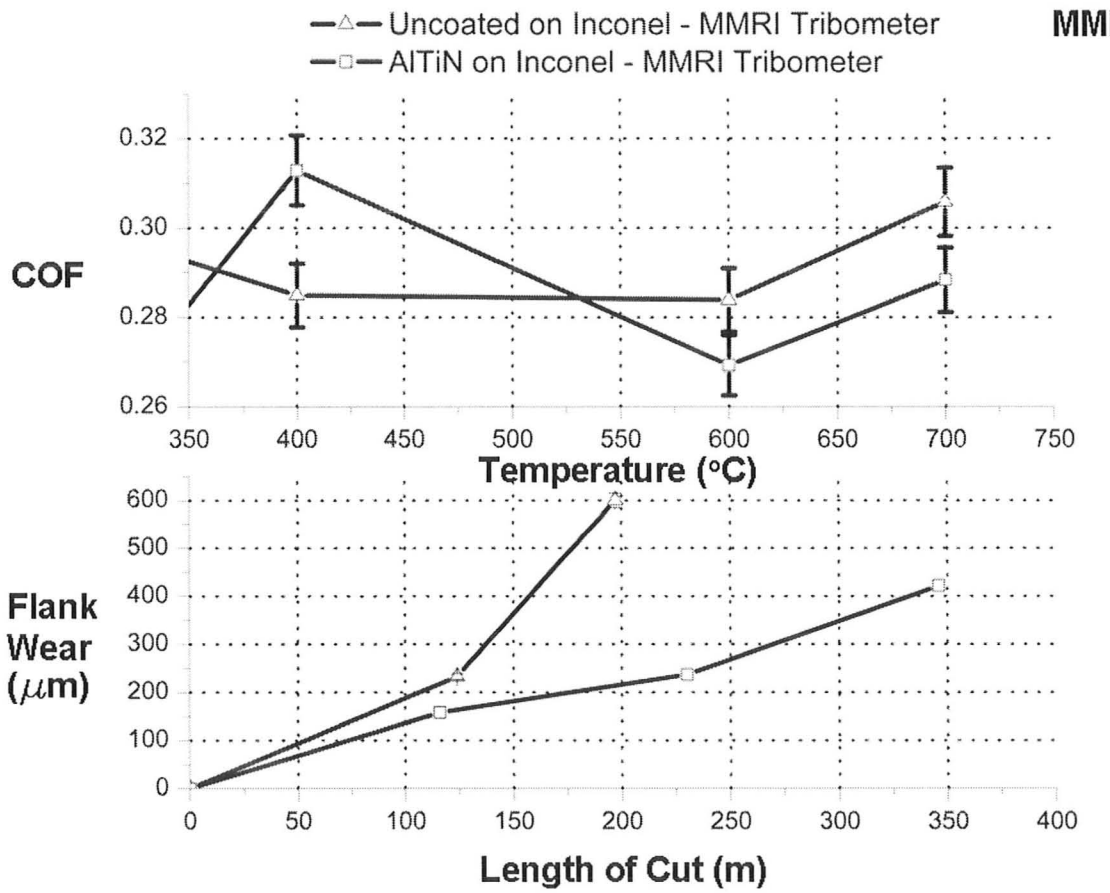

Figure 5.11: Comparison of Tribometer Data and Machine Data for Inconel

Thus the compressive stresses for the MMRI tribometer are in the correct range, COF is within about +/- 15% of Shuster's and several data points for Ti6Al4V and Inconel show a positive correlation with machine data.

Chapter 6. Conclusions

The MMRI tribometer produces similar rake face seizure zone conditions found in metal cutting. This has shown to have the potential to predict machinability based on a coefficient of friction measurement. Coefficient of friction for various hard to cut alloys using tungsten carbide tooling was found to yield COF in the range of 0.2-0.35. These tribometer results were validated against the work of Shuster and MMRI industrial machining tests.

Based on the setup currently in place the coefficient of friction can be calculated using the following equation for the tribometer test setup:

$$\mu_{MMRI} = \frac{3M_{TOT}}{2F_N R_{IND}} = \frac{\tau}{\sigma} = \frac{F_F}{F_N}$$

Testing showed that COF was relatively insensitive to compressive stresses in the 1-4 GPa region for a constant temperature. However, testing indicated that COF was very sensitive to temperature. The interface temperature and the temperature gradient were deemed most crucial to obtaining accurate results. A reasonable temperature gradient was found such that the disk temperature was approximately 50% of the interface temperature within a distance of a few millimetres from the interface. More research needs to be completed with regards to controlling the temperature in the contact region and extending the system performance to the 800°C to 1000°C range. Also, a larger matrix of coatings needs to be tested to validate the overall approach being taken in this research.

Chapter 7. Future Work and Recommendations

There are several recommendations based on this testing. The following recommendations are listed in the order of importance for the continued success of this test:

- Currently it costs about $18.00 for 1 doubled sided spherical polished tip pin of tungsten carbide from Canada Carbide® based out of Woodbridge, Ontario. This was an introductory price for 25 pins. Subsequent pins cost about $50-60 each. This is the same cost range for HSS pins. To do the multitude of testing we require, this cost becomes quite large. Finding a more cost effective solution is imperative.
- Develop more coatings and test on the tribometer. Develop a procedure for comparing the coating quality on a tool insert and pin to determine if the pins have the coatings adhere as well to the substrate as the inserts.
- Investigate the PVD coating processes at Balzers® and Kobelco® who are currently retooling their PVD process. Any issues with their coating chambers could induce errors to tribometer testing.
- Test specimen reversal (i.e. switch pin and disk) to determine the magnitude of this effect. Preliminary testing showed promise but further testing is required. An FEA model contrasting a hard pin and soft disk vs. a soft pin and hard disk would be valuable as a research tool.
- Need to find a way to make CBN, diamond and ceramic pins. These pins based on calling distributors cost several hundred dollars each. To avoid a Case 2 scenario where the pin is soft and disk is hard, these pins need to

be made out of these hard materials. Possibly DLC or CBN coatings can be applied to a tungsten carbide pin.

- Collaborate further with Shuster and determine COF for uncoated samples on Shuster's tribometer to determine in more detail how close the MMRI tribometer correlates with Shusters. It would be worthwhile for Shuster to ship used pin samples back to McMaster to analyze under the SEM to determine if the workpiece pickup on his pin matches McMaster's findings.
- Develop a trigger system for the reactor torque sensor. This would involve monitoring the torque and if it reaches a threshold value (say 0.9Nm), shut off the rotation and induction heater. Also mounting a thermocouple near the torque sensor rather than the temperature tape being used could trigger the induction heater to turn off if a threshold temperature (say 70°C) is reached near the thermocouple.
- FEA modelling for the tribometer pin and disk stress and temperature profiles is imperative. An initial model was constructed to verify the normal stress profile however more detailed work needs to be completed to map the stresses, temperatures and indentation profiles to more accurately calculate COF. Also a metal cutting FEA model would be extremely useful so that once the optimum conditions on the tribometer are found based on temperature, the cutting parameters in FEA can be adjusted so that their impact can be better understood and help tune the industrial machine.
- A K-type thermocouple feedback system was programmed into the control software but not implemented for testing (opposed to using the pyrometer).

A high temperature thermocouple cement (over 1000°C stability) from Omega® was purchased. Integrating the thermocouple with cement into the disk during a test would provide valuable insight to compare against the pyrometer control. It would also be useful to add a second temperature feedback loop to maintain a desired temperature gradient.

- Using an electrical resistance method may prove useful in addition to the induction heater to raise the temperatures from 800°C to 1000°C. A spot welder may be a possible solution. The induction company Ameritherm® also offers a 2 kW unit to replace the current 1 kW unit at a cost upgrade of approximately $3000-$4000. This would double the power and put the temperatures well over 1000°C.
- Implement a gravity fed lubrication module. 3 gravity fed lubrication modules have been purchased but need to be installed.
- Shaw notes there is some merit to a static diffusion test using high load and temperature with no disk rotation. This was not tackled as it takes some time to develop a procedure based on heating times and SEM techniques to develop a robust process (Rao, Kumar and Shaw 1978, 355).
- Electrical conductivity measurement has been shown to successfully show the formation and destruction of tribofilms at an interface. By plotting the conductivity signal in real time on the same axes as the reaction torque, it might be possible to get a glimpse into when film evolution is taking place. Bowden and Tabor noted that electrical contact resistance is a method appropriate to measure the contact area and the effect of films formed.

These films may be contaminants or oxides. Stachowiak also notes that electrical resistance changes at the interface may show the creation or destruction of a tribofilm (Stachowiak 2004, 45). A possible setup is illustrated as follows:

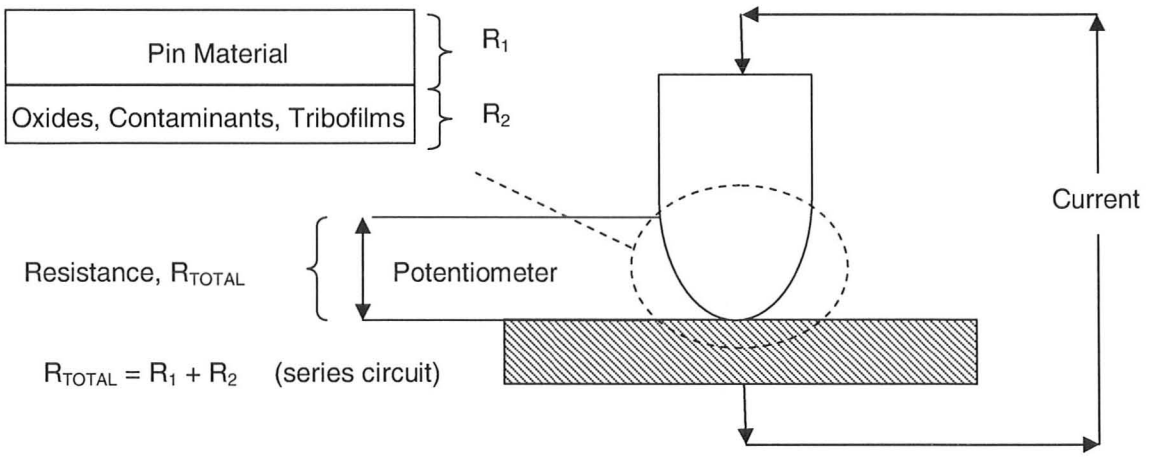

Figure 7.1: Electrical Conductivity Illustration with the Pin and Disk

- Childs has noted that an acoustic emission sensor may be used with a higher signal proportional to more wear (Childs, et al. 2000, 157).
- Godfrey has noted there may be some merit to ultrasonic cleaning. Once a large batch of pins and disks were reground and/or polished they could be ultrasonically cleaned in one batch to remove contaminants.

Chapter 8. Bibliography

American Society for Metals. *Machining - Theory and Practice.* Cleveland, Ohio: American Society for Metals, 1950.

Armarego, E J, and R H Brown. *The Machining of Metals.* Prentice Hall, 1969.

Armarego, E, I S Jawahir, V A Ostafiev, and P K Venuvinod. "Modelling of Machining Operations." *CIRP*, 1996.

Arnell, R D, P B Davies, J Halling, and T L Whomes. *Tribology - Principles and Design Applications.* Macmillan, 1991.

Avient, B W, J Goddard, and H Wilman. "An Experimental Study of Friction and Wear During Abrasion of Metals." *Proceeedings of the Royal Society of London*, 1960: 168.

Bailey, J A. "Friction In Metal Cutting - Mechanical Aspects." *Wear*, 1975: 243-275.

Biksa, A, et al. "Wear Behaviour of Adaptive Nano-Multilayered AlTiN/MexN PVD Coatings During Machining of Aerospace Alloys." *Tribology International*, 2010.

Biwa, Shiro, and Bertil Storakers. "An Analysis of Fully Plastic Brinell Indentation." *Journal of Mechanical Physics of Solids*, 1995.

Blau, Peter J. "Interpretations of the Friction and Wear Break-In Behaviour of Metals in Contact." *Wear*, 1971.

Bonnet, C, F Valiorgue, J Rech, J M Bergheau, P Gilles, and C Claudin. "Development of a Friction Modelling Method in Dry Cutting of AISI 316L Austenitic Stainless Steels." *International Journal of Materials*, 2008.

Boothroyd, Geoffrey. *Fundamentals of Metal Machining and Machine Tools.* Scripta Book Company, 1975.

Bowden, F P, and D Tabor. *The Friction and Lubrication of Solids.* Oxford University Press, 1950.

Brocail, J, M Watremez, and L Dubar. "Identification of a Friction Model for Modelling of Orthogonal Cutting." *International Journal of Machine Tools and Manufacture*, 2010.

Byrne, G, D Dornfeld, and B Denkena. "Advanced Cutting Technology." *CIRP*, 2003.
Callister, William D. *Materials Science and Engineering an Introduction.* John Wiley and Sons, 2003.

Chandrasekaran, H, and D V Kapoor. "Photoelastic Analysis of Tool-Chip Interface Stresses." *Journal of Engineering for Industry*, 1965: 495-502.

Childs, Thomas, Katsuhiro Maekawa, Toshiyuki Obikawa, and Yasuo Yamane. *Metal Machining.* John Wiley & Sons Inc., 2000.

Cristino, V A, P A Rosa, and P A Martins. "On the Utilization of Pin-On-Disc Simulative Tests for the Calibration of Friction in Metal Cutting." *Journal of Engineering Tribology*, 2009.

Curtis, Frank W. *High-Frequency Induction Heating.* McGraw-Hill, 1944.

Dahmus, Jeffrey B, and Timothy G Gutowski. "An Environmental Analysus of Machining." *Proceedings of 2004 ASME International Mechanical Engineering Conference*, 2004.

Davies, M A, T Ueda, R M'Saoubi, B Mullany, and A L Cooke. "On the Measurement of Temperature in Material Removal Processes." *Annals of the CIRP*, 2007.

Dr.G.Fox-Rabinovich, interview by Andrew Biksa. (2010).

Ezugwu, E O. "Key Improvements in the Machining of Difficult-to-Cut Aerospace Alloys." *Ineternational Journal of Machine Tools and Manufacture*, 2005.

Finkin, Eugene F. "Adhesive Wear: A General Review of the State of Experimental Knowledge and Theory." *Materials In Engineering Applications*, 1979.

Fox-Rabinovich, G S, et al. "Multi-Functional Nano-Multilayered AlTiN/Cu PVD Coating For Machining of Inconel 718 Superalloy." *Surface Coatings and Technology*, 2010.

Fox-Rabinovich, G S, K Yamamoto, S C Veldhuis, A I Kovalev, L S Shuster, and L Ning. "Self-Adaptive Wear Behaviour of of Nano-Multilayered TiAlCrN/WN Coatings Under Severe Machining Conditions ." *Surface and Coatings Technology*, 2006.

Fox-Rabinovich, G.S and Totten, G.E. *Self-Organization During Friction.* Taylor and Francis Group, 2007.

Gekonde, Haron O, and S V Subramanian. "Tribology of Tool-Chip Interface and Tool Wear Mechanisms." *Surface and Coatings Technology*, 2002.

Ghosh, Amithabha, and Asok Kumar Mallik. *Manufacturing Science.* Affiliated East-West Press Private Limited, 1985.

Godfrey, Douglas. "Friction Oscillations with a Pin-On-Disc Tribometer." *Tribology International*, 1995.

Grzesik, W. "An Integrated Approach to Evaluating the Tribo-Contact for Coated Cutting Inserts." *Wear*, 2000.

Iawata, Kazuaki, Junshiro Aihara, and Katsuhide Kurasaka. "The Adhesion of Carbide and Carbon Steels At High Pressures and Temperatures." *Wear*, 1971.

Kalpakjian, Serope. *Manufacturing Engineering and Technology.* Addison-Wesley Publishing Company Inc., 1995.

Koshy, Dr. Philip, interview by Andrew Biksa. *Heat in Metal Cutting* (2010).

Koshy, Dr. Philip, interview by Andrew Biksa. *Manufacturing Processes Lecture* (February 2010).

Kuzmin, N N, E A Shuvalova, and O G Checkina. "An Approach To Tribosystem Simulation and Tribotesting." *Tribotest Journal*, 1996.

Lyapin, N.M. Mikhin and K.S. "The Influence of a Perpendicular Load and the Diameter of the Identor on the Tangential Strength of the Adhesive Bond." *Fiziko-Khimicheskaya Mekhanika Materialov* (Plenum Publishing Corporation) 7, no. 1 (September 1969): 36-40.

Mallik, A K, and A Ghosh. *Manufacturing Science.* England: Ellis Horwood Limited, 1986.

Plakhtii, T O. "Forecasting the Technological Performance with Lubricating and Cooling Liquids." *Ukranian Academy of Sciences*, 1990.

Pytel, Andrew, and Jaan Kiusalaas. "Engineering Mechanics: Statics." 346-347. Harper Collins, 1994.

Rabinovich, G S, K Yamamoto, S C Veldhuis, A I Kovalev, and G K Dosbaeva. "Tribological Adaptability of TiAlCrN PVD Coatings Under High Performance Dry Machining Conditions." *Surface Coatings and Technology*, 2005.

Rabinovich, G S, N A Bushe, A I Kovalev, S N Korshunov, L S Shuster, and G K Dosbaeva. "Impact of Ion Modification of HSS Surfaces On The Wear Resistance of Cutting Tools With Surface Engineered Coatings." *Wear*, 2001.

Rabinowicz, Ernest. *Friction and Wear of Materials.* Wiley, 1995.

Rao, S B, V K Kumar, and M C Shaw. "Friction Characteristics of Coated Tungsten Carbide Cutting Tools." *Wear*, 1978.

Rech, J, A Kusiak, and J L Battaglia. "Tribological and Thermal Functions of Cutting Tool Coatings." *Surface and Coatings Technology*, 2004.

Reid, Jean V. "The Twist Compression Test For Evaluating Lubricant/Material Combinations." *Tribology and Lubrication Technology*, 2005.

Rice, Stephen L, and Steven F Wayne. "Specimen Material Reversal In Pin-On-Disc Tribotesting." *Wear*, 1983.

Schey, John. *Tribology in Metalworking.* Waterloo: American Society for Metals, 1983.

Shaw, M C. "The Fundamental Basis of the Hardness Test." In *The Science of Hardness Testing and Its Research Applications*, edited by J H Westbrook and H Conrad, 1-11. American Society for Metals, 1971.

Shaw, Milton C, Ber Abraham, and Pierre A Mamin. "Friction Characteristics of Sliding Surfaces Undergoing Subsurface Plastic Flow." *Journal of Basic Engineering* , 1960.

Shaw, Milton C. *Metal Cutting Principles.* 2nd. New York: Oxford University Press, 2005.

Shirakashi, T, R Komanduri, and M C Shaw. "On Friction and Metal Transfer of Sliding Surfaces Undergoing Subsurface Plastic Deformation." *Wear*, 1978: 197.

Shuster L.S, Korotkov V.A, and Zelin M.G. "Wear Resistance of Die Steel Under Conditions of Hot Sliding Friction." *Material Science and Heat Treatment* (Plenum Publishing Corporation) 31, no. 1-2 (1997): 57-60.

Sreejith, P S, and B K Ngoi. "Dry Machining: Machining of the Future." *Journal of Materials Processing Technology*, 2000.

Stachowiak, G.W, Batchelor, A,W., Stachowiak, G.B. *Experimental Methods in Tribology.* Edited by D Dowson. Vol. Tribology Series 44. Elsevier, 2004.

Steele, Clint. "Use of Log Normal Distribution for the Coefficients of Friction and Wear." *Reliability Engineering and System Safety*, 2008: 1574.

Stephenson, David, A and Agapiou, John, S. *Metal Cutting Theory and Practice.* Marcel Dekker Inc, 1997.

Tabor, D. "The Hardness of Solids." *Review of Physics in Technology*, 1970.

Trent, Edward M. *Industrial Tribology* . Edited by M.H., and Scott, D Jones. Elsevier, 1983.

Trent, Edward M, and Paul K Wright. *Metal Cutting.* 4th. Butterworth-Heinemann, 2000.

Trout, Harry E. "Function and Application of Pyrometers." *Industrial Heating*, 1980.

Weinert, K, I Inasaki, J W Sutherland, and T Wakabayashi. "Dry Machining and Minimum Quantity Lubrication." *CIRP Annals - Manufacturing Technology*, 2004: 511-537.

Zorev, N N. *Metal Cutting Mechanics.* Edited by Milton C Shaw. Oxford - Pergamon Press, 1966.